A Study of Ring Laser Gyroscopes

A THESIS SUBMITTED IN PARTIAL FULFILMENT
OF THE REQUIREMENTS FOR THE DEGREE OF
MASTER OF SCIENCE

by

Nishanthan Rabeendran

2008

Abstract

This thesis presents a study of a 1.6 metre square, helium-neon based ring laser gyroscope (denoted PR-1). This device is mounted on one of the internal walls of a high rise building. After optimisation a cavity Q of 2.9×10^{11} and a sensitivity to rotation of approximately 10^{-3} of the background Earth bias was obtained. A detailed investigation of the single mode operating regime and multi-mode thresholds was undertaken and could be well accounted for with a simple model of the gain curves. A key feature of the operation of PR-1 is persistent longitudinal mode hopping. It is shown that by running the laser at selective high powers, one obtains CW mode locked operation thereby negating the influence of mode hopping and allowing for long time data acquisition. PR-1 was used to demonstrate oscillation of the Rutherford building on its second fundamental mode during an earthquake.

In a separate investigation, a range of supermirrors were studied to determine the optimum configuration in a 4 by 4 metre ring laser. The set with the highest finesse prevailed despite the comparatively low light levels on the photo detectors. The geometric stability of the lasers was not found to be a significant factor.

Contents

List of Figures

List of Tables

Chapter 1

Introduction

1.1 Historical Overview and Summary of the Present Ring Laser Systems

As early as 1925, Michelson, Gale and Pearson demonstrated that it was possible to measure the rotation of the Earth using a Sagnac interferometer. Their device had a rectangular form of dimensions 2000×1100 feet and was made from evacuated sewer pipes near Clearing [37]. This remarkable technological achievement (for the time) yielded a detectable $\frac{1}{4}$ fringe phase difference due to earth rotation thereby demonstrating a measurement of an absolute rotation rate from within a rotating reference frame.

The advent of the laser in 1960 changed the face of interferometry forever. The potential of ring lasers as sensors of inertial rotation (i.e. gyroscopes) was first shown by Macek and Davis as little as 3 years after the laser was first created [34]. Their device operated using a helium-neon gain medium lasing on the 1.153 micron transition. The

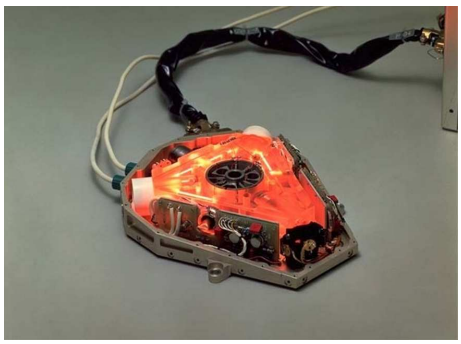

Figure 1.1: Typical He-Ne gyroscope used in inertial navigation systems.

beauty of the active interferometer is that it converts the phase difference measured in a passive device to a more readily measurable frequency difference. Essentially the ring laser cavity supports two independent, oppositely directed traveling waves that can oscillate at different frequencies so as to support coherent amplification. The frequencies of oscillation of the traveling waves are dependent on the rotation of the cavity with respect to inertial space. A measurement of the frequency difference between the two waves gives a direct measurement of the rotation of the laser cavity. Thus, laser gyroscopes measure rotation, with unparalleled precision, readily detecting subtle rotations such as those attributable to seismic events.

Small laser gyros have become widespread in the inertial navigation systems used in aeroplanes, military vehicles and equipment, robotics and even automobiles. However these devices typically have perimeters with an upper limit around 60 cm. In spite of the fact that the original ring gyro [34] of Macek and Davis was 1 metre square, the development of large, active laser interferometers proceeded slowly and much of the genuinely pioneering work was performed as a part of the New Zealand-German-American collaboration [51], based in Christchurch, New Zealand.

The University of Canterbury operates the World's largest ring laser gyroscopes, in a dedicated and unique facility, *the Cashmere Cavern Laboratory* thirty metres under the Port Hills in Christchurch. The laser gyros measure rotation, with extraordinary precision. They easily detect the Earth's rotation as a steady background signal. As stated above we can see disturbances in this steady background due to geophysical events such as earthquakes, and the gravitational influences of the sun and moon, which cause the earth to wobble on its axis. Large gyros have inherent advantages of increased precision and potentially lower quantum noise limits, but their operation on a single cavity mode (essential for gyroscope applications) had initially been thought to be impracticable due to the reduction in free spectral range for the laser cavity as the dimensions increase.

The first ring laser (C-I) built at the University of Canterbury (in collaboration with Prof. Hans Bilger of Oklahoma State University, U.S.) had area of 0.7547 m^2 (Table 1.1). This is shown in figure 1.2. Originally, C-I was housed within the Rutherford building, however this environment was insufficiently mechanically stable since C-I only marginally unlocked on Earth rotation. Nevertheless, this first ring laser was (to the best knowledge of the author) the *first laser gyroscope to unlock on Earth rotation alone* and as such, was an important milestone. Indeed, even C-I was able to determine the Earth rotation with an accuracy of 1 part in 10^{15} of the laser frequency of 474 THz. With the involvement of Prof. Manfred Schneider and Ulrich Schrieber (Technical University

of Munich, Germany) a second ring laser (C-II) was constructed, this time from a solid piece of Zerodur ceramic. Only marginally larger than C-I, the real advances of the C-II construction were the monolithic design (with optically contacted - fixed - supermirrors) and the use of next generation SiO_2-TiO_2 multi-dielectric supermirrors to increase the finesse of the cavity by more than a factor of six. Note that the overall losses in modern supermirrors are significantly less than 10 ppm. C-II was installed in the Cashmere caverns in 1997. Both of these helium-neon based ring lasers were operated on a single longitudinal cavity mode using the method of gain starvation, where the gain is decreased (by lowering the input radio-frequency power) such that only a single cavity mode remains above threshold [51]. In preparation for a proposed German ring laser, the 'Gross-ring', a third ring laser was installed at Canterbury. The G-0 laser is 3.5 metres on a side and vertically mounted [56]. This paved the way for the G-ring which was installed at Wettzell in Bavaria in 2002. The G ring is based on the C-II design in that it is essentially a monolithic ring laser (constructed on top of a large disk of Zerodur). It is a perfectly square ring of perimeter 16 metres housed in a sealed underground laboratory. The G-ring has an unparalleled sensitivity to rotation of better than 1×10^{-8} of the Earth rotation rate Ω_e [44].

More recently, the Canterbury team have embarked upon an ambitious project to build ultra large ring lasers, with geometrical dimensions starting to approach those of the 1925 Michelson interferometer [21, 27]. The first of these devices, UG-1 has dimensions of 21 by 17.5 metres and thereby encloses an area of 367.5 m^2. The second, UG-2, has an optical beam path which encloses an area of 833.7 m^2 - all of the available space of the Cashmere cavern floor. Remarkably, it is possible to get these lasers to run in a single longitudinal cavity mode despite the ever decreasing free spectral range. However the sheer physical dimensions of these lasers give rise to many problems. Both are constructed from stainless steel pipes which connect the four corner boxes containing the supermirrors. Stainless steel has the unfortunate property of out-gassing hydrogen which then contaminates the gain medium over time. Thus, the operational lifetime of a gas fill is around 60 days for UG-2. Further, the 121 metre perimeter of UG-2 means that the intra-cavity beam diameters are significant and sample a comparably large portion of the mirrors which in turn can lead to a propensity for astigmatic and otherwise badly aberrated beams. Additionally, the necessarily heterolithic design (and the fact that the laser is attached to a non-rigid Earth) leads to significant geometric instabilities which in turn, can translate into instabilities in the measurement quantity.

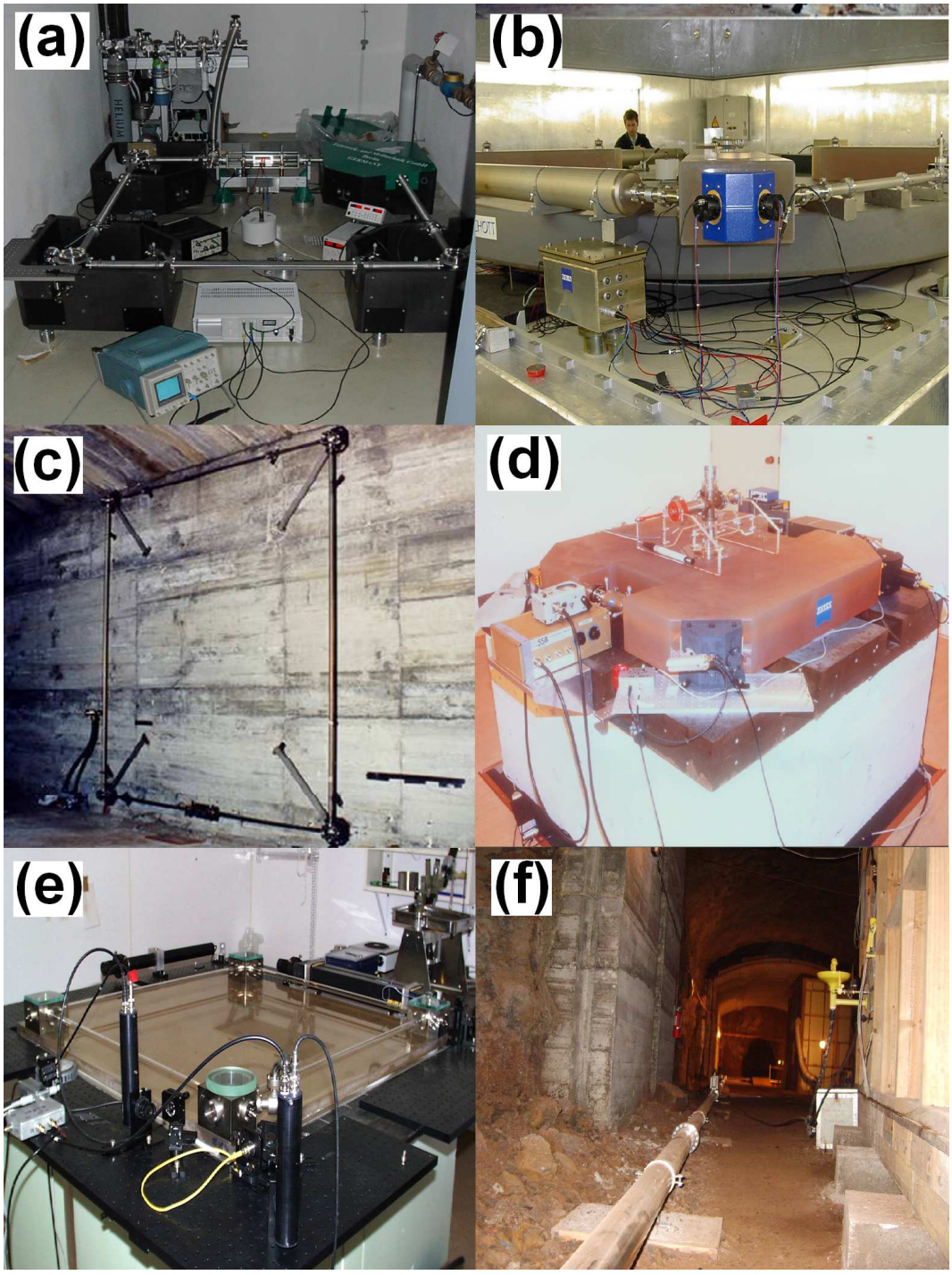

Figure 1.2: The (a) GEOsensor, (b) G-ring, (c) G-0, (d) C-II, (e) C-I and (f) UG-2 ring lasers.

Ring Laser	**Area, m^2**	**Perimeter, m**	f_{Sagnac}**, Hz**	$\Delta\Omega/\Omega_e$
C-II	1	4	79.4	1×10^{-7}
GEOsensor	2.56	6.4	102.6	1×10^{-7}
G	16	16	348.6	1×10^{-8}
UG-1	366.83	76.93	1512.8	3×10^{-8}
UG-2	834.34	121.435	2177.1	5×10^{-8}

Table 1.1: Summary of some physical parameters of the ring lasers

1.2 Motivation and Thesis Outline

The summary above deliberately omits any discussion of the PR-1 laser (Figure 1.2 and Table 1.1) since this forms the basis of much of this thesis. The work presented here has been motivated by several factors. Firstly, a study of the operating characteristics of the PR-1 laser has not been undertaken previously. This is highly relevant since an identical device has been established at the Pinon Flats Seismological Observatory (SCRIPPS Institute of Oceanography) in California in the United States of America. The gyroscope in the US (dubbed the GEOsensor) is designed to monitor coseismic rotations. In fact, ring laser technology is spearheading a very new field of geophysical research, namely that of rotational seismology. Further, we note brief remarks in several articles [19, 20] of a mode locked regime of operation for He-Ne ring lasers and we have attempted to make preliminary observations of that phenomenon here. In a separate (although clearly related) study, we report on the first systematic study of a series of supermirrors in the context of ring laser performance.

Chapter one charts the progress of large ring lasers over the last two decades. Chapter two reviews some relevant concepts in the back ground physics of ring laser gyroscopes. Chapter three consists of characterisation of the PR-1 ring laser. Chapter four explores the mode behavior from the single mode configuration to multimode under different gas pressures and neon isotope ratios. Chapter five reviews the building behaviour measured by PR-1 during normal conditions and during an earthquake. Chapter six looks at the different stability of different supermirror configurations. Chapter 7 summarises the entire thesis.

Chapter 2

Theoretical Considerations

2.1 Sagnac Effect

The Sagnac effect was first observed in 1913 as a moving fringe pattern from an interferometer placed on a turntable [43]. In a ring laser, two beams travel clock wise and counter clockwise direction around the cavity. The beams are reflected along a closed path by the mirrors. The enclosed area by the beam is A. When the inertial frame that the beams are located in rotates with an angular frequency of $\widehat{\Omega}$, the difference in arrival time between the two beams is given by:

$$\delta t = \frac{4\widehat{\Omega}.\widehat{A}}{c^2} \tag{2.1}$$

where c is the speed of light. The relative phase difference caused by the beams due to the rotation is:

$$\delta\phi = \frac{8\pi\widehat{\Omega}.\widehat{A}}{\lambda c} \tag{2.2}$$

where λ is the wavelength of the light. The Sagnac effect can be derived by multiple methods. One of the methods is to use an time of flight proof within the classical (non-relativistic) model [28]. The alternative approach utilises Stokes' theorem [29], which is used here to prove the Sagnac formula:

$$f_{sagnac} = \frac{4\widehat{\Omega}.\widehat{A}}{\lambda P} \tag{2.3}$$

In the ring laser resonator the clockwise and counterclockwise beams have different resonator frequencies. The difference is caused by the time taken to go around the ring, since every resonator point is rotated to a different position, causing a change in path length relative to the inertial frame. Since the ring resonator has specific eigenmodes, it

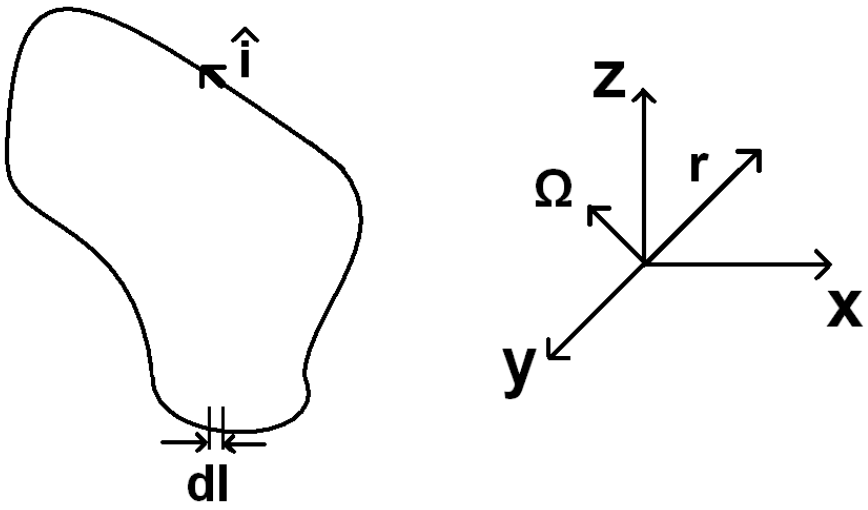

Figure 2.1: Ring laser rotating with angular velocity $\widehat{\Omega}$.

imposes a resonance requirement, that one path around the ring is spanned by an integral number (n) of wavelengths of light:

$$n\lambda = \oint_{ring} \widehat{dl} = P \tag{2.4}$$

where P is the perimeter of the ring.

2.1.1 The Proof of Sagnac Formula Using Stokes's Theorem

The proof applies when a ring laser with angular velocity Ω rotates about an arbitrary axis (fig 2.1). The path integral ΔP is the velocity component along the path multiplied by the time required for light to transverse a path element dl. To obtain ΔP we note that the time taken for the light to travel along the path is dl/c and the velocity component (v_{path}) along the light path of a point in the resonator is:

$$v_{path} = (\widehat{\Omega} \times \widehat{r}).\widehat{i} \tag{2.5}$$

Where

$$\widehat{\Omega} = \Omega_x\widehat{x} + \Omega_y\widehat{y} + \Omega_z\widehat{z} \tag{2.6}$$

$\widehat{x}$, $\widehat{y}$ and $\widehat{z}$ are unit vectors along the x,y,z axis; $\widehat{r}$ is the position vector of a point on the resonator whose coordinates are (x,y,z):

$$\widehat{r} = x\widehat{x} + y\widehat{y} + z\widehat{z} \tag{2.7}$$

and $\widehat{i}$ is a unit vector tangent to the light path at the point x,y,z. Hence:

$$\Delta P = \oint_{ring} [(\widehat{\Omega} \times \widehat{r}).\widehat{i}]\frac{dl}{c} = \frac{1}{c}\oint_{ring} (\widehat{\Omega} \times \widehat{r}).\widehat{dl} \tag{2.8}$$

Where the vector $\widehat{dl} \equiv \widehat{i}\ dl$, now using Stokes theorem:

$$\oint_{ring} (\widehat{\Omega} \times \widehat{r}).dl = \int\int_{\frac{ring}{area}} [\nabla \times (\widehat{\Omega} \times \widehat{r})].dA \tag{2.9}$$

Thus

$$\triangle P = \frac{1}{c}\int\int_{\frac{ring}{area}} [\triangle \times (\widehat{\Omega} \times \widehat{r})].dA \tag{2.10}$$

Using identity on the equation above;

$$\nabla \times (\widehat{\Omega} \times \widehat{r}) = \widehat{\Omega}(\nabla.\widehat{r}) - \widehat{r}(\nabla.\widehat{\Omega}) + (\widehat{r}.\nabla)\widehat{\Omega} - (\widehat{\Omega}.\nabla)\widehat{r} \tag{2.11}$$

The equation above simplifies when Ω=const. This leads to $\nabla.\Omega = 0$ and equation below.

$$(\widehat{r}.\nabla)\widehat{\Omega} = (x\widehat{x} + y\widehat{y} + z\widehat{z}).(\widehat{x}\frac{\partial}{\partial x} + \widehat{y}\frac{\partial}{\partial y} + \widehat{z}\frac{\partial}{\partial z})\widehat{\Omega} = 0 \tag{2.12}$$

Also,

$$\nabla.\widehat{r} = (\widehat{x}\frac{\partial}{\partial x} + \widehat{y}\frac{\partial}{\partial y} + \widehat{z}\frac{\partial}{\partial z}).(x\widehat{x} + y\widehat{y} + z\widehat{z}) = 3 \tag{2.13}$$

and

$$\begin{aligned}
(\widehat{\Omega}.\nabla)\widehat{r} &= \widehat{\Omega}.(\widehat{x}\frac{\partial}{\partial x} + \widehat{y}\frac{\partial}{\partial y} + \widehat{z}\frac{\partial}{\partial z}).(x\widehat{x} + y\widehat{y} + z\widehat{z}) && (2.14)\\
&= (\Omega_x\frac{\partial}{\partial x} + \Omega_y\frac{\partial}{\partial y} + \Omega_z\frac{\partial}{\partial z}).(x\widehat{x} + y\widehat{y} + z\widehat{z}) && (2.15)\\
&= \Omega_x\widehat{x} + \Omega_y\widehat{y} + \Omega_z\widehat{z} && (2.16)\\
&= \widehat{\Omega} && (2.17)
\end{aligned}$$

Combining equation 2.10-2.14

$$\nabla \times (\widehat{\Omega} \times \widehat{r}) = 3\widehat{\Omega} - \widehat{\Omega} = 2\widehat{\Omega} \tag{2.18}$$

Combining equation 2.18 with 2.11 we get, for constant $\widehat{\Omega}$

$$\triangle P = \frac{1}{c}\int\int_{\frac{ring}{area}} 2\widehat{\Omega}.d\widehat{A} = \frac{2}{c}\widehat{\Omega}.\widehat{A} \tag{2.19}$$

Using the resonant frequency shift caused by the path length change $\triangle v/v = \Delta P/P$ and the equation above:

$$\frac{\triangle v}{v} = \frac{\Delta P}{P} = \frac{2\widehat{\Omega}.\widehat{A}}{cP} \tag{2.20}$$

Finally using the beat frequency (f_{beat}) between the two resonators,

$$f_{beat} = 2\Delta v = \frac{4\widehat{\Omega}.\widehat{A}}{\lambda P} \tag{2.21}$$

2.2 The Gain Medium

The light wave is amplified by simultaneous emission as it passes through the gain medium. The amplification depends on the population inversion, shape of the gain curve, frequency of the transition and radiative life time. In He-Ne lasers the population inversion occurs between 5s and 3p states in neon. The neon 5s state is pumped by collision with 2^1S helium atom. While the radio frequency is used to excite the ground state helium atom to 2^1S state. The fractional gain in single pass of the gain medium produced by this process influence the shape of the gain curve. The shape of the gain curve itself is determined by a combination of homogenous and inhomogeneous broadening.

2.2.1 Homogenous Broadening

Homogenous broadening influences all atomic dipoles uniformly. There are two main types of homogenous broadening: lifetime and collision broadening.

Lifetime broadening occurs because of spontaneous emission of the lasing energy level. The Heisenberg uncertainty principle gives a minimum uncertainty in the energy of the transition. For the neon transition (5s to 3p) at 632.8 nm the decay time is about 55 ns for the upper level and about 7-10 ns for the lower level [24]. Natural broadening leads to a Lorenzian distribution.

The full width half maximum of the Lorentzian line γ is given by the equation below:

$$\gamma = \frac{1}{2\pi\tau_{upper}} + \frac{1}{2\pi\tau_{lower}} \tag{2.22}$$

where τ is the spontaneous decay rate of the energy level. For the transition mentioned above, this gives the value of 18 MHz.

Another type of broadening mechanism is collision broadening. Collision broadening is due to collisions between atoms, ions, free electrons and the walls of the gain tube. The atoms, ions, and free electrons move randomly due to thermal and Brownian motions. When a collision occurs it causes a disturbance in the phase of the electric field of the species undergoing the collision. Generally collisions between the emitting species and the gain tube is not important at optical frequencies [46]. Homogenous broadening increases linearly with total pressure of He and Ne [46]. For a He-Ne mixture, the broadening is roughly 77 MHz/torr [46].

2.2.2 Inhomogeneous Broadening

This is the most important broadening mechanism for gas lasers. This occurs because of atoms having different resonance frequencies which are randomly distributed from a central frequency.

Doppler broadening is the dominant process in broadening for He-Ne lasers. It is caused by Doppler shifts of the individual atoms due to thermal motion. The Doppler broadening width $\triangle\nu$ is given by

$$\triangle\nu = 2\nu_o\Big(\frac{2k_BTln(2)}{Mc^2}\Big)^{1/2} \tag{2.23}$$

where ν_o is the lasing frequency of 4.74×10^{14} Hz, k_B is Boltzmann's constant, T it is temperature, and M is the mass of Ne. This gives a value of 1.5 GHz which agrees with the quoted value of 1.5 GHz [56].

2.2.3 Gaussian Lineshape Function

Figure 2.2 shows the general gain curve comprised of homogenously broadened spectral packets (group of atoms which respond as one). The convolution of the packets gives the final Gaussian curve. When the difference in frequency between the spectral packets $(\nu_1 - \nu_2)$ is large compared to the homogenous width of the packets $\Delta\nu_1$ the Doppler broadening is large. When the width of the spectral packet is wide compared to linewidth of the Gaussian curve $(\Delta\nu_o)$, Doppler broadening is small or nonexistent. The width of the spectral packet depends on collision broadening and lifetime broadening, since lifetime broadening is essentially constant and small in magnitude compared to collision broadening. Only the collision broadening process is taken into account in the following discussion. Collision broadening increases with pressure due to the fact that the number of species available for collision increases, assuming the volume in kept the same, which is true for all the experiments done with PR-1. Doppler broadening depends on the temperature and mass of the species involved, in our case Ne (equation 2.23).

2.2.4 Saturation of the Gain Medium

In the previous section we have considered the effect of homogenous and inhomogeneous broadening of the laser gain medium without the complication of saturation effects. In this section the hole burning effect is introduced as it is the main mechanism to influence

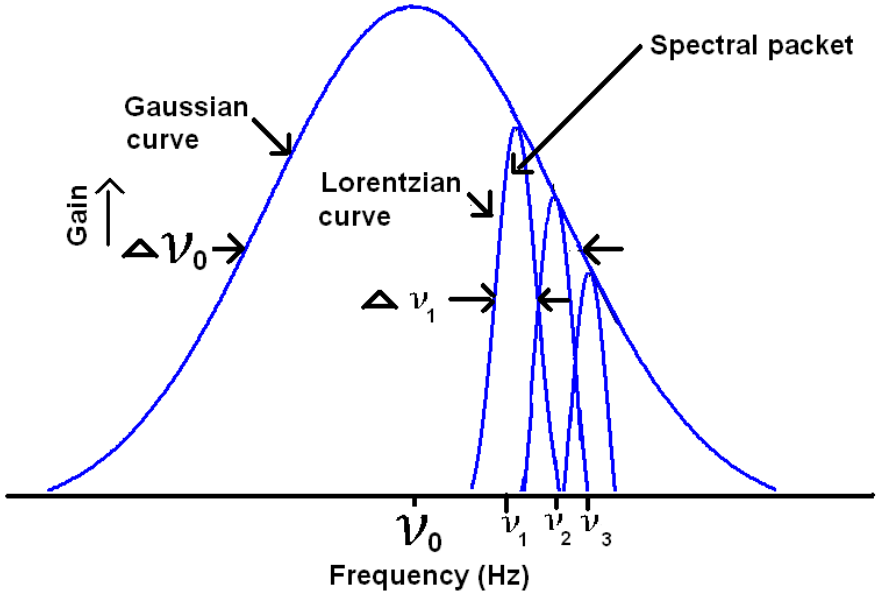

Figure 2.2: Generalised Gaussian profile, showing a homogenously broadened spectral packet under the Gaussian gain curve.

the gain curve in a He-Ne plasma. This effect is introduced here since it affects the shape of the gain curve and consequently it changes the gain available for the cavity modes.

When an external signal is applied to the gain medium (such as the circulating intra-cavity beam) it causes the population inversion in the lasing transition to decrease. As the intensity of the signal increases the inversion tends towards zero. The response of the gain curve to the applied intensity varies depending on the type of broadening [50]. In homogenous broadening when the signal is applied the whole curve responds as one (fig 2.3).

Since the Gaussian lineshape profile is a convolution of many homogenously broadened spectral packets (fig 2.2), a hole is burned that depends on the location in the gain curve and affects only the spectral packet(s) near the signal (fig 2.4). As implied in fig 2.2, the inhomogeneous broadening is much larger than the homogeneous, and therefore dominates the overall broadening.

2.3 Noise Processes in the Ring Laser

The ring laser detection and data acquisition system is composed of a beam combining system (which yields an oscillating signal) and a counter. The oscillating signal is the

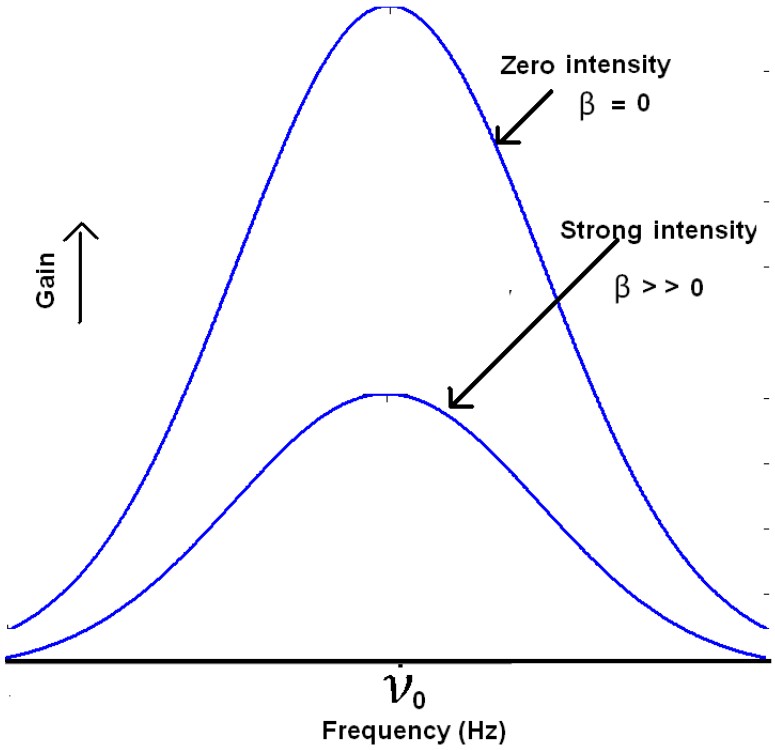

Figure 2.3: Homogeneously broadened Lorenzian line, saturated by strong intensity.

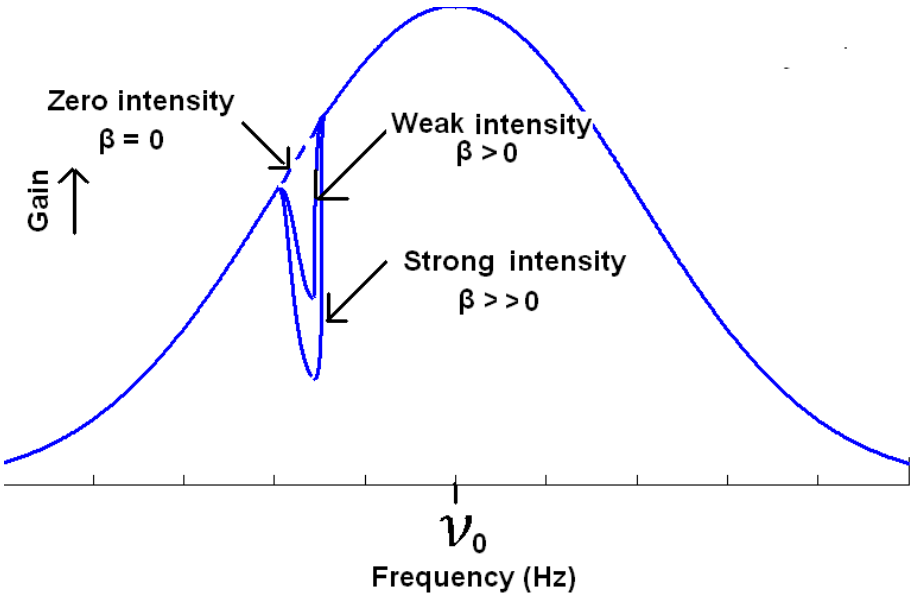

Figure 2.4: Inhomogeneously broadened Gaussian line, saturated by weak and strong intensity.

beat frequency between two slightly different optical frequencies.

A function generator (Stanford DS335) is used to count the cycles of the beat signal. In ultra sensitive rings a GPS clock is used to increase the stability of the counter, however, there are inherent instabilities. The measurement noise associated with detectors such as photodiodes, photomultipliers and electronic circuits also contributes to the process. The frequency is determined by phase comparison against a very stable function generator. The signal from ring lasers can be defined mathematically as:

$$v(t) = (V_0 + \varepsilon(t))sin[2\pi\nu_0 t + \varphi(t)] \tag{2.24}$$

where V_0 is the nominal peak voltage, ε(t) is the deviation of amplitude due to noise, ν_0 the theoretical Sagnac frequency and $\varphi(t)$ is the deviation of the phase.

If the angular velocity of the ring is constant (and in the absence of mode competition and frequency pulling or lock in) then $\varepsilon(t)$ and $\varphi(t)$ will be zero all of the time. In a working gyroscope this is unattainable for several reasons; random and systematic variation of the beat frequency; environmental perturbations such as changes in temperature, humidity, shock, vibration and pressure [8].

2.3.1 Allan Variance

Allan variance provides a quantitative way to measure the stability of the laser over time. The data from the ring laser is collected in the measurement time interval τ. The standard deviation is not used since it is a function of the number of the points in the data. It is also affected by the dead time and the bandwidth of the measurement system [26]. Allan variance σ_A is defined as [7]

$$\sigma_A^2 = \frac{1}{2(n-1)} \sum_{p=1}^{n-1} (\nu_{p+1} - \nu_p)^2 \tag{2.25}$$

where $\Delta\nu = \nu_{p+1} - \nu_p$ is change in frequency, and n is number of measurements. Phase tracking software is used to measure the phase difference between the generated sine wave (using a Stanford DS335) and the Sagnac waveform. The phase difference was used to calculate the change in frequency $\Delta\nu$ then needed to calculate Allan variance. The formulae used to calculate the change in frequency ($\Delta\nu$)is:

$$\Delta\nu = \frac{\phi(t+2\tau) - 2\phi(t+\tau) + \phi(t)}{\tau} \tag{2.26}$$

where $\phi(t)$ is the phase, τ is the measurement time [54]. The change in frequency ($\Delta\nu$) is inserted into equation 2.25 to calculate the Allan variance.

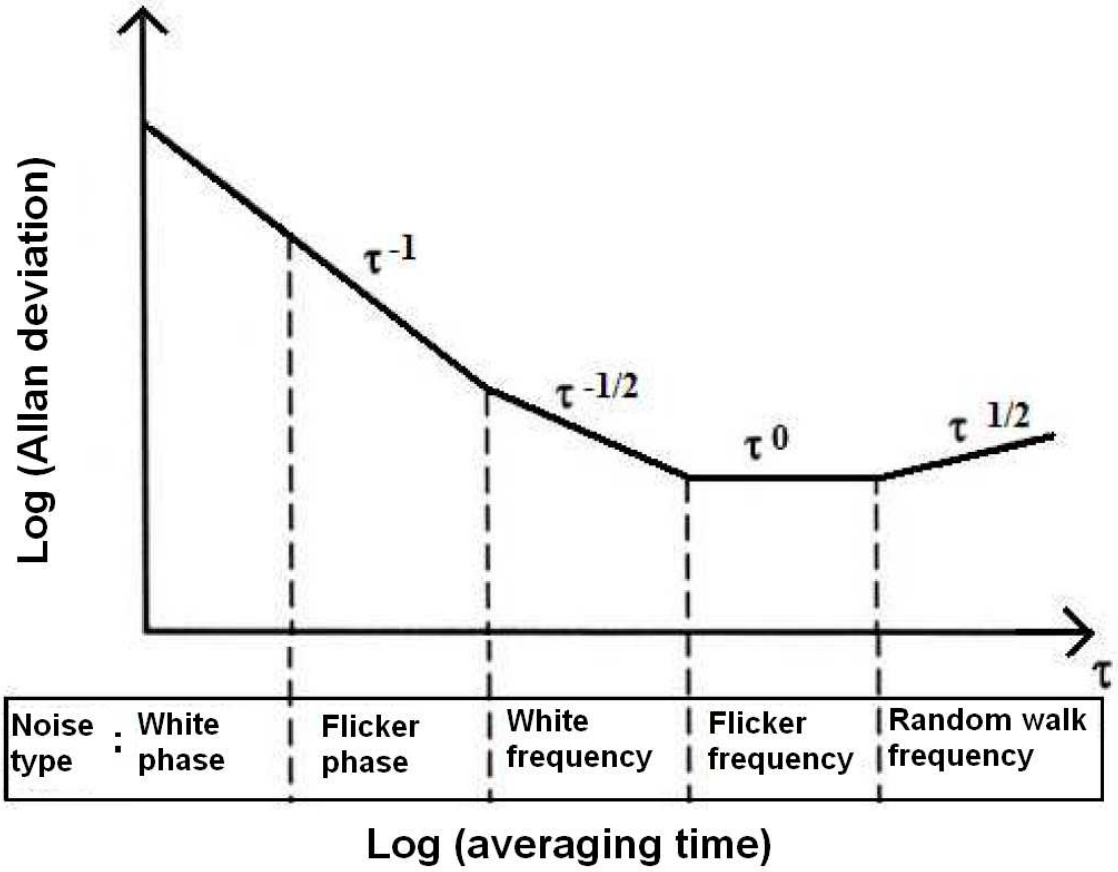

Figure 2.5: The different noise types give rise to integer or half-integer power laws for the Allan deviation as indicated.

Noise type	**Power of f**
1.Random walk FM	$\alpha = -2$
2.Flicker FM	$\alpha = -1$
3.White FM	$\alpha = 0$
4.Flicker PM	$\alpha = 1$
5.White PM	$\alpha = 2$

Table 2.1: The power of Fourier frequency (α) corresponding to various noise

2.3.2 Power Spectral Density

The random deviation of the frequency can be characterised by a power law spectrum [9]:

$$S_y(f) = h_\alpha f^\alpha \tag{2.27}$$

where S_y is the spectral density of the fractional frequency fluctuation, y is the normalised Fourier frequency deviation, f is the Fourier frequency, h_α is the intensity of the noise and α is constant over the range of f. There are five main powers of α corresponding to various noises in the oscillator (table 2.1):

The relationship between power law spectra and Allan variance is shown by Culter[17] to be:

$$\sigma^2(\tau) = 2\int_0^\infty df S_y \frac{sin^4(\pi f\tau)}{(\pi f\tau)^2} \tag{2.28}$$

This can be generalised to give an approximate relationship between τ and the Allan variance; $\sigma^2(\tau) \sim \tau^\mu$, where μ is constant and it is related to α; $\mu = -\alpha - 1$ when $-3 < \alpha \leq 1$ and $\mu = -2$ when $\alpha \geq 1$. Figure 2.5 summarises various powers of τ and how they correspond to different noises.

2.4 Sideband Analysis

Sidebands appear on the fast Fourier spectrum when the Sagnac frequency is modulated by some perturbation. The side band can be created due to a variation of tilt or a rotation induced by the perturbation e.g. a seismic event. By looking at the carrier frequency it

is possible, with the reasoning that follows, to obtain absolute rotation rate and the magnitude of the rotation, even when the modulation is caused by tilt. In this thesis we deal with tilt caused by building oscillation during an earthquake.

The following side band analysis was first performed by Stedman [52] (later modified by McLeod [36]).

In the ring laser there are two clockwise and counter clockwise beams with rapidly oscillating complex field ($\tilde{E}_{\pm}$). The convention used throughout the chapter is positive for clockwise beam and negative for counter clockwise beam.

$$\tilde{E}_{\pm} = E_{\pm} e^{i\phi_{\pm}} \tag{2.29}$$

The phase of the field is defined as:

$$\phi_{\pm} = \omega_{\pm}(t - \frac{z_{\pm}}{c}) \tag{2.30}$$

where $z_{\pm}$ are the optical path lengths from an arbitrary origin and $\omega_{\pm}$ are the frequency of the cavity modes. The analysis only applies for single longitudinal mode operation.

$$f = \frac{\omega_{+} - \omega_{-}}{2\pi} \tag{2.31}$$

The phasors $\tilde{E}_{\pm}$ change with time due to several reasons [53]. The first is the time dependence present in equation 2.30, in the form of $\omega_{\pm}t$. Differentiating this equation 2.29 with respect to time gives:

$$\frac{d\tilde{E}_{\pm}}{dt} = i\omega_{\pm}\tilde{E}_{\pm} \tag{2.32}$$

The second time dependence is caused by laser pumping (a), saturation (β) and cross saturation (ξ), which provides a scaling factor for $\tilde{E}_{\pm}$:

$$\frac{d\tilde{E}_{\pm}}{dt} = (\pi a - \beta\tilde{E}_{\pm}^2 - \xi\tilde{E}_{\mp}^2)\tilde{E}_{\pm} \tag{2.33}$$

The final time dependence is caused by backscatter. For argument say at point A the backscatter contributes a time dependent phasor. The backscatter can be caused by various imperfections on the supermirrors and at the edges of the gain tube. The imperfections are labeled n, and have different optical path lengths ($z_{n\pm}$) from A. A different optical path length from A to the imperfection causes a phase of shift of $e^{-i\omega_{\pm}z_{n\pm}/c}$ on $\tilde{E}_{\pm}$. The scattered wave from the imperfection will have a different phase and amplitude by a complex back scatter factor $\tilde{A}_{\pm}$. This gives the resultant phasor as:

$$\tilde{A}_{\pm}\tilde{E}_{\pm}e^{i\omega_{\pm}t - i\omega_{\pm}z_{n\pm}}/c \tag{2.34}$$

When the wave propagates back to A it adds another phase factor $e^{i\omega_{n\mp}}$. The total phase shift at A is $e^{-i\omega_{\pm}}(z_{n_{\pm}} - z_{n_{\mp}} + P_{\mp})/c$. To approximate nonreciprocities, $\omega_{\pm}$ and $P_{\pm}$ it is replaced with an average value in ω and P. This means that in the phase calculation it is possible to take $z_{n+} \simeq P - z_{n-} \equiv z_n$ and use $\omega P{=}2\pi cN$ to show that the distance-dependent phase doubles in the journey back to A. The effect of the backscatter at point A per unit of time is:

$$R_{\mp} = \sum_n \tilde{A}_{\mp} e^{2i\omega z_n/c} \tag{2.35}$$

The equation above shows the phase changes due to propagation distance is the same for R_+ and R_- and the difference is only caused by $\tilde{A}_{n\pm}$. The amplitude and the phase of equation 2.35 is defined by $R_{\mp} = r_{\mp}e^{i\epsilon_{\mp}}$. Hence the backscatter contribution to the time dependent phasor is :

$$\frac{d\tilde{E}_{\pm}}{dt} = r_{\mp}\tilde{E}_{\mp}e^{i\epsilon_{\mp}} \tag{2.36}$$

Combining the contribution from equations 2.32,2.33 and 2.36.

$$\frac{d\tilde{E}_{\pm}}{dt} = (i\omega_{\pm} + \pi a - \beta\tilde{E}_{\pm}^2 - \xi\tilde{E}_{\mp}^2)\tilde{E}_{\pm} + r_{\mp}\tilde{E}_{\mp}e^{i\epsilon_{\mp}} \tag{2.37}$$

separating the imaginary and complex components of the equations we get;

Real part:

$$\frac{1}{\tilde{E}_{\pm}}\frac{d\tilde{E}_{\mp}}{dt} = (\pi a - \beta\tilde{E}_{\pm}^2 - \xi\tilde{E}_{\mp}^2) + \rho_{\mp}cos(\psi \mp \zeta) \tag{2.38}$$

Imaginary part:

$$\frac{d\phi_{\pm}}{dt} = \omega_{\pm} \mp \rho_{\mp}\sin(\psi \mp \zeta) \tag{2.39}$$

where the beam amplitude backscatter scale factor, $\rho_{\pm}$:

$$\rho_{\pm} = r_{\pm}\frac{E_{\pm}}{E_{\mp}} \tag{2.40}$$

relative beam phase, ψ:

$$\psi = \phi_+ - \phi_- + \frac{\epsilon_+ - \epsilon_-}{2} \tag{2.41}$$

net backscatter phase, ζ:

$$\zeta = \frac{\epsilon_+ + \epsilon_-}{2} \tag{2.42}$$

The relative beam phase ψ, from which the detected signal is obtained, varies in time as:

$$\frac{d\psi}{dt} = 2\pi f - \rho_-\sin(\psi - \zeta) - \rho_+\sin(\psi + \zeta) \tag{2.43}$$

If the backscatter from each beam is equal $\rho_+ = \rho_- = \rho$, we obtained the Adler equation:

$$\frac{1}{2\pi}\frac{d\psi}{dt} = f - l\sin(\psi) \tag{2.44}$$

where $l = \frac{\rho}{\pi} cos(\zeta)$. Suppose a modulation is applied on the Sagnac frequency (e.g. modulation caused by building vibration and earthquakes)

$$f = f_e - S f_m \sin 2\pi f_m t \tag{2.45}$$

where f_e is the Sagnac frequency due to Earths rotation, f_m the frequency of the modulation applied on the Sagnac frequency and S is the amplitude (in radians) of the phase excursion caused by the frequency modulation. Integrating equation 2.45 with respect to time to give phase modulation:

$$\psi_f(t) = 2\pi f_e t + S \cos 2\pi f_m t \tag{2.46}$$

With this phase modulation the detected signal can be written as:

$$V(t)_{FM} = Re(V_e e^{i\psi_f}) = Re(V_e e^{i2\pi f_e t + S\cos 2\pi f_m t}) \tag{2.47}$$

This equation can be expanded as:

$$V(t)_{FM} = Re(V_e e^{i2\pi f_e t}(J_0(S) + s\sum_{n=1}^{\infty} i^n J_n(S)\cos(2\pi f_e t))) \tag{2.48}$$

This shows that an infinite number of sidebands will form on both sides of the Sagnac 'centre' frequency (f_e) separated by the modulation frequency (f_m). The power of the sidebands is governed by the Bessel function $J_n(S)$.

$$J_n(S) = (\frac{S}{2})^n \sum_{m=0}^{\infty} (-1)^m \frac{(\frac{S}{2})^{2m}}{m(m+n)} \tag{2.49}$$

If $S<<1$, the lower sidebands are N decibels below the carrier, where

$$\begin{aligned} N &= 20\log(\frac{J_o(S)}{J_1(S)}) && (2.50)\\ &\approx 20\log(\frac{2}{S}(1 - \frac{1}{8}S^2)) && (2.51)\\ &\approx 6 - 20\log S && (2.52) \end{aligned}$$

Therefore, the sidebands which are 20n below the carrier gives the modulation index of:

$$S \approx 2 \times 10^{-n} \tag{2.53}$$

If the peak frequency deviated from f_e by Δf, then:

$$S = \frac{\Delta f}{f_m} \tag{2.54}$$

This leads to a change in frequency of:

$$\Delta f \approx 2 \times 10^{-n} f_m \tag{2.55}$$

If the modulation is caused by rotation, the absolute angular rotation is given by:

$$\theta = \frac{S\lambda}{2P} \tag{2.56}$$

where θ is the angular amplitude, S the modulation index, λ is the wavelength of the laser and P is the perimeter of the ring laser.

Chapter 3

Preliminary Characterisation of the PR-1 Ring Laser

PR-1 is a 1.6 metre square, ring laser gyroscope employing the helium-neon gain medium as with the other lasers operated by the Canterbury ring laser research group. This laser is currently mounted vertically on the seventh floor of a high rise building (the Rutherford building on the central campus of the University of Canterbury). This laser is one of two identical devices: one located at the Piñon flat seismological observatory in California and denoted the GEOsensor; one at Canterbury. The primary goal of the GEOsensor is to measure seismically induced rotation [44]. Because the GEOsensor is an observatory based instrument, its performance has not been characterised over a significant parameter range e.g. at different gas pressures. PR-1 can serve that purpose. In addition, PR-1 is ideally positioned to be used as a monitor of building dynamics under the influence of external perturbations. This chapter describes the preliminary operation and optimisation of the PR-1 ring laser.

3.1 Preliminary Details

The PR-1 ring laser was constructed during August and September 2003 and the first lasing was achieved shortly thereafter. Due to various unforeseen problems, the project stagnated. Here we describe the initial attempts to resurrect it.

3.1.1 PR-1 Equipment Setup

The PR-1 ring laser is mounted vertically on a structural wall of the Rutherford building (fig 3.1 and 3.2). Each of the corner boxes are held in place by three 15 mm steel bolts

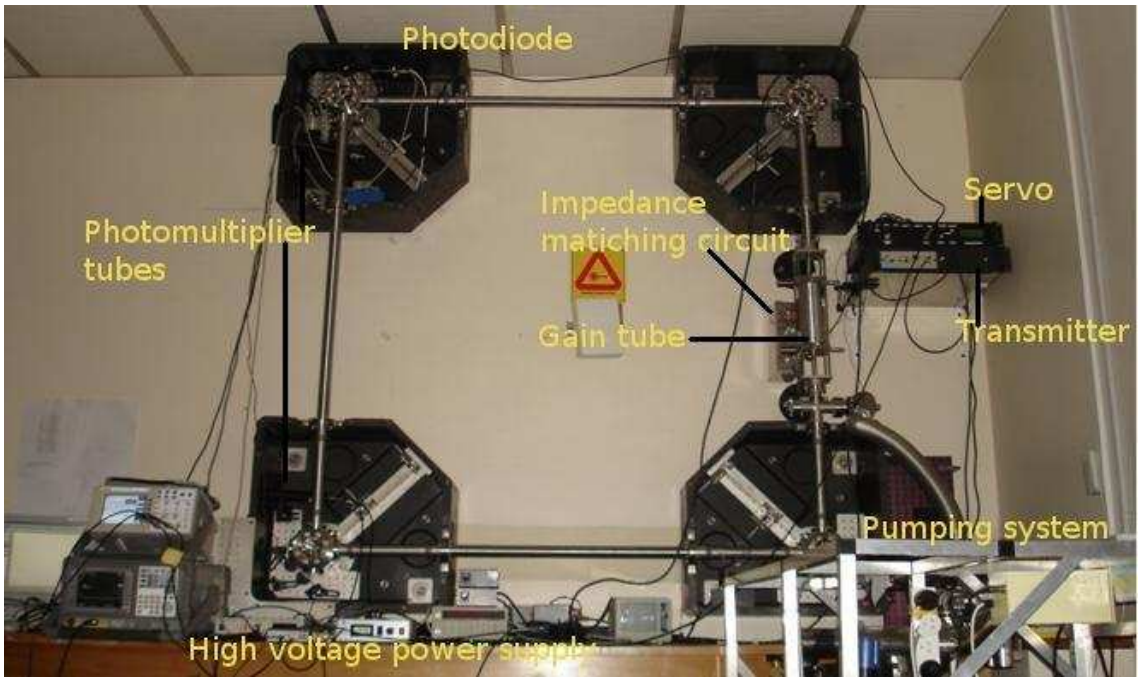

Figure 3.1: The PR-1 ring laser.

which are imbedded 150 mm into the concrete wall. The corner boxes are connected together by a 1.6 m stainless steel arm. All of the stainless steel segments are connected together with copper washers so they can withstand the high vacuum produced by the turbo pump (see chapter 4 for details). The arm on the left of PR-1 contains the 4 mm diameter gain tube. The gain tube is made from fused silica, which is transparent to RF frequency, has a low outgassing rate and is able to withstand the temperatures required to create the He-Ne plasma [55].

Helium-Neon gas is used as a gain medium, and it is pumped by an 80 MHz radio frequency transmitter. The electrodes at the edge of the plasma tube are earthed; and an oscillating longitudinal electric field develops between the middle electrode and the outside ones. The electrons are forced by the electric field to oscillate between the electrodes, which behave in a similar fashion to a capacitor ring.

The laser beam is maintained at a constant output power by the servo system. The servo system compares the laser set voltage with a laser voltage from the photodiode and adjusts the RF supply until the laser voltage matches the set voltage [36]. The output impedance of the RF supply is 50 ohms which is different from that of the plasma, so an impedance matching unit is needed to maximise the energy transfer between the plasma and the RF supply. The impedance of the plasma is a function of density, distribution of the plasma itself and a function of absorbed power [23, 24]. The photodiodes are housed

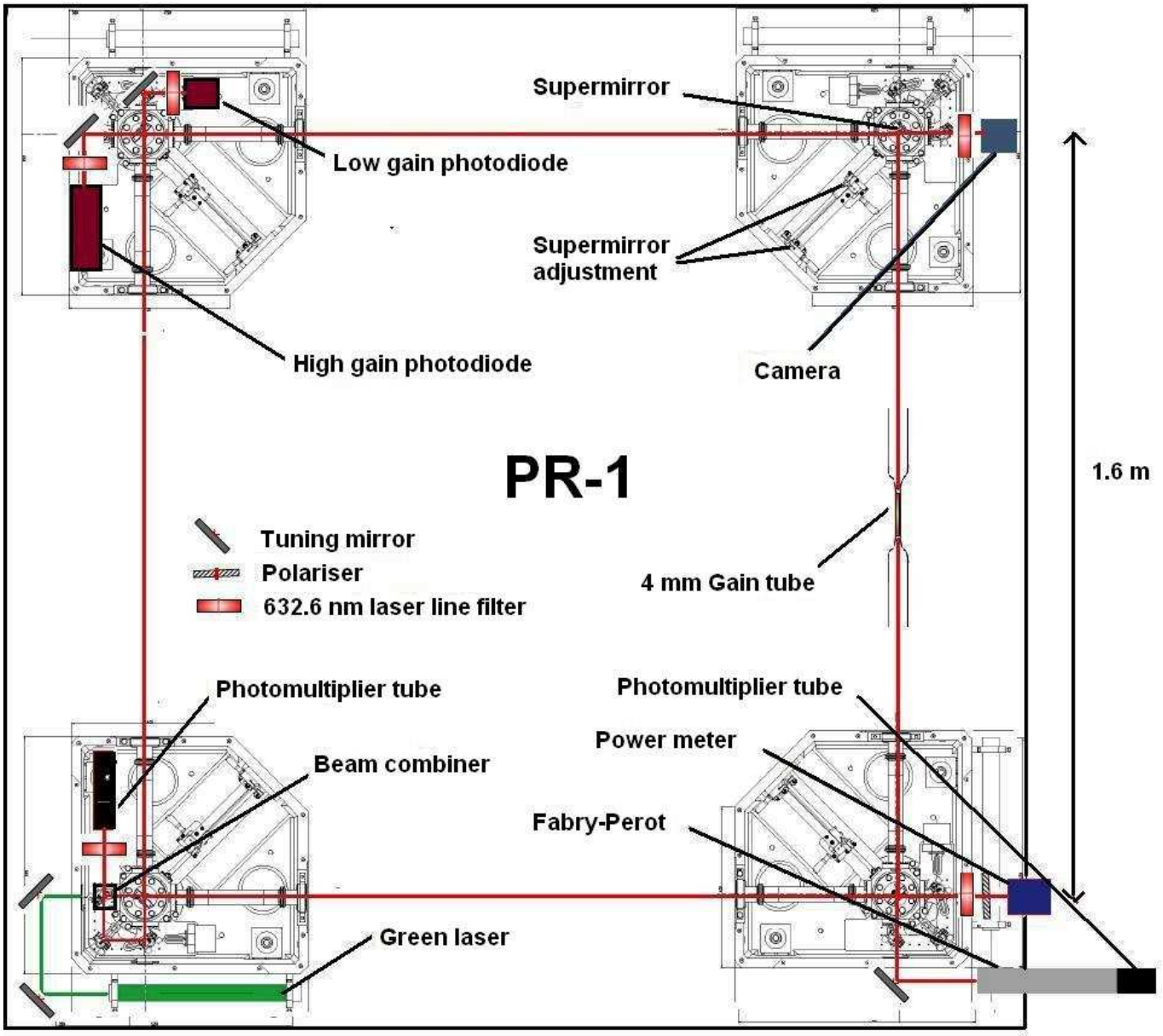

Figure 3.2: Schematic of PR-1.

at the top right hand side of the corner box and have plasma filters attached to them to prevent plasma light affecting the measurement. The high gain photodiode is 1.3 times more sensitive than low gain one. The two different gain photodiodes are needed due to the wide range of power needed for the experiments described in this thesis. The clockwise and counter clockwise laser beams supported by the gain-medium are transmitted through the supermirror in the bottom left corner box. A cube beam splitter is used to combine both beams producing a moving fringe pattern, which is measured using a Hamamatsu R3896 photomultiplier tube (PMT). The PMT has a quantum efficiency of 14 % at the lasing wavelength of 632.8 nm [1]. The PMT is powered by a high voltage supply. The PMT is a current source, so the signal must be converted to a voltage output by a transimpedance amplifier prior to data acquisition. The corner box on the bottom right contains a Fabry-Perot spectrum analyser used to study the cavity mode structure. It is also used to collect the transmitted beam though the Fabry-Perot. A green He-Ne laser is used as an alignment beam for the ring cavity. The top right hand side corner box contains a camera which initially was put in place to measure the transverse mode patterns. The beams captured were distorted as it traveled though the supermirror and the glass window in the corner box (fig 3.3) making transverse mode analysis difficult.

3.1.2 Alignment of the Detection System

The output power of all of our ring lasers is in the nanowatt range due to the supermirrors used in the cavity construction. This makes the beam difficult to see with the naked eye, therefore the alignment was carried out in darkness. The clockwise and counterclockwise beams from the laser were passed through the beamsplitter and reflected using a tuning mirror to the furthermost distance possible within the current laboratory setup. White paper was placed close to the beamsplitter and a turning mirror on the counterclockwise beam was adjusted until both beams were combined. The paper was then moved away from the laser until two separate spots could be seen (fig 3.4), and then the beamsplitter was adjusted. This process was repeated until the beams were parallel and spatially overlapped.

Figure 3.5 shows a representative time series of the Sagnac frequency output from PR-1 after optical alignment. Very large spikes (off the scale on figure 3.5) are observed when the laser is operating in *split mode* - the clockwise and counterclockwise beams running on different longitudinal modes. *Mode hops* - when both beams jump simultaneously to higher or lower longitudinal mode indexes, are also visible.

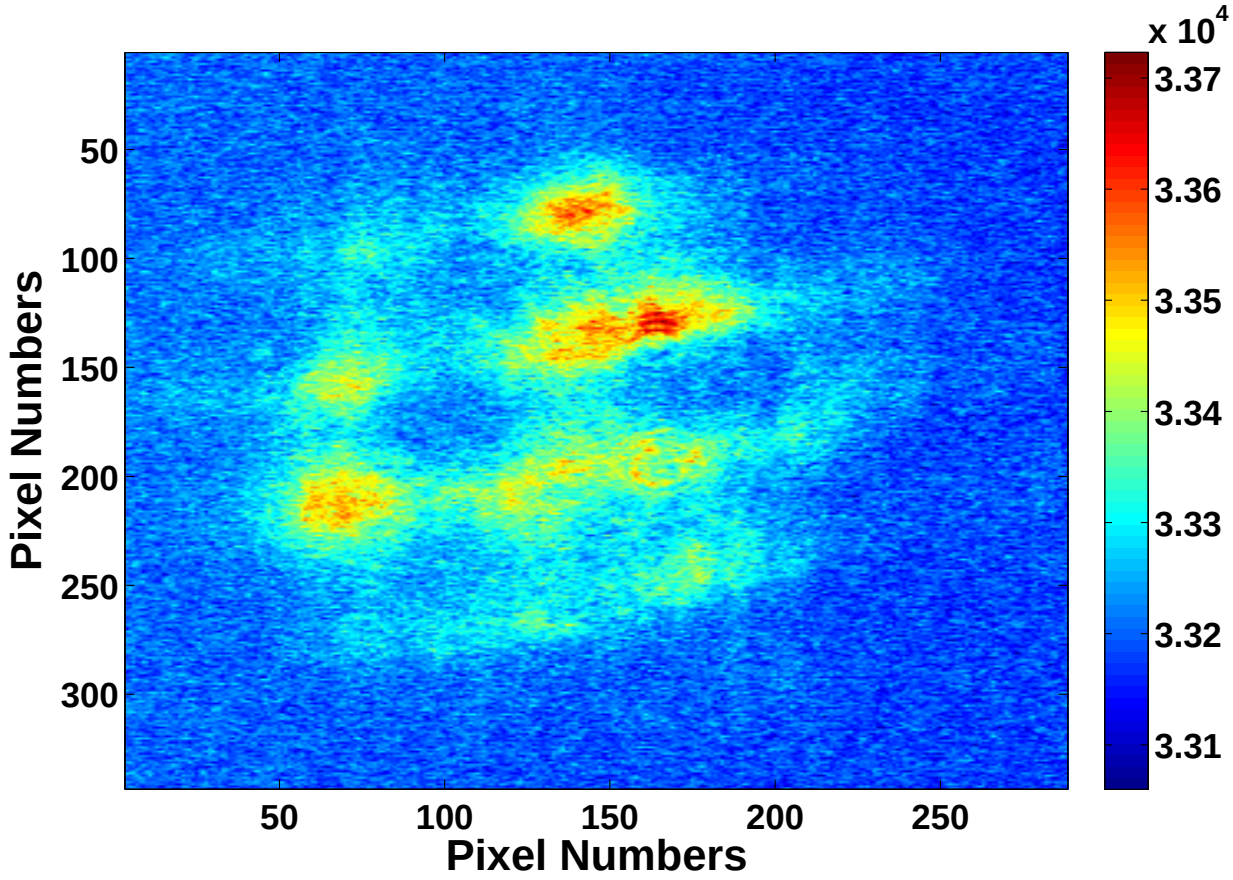

Figure 3.3: The false colour contour plot of the PR-1 laser beam through the supermirror. The arbitrary intensity scale of the beam is displayed on the right. Interference in the window and distortion through the supermirror yields the observed pattern.

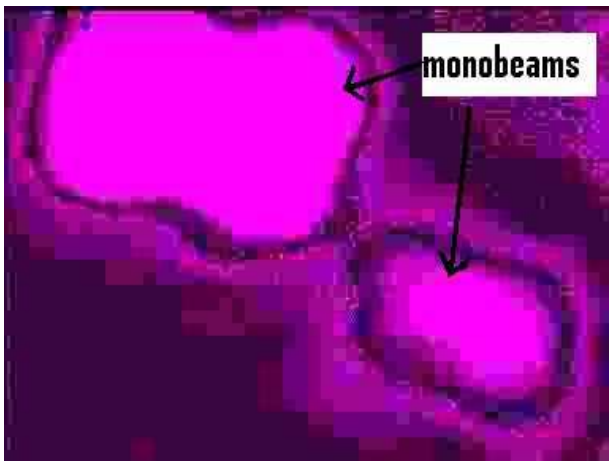

Figure 3.4: The counter propagating laser beams as seen in the alignment process. Notice the higher order mode structure that is visible at the edges of the beams.

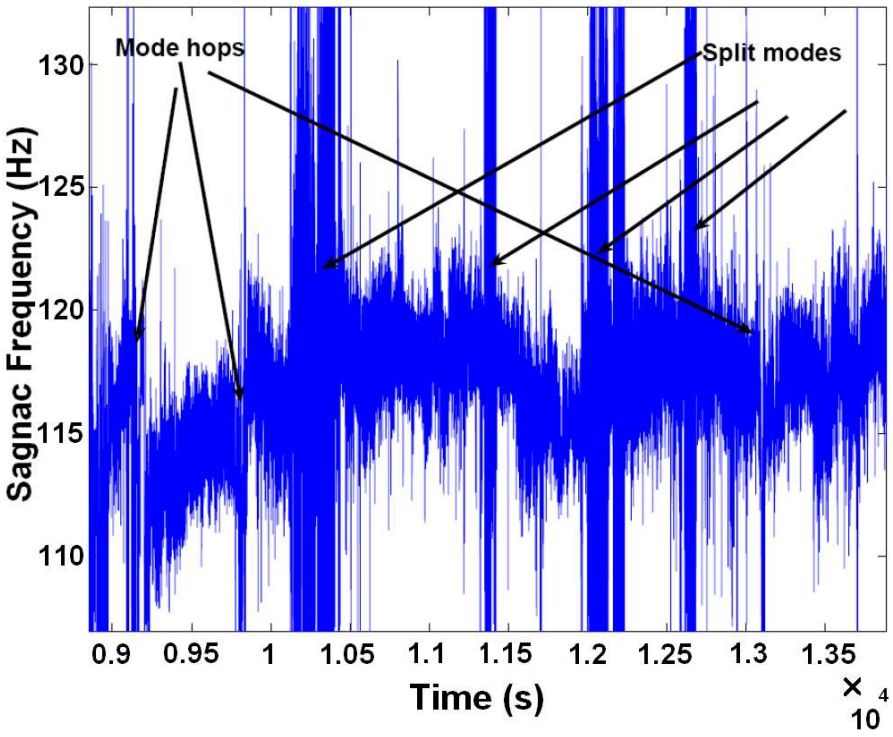

Figure 3.5: Sagnac frequency time series obtained from PR-1 after optical alignment in December 2007.

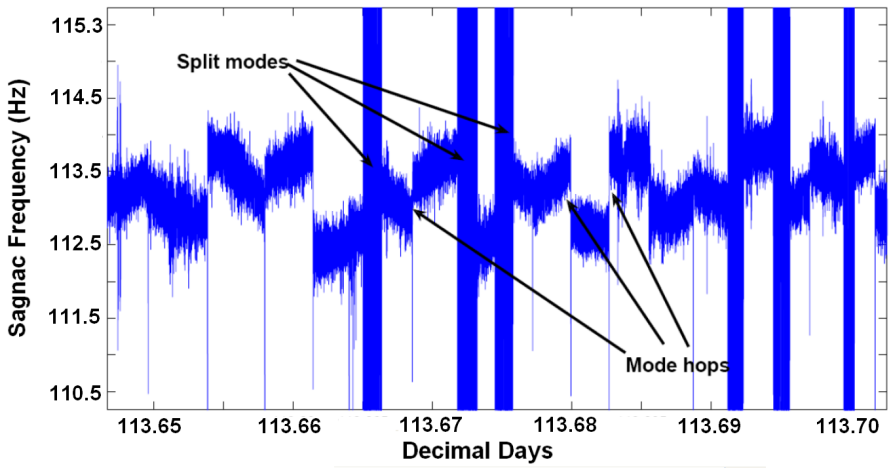

Figure 3.6: Sagnac frequency time series obtained from PR-1 after cleaning the supermirrors.

3.1.3 Cleaning the Supermirrors

The supermirrors are TiO_2-SiO_2 dielectric stacks with a nominal reflectivity of 99.99997 %. The mirrors had not been cleaned since manufacture. Prior to the removal of the mirrors helium gas was used to bring the PR-1 cavity up to atmospheric pressure in order to minimise the accumulation of dust in the cavity. Then the mirrors could then be removed and placed in sealed containers for cleaning in a clean-room environment.

Meanwhile a 3 mW He-Ne laser is used to illuminate the mirror surface so that scattering centres can be identified through a low magnification optical microscope (fig 3.7). Acetone[1] and deionised water[2] are applied with a cotton swab to the rotating surface to remove the scattering centres.

After cleaning the mirror surfaces only 4 scattering centres could be observed. By contrast the entire surface of a standard laser mirror (having 99.9 % reflectivity) would be illuminated through the multitude of scattering centres present.

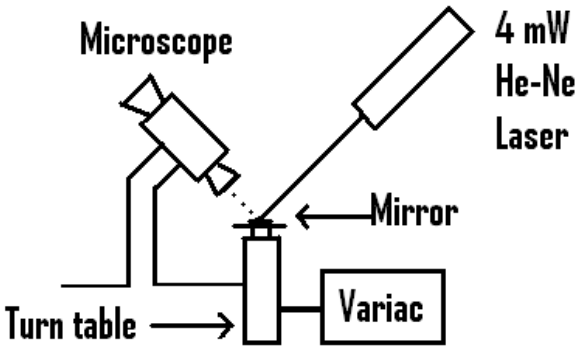

Figure 3.7: Mirror cleaning apparatus.

3.1.4 Supermirror Transmission Measurement

Modern supermirrors are characterised by total losses well below 10 parts per million. This translates into both scatter and transmission losses (absorption is negligible). In order to infer the true circulating intra-cavity power (from the transmitted beams), a measurement of the actual mirror transmission at the laser wavelength is required. In order to do this, some care is required since the mirrors are made from a dielectric multilayer coating and

[1]Because of its medium polarity acetone dissolves a wide range of compounds and therefore also was sprayed onto the mirror to act as a solvent.

[2]Deionised water is used to prevent contamination of the surface by impurities usually found in water.

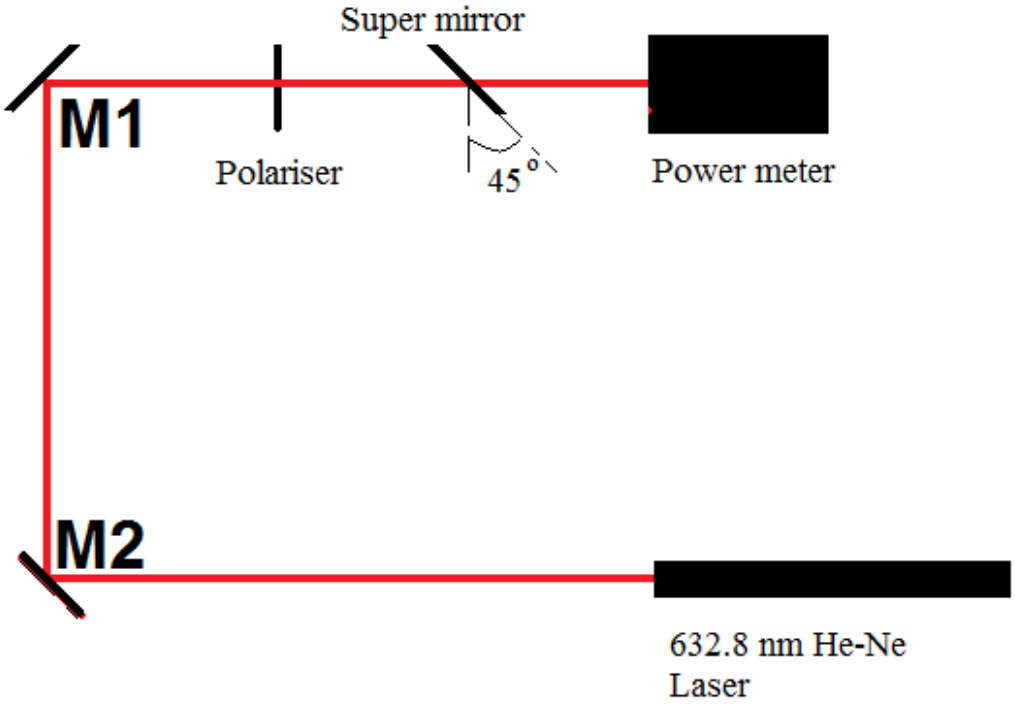

Figure 3.8: Experimental setup for the transmission measurement.

have extreme sensitivity to the polarisation state of the laser. The test beam for these measurements is derived from a 14.44 mW, 632.8 nm He-Ne, however; it was not strictly linearly polarised. To find the polarisation plane, a glass block (with a Brewster angle of 56.3^0) was placed between the polariser and mirror one (fig 3.8). The plane of the glass block is the same as that of the table the experiment was setup on. So the laser beam is reflected on to the roof of the lab. The laser was then rotated until the beam was at the lowest intensity. This occurs when the laser beam is mostly polarised perpendicular to the table. Once this is done the polariser is used to further remove any scattered light. Mirror two is used to increase the distance between the laser and the super mirror to minimise the plasma light. The supermirror was angled at 45^0 to mimic its orientation in PR-1. When the laser beam is perpendicular to the bench, the polarisation is in the same orientation as in PR-1. This gives the transmission of the supermirror at the centre to be 0.7 ppm. It was surprising that the mirror transmission varied when the mirrors were moved away from the centre. The highest value recorded was 39 ppm, indicating the coating in the mirror was not uniform. Fortunately in PR-1, the beam is reflected at the centre of the mirror. It is interesting to note that when the laser beam is rotated further by 90^0 the transmission is 399 ppm.

3.2 Measurement of Laser Stability

3.2.1 Allan Variance

The detailed method of how the Allan variance is calculated is given in section 2.3.1. Both before and after cleaning the mirrors the laser was run at a pressure of 5.8 torr of helium and 0.15 torr of natural neon. The Allan variance of plot in figure 3.9 show that cleaning the mirrors has a substantial effect. An order of magnitude improvement in the performance of the laser is observed. This corresponds to a peak sensitivity to rotation of 96.5 mHz (out of 475 THz) at an integration time of $\sim$ 5 seconds. The difference in the noise levels is readily apparent in figures 3.5 and 3.6.

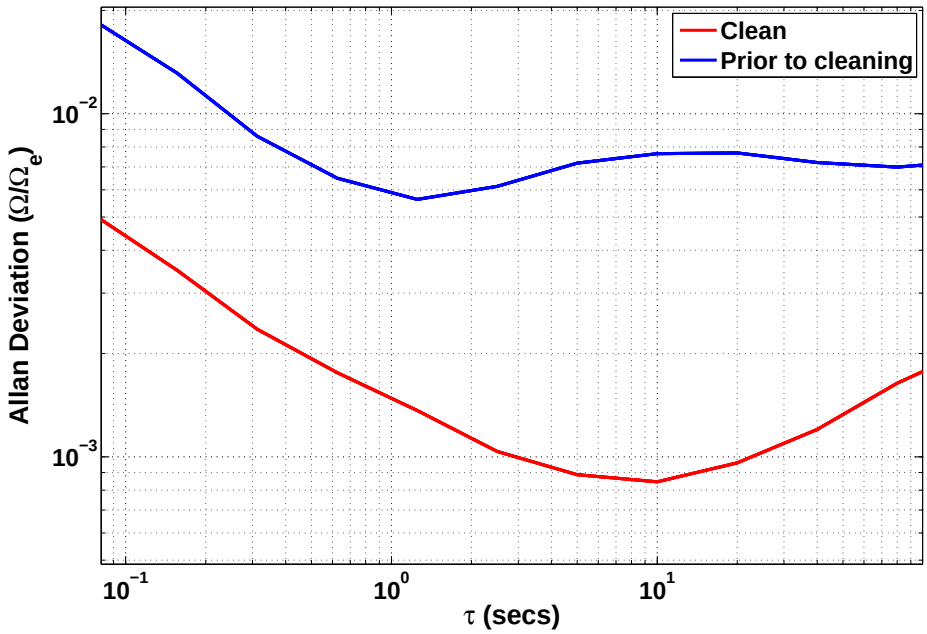

Figure 3.9: Allan variance plot derived from two data sets: one taken prior to cleaning the mirrors, the other after cleaning. The Allan variance is normalised with earth's rotation (Ω_e).

3.2.2 Beam Scatter from the Cavity Mirrors

Deposits on the mirror surfaces and imperfections associated with either the dielectric coating or the polish of the substrate will cause some scattering of the intra-cavity beams. Generally, this effect will increase as the mirror ages and with the time between mirror

cleans. A particular problem in ring laser gyroscopes is the degree of *backscatter*. For our purposes, backscatter is that portion of a single beam scattered directly into the beam path of the counter-propagating intra-cavity beam. This leads to coupling between the two nominally independent oscillators that comprise the two oppositely directed cavity modes. This gives rise to both frequency (Adler) pulling and an amplitude modulation of a single beam (so called *monobeam modulation*) at the Sagnac frequency ($\sim$113.5 Hz for PR-1)

We have measured the monobeam modulation both before and after cleaning the mirrors. The ratio of the modulation amplitude to the raw DC level due to a single beam is used as a figure of merit. Prior to cleaning the mirrors we find that this ratio is twenty two percent whilst after cleaning the mirrors it is reduced by around an order of magnitude to three percent. Thus, it is remarkable that PR-1 operated in a rotation sensitive regime at all prior to cleaning the mirrors since the backscatter was clearly significant, which should have extended the rotational dead-band such that the Earths rotation was an insufficient bias to unlock the laser.

3.2.3 Cavity Ringdown

The cavity ring down measurement was performed in order to check the overall finesse of the cavity and associated losses due to the mirror surfaces. Thus, it is a useful test of the quality of the mirrors and the success of the cleaning process. To perform this measurement the plasma was turned off using a CX-600N coaxial-relay which acts as a fast switch (fig 3.10). Coaxial termination with a 50 ohm characteristic impedance was used to absorb almost all of the incident power with a minimum amount of reflection when the relay was triggered. Care was taken to reduce the length of the coaxial cable used. A low capacitance coaxial cable was used between the photomultiplier tube and the oscilloscope. A 1 MΩ resistor was also added in parallel to the oscilloscope to further decrease the resistance and hence the RC time constant. This extra precaution was taken so that the decay time reflects the photon decay not the decay of the signal in the measurement system. The oscilloscope was set on a manual trigger so that when the signal from the photomultiplier reaches the trigger level the oscilloscope begins measuring the voltage.

The decay curves prior to cleaning the mirrors and after cleaning are shown in figure 3.11. A single exponential function of the form:

$$y(t) = y_0 e^{\frac{-t}{\tau}} \tag{3.1}$$

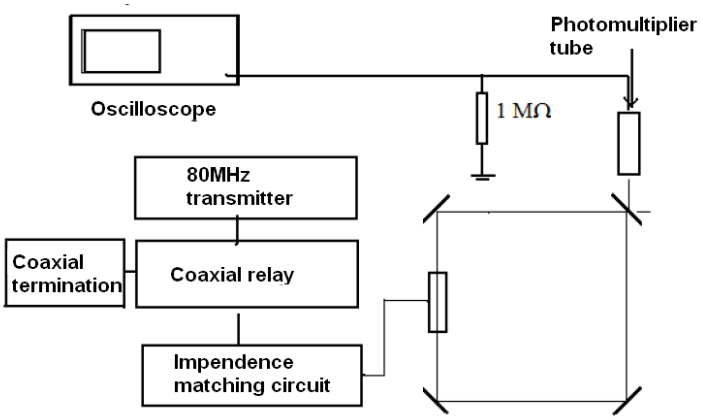

Figure 3.10: Schematic of the experimental setup for measuring ring down time

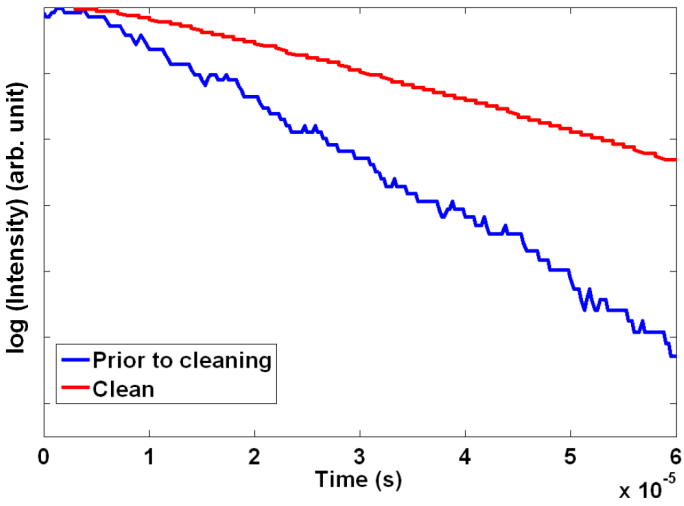

Figure 3.11: Cavity photon lifetime for PR-1 prior to cleaning the supermirror and after cleaning.

was fitted to the data. Prior to cleaning the ringdown time was 49.1 μs and after cleaning it increased to 97.4 μs. The associated quality factor Q of the cavity can be calculated using:

$$Q = 2\pi\tau\nu \tag{3.2}$$

here ν is the frequency of the laser and τ is the ring down time. The quality factor changed from 1.458×10^{11} to 2.898×10^{11} after mirrors were cleaned. The improvement of a factor of approximately two is quite remarkable.

Chapter 4

Dynamics of the PR-1 Laser Cavity Modes

In this chapter we use the shape of the helium-neon gain curve to model the cavity mode dynamics for the PR-1 ring laser. The dependence of the single longitudinal mode operating regime upon the helium-neon gas pressure and composition (as well as the neon isotope mixture) is investigated. We also present studies of a new regime of operation for which the laser runs on multiple longitudinal and transverse modes at high gas pressures and yet yields a stable Sagnac beat note. This approach is potentially useful to minimise the effect of mode hops and laser operation on different longitudinal mode indices for the counter-propagating intra-cavity beams. The influence of spectral hole burning on the mode stability is also discussed.

4.1 Modeling of the Gain Curves

The shape of the laser gain curve plays an important part in the stability of the cavity mode structure in a ring laser. Any reliable model should take into account the lifetime, collision and doppler broadening processes. This is done using a Voight line-profile, which combines all broadening mechanisms. The model also must take into account gain saturation for the clockwise and counterclockwise beams in the ring. Gain saturation burns a hole in the gain curve, which has an obvious effect on the spectral distribution of gain. A visual basic code which treats this situation has been developed by Dr. Bob Hurst [27] of this department. We outline the underlying physics in the next section, as the basis for the calculations presented here.

4.1.1 Calculation of the Voight Line-Profiles

The homogeneous susceptibility $\ddot{\chi}$ observed at frequency ν due to a single atom with resonance frequency ν_a can be written as [46]:

$$\ddot{\chi} \equiv -\chi_o^{''} \frac{1}{[2(\nu - \nu_a)/\Delta\nu_a]^2} \tag{4.1}$$

where $\chi_o^{''}$ is the unsaturated midband susceptibility, ν is the frequency and $\Delta\nu_a$ is the full width half maximum. The inhomogeneous contribution to the lineshape across from doppler broadening and is given by the Gaussian lineshape function (G):

$$G(\nu) = \frac{C}{\sigma} e^{(\nu-\nu_o)^2/2\sigma^2} \tag{4.2}$$

where C is a constant and σ is the root mean square spread of the Gaussian distribution. A saturation factor is added to the model to account for the hole burned by the clockwise (cw) and counterclockwise beams (ccw). The clockwise and counterclockwise beams burn their own holes. There will be two symmetric holes on the gain curve at frequencies ν_a (cw) and ν_b (ccw). The intensity of the saturating signal is I_1 (cw) and I_2 (ccw) at frequencies ν_1 and ν_2. The saturation intensities is given by I_{sat}. The total saturating factor($S(T)$) due to both beams is given by

$$S(T) = \frac{1}{1 + F(\nu_a, \nu_1, I_1, I_{sat}) + F(\nu_b, \nu_2, I_2, I_{sat})} = \frac{1}{1+F} \tag{4.3}$$

where:

$$F = \frac{I_1}{I_{sat}} \times \frac{1}{1 + [2(\nu_1 - \nu_a)/\Delta\nu_a]^2} + \frac{I_2}{I_{sat}} \times \frac{1}{1 + [2(\nu_2 - \nu_b)/\Delta\nu_b]^2} \tag{4.4}$$

Finally the Lorenzian, Gaussian and saturation contribution are combined to calculate total atomic susceptibility (ϑ) at the saturation intensities I_1 and I_2 by summing over all the homogenous line contribution . The total susceptibility is proportional to the gain and therefore, evaluating the integral below reproduces the spectral distribution of the gain.

$$\vartheta = \int_{-\infty}^{\infty} \ddot{\chi} G(\nu) S(T) d\nu \tag{4.5}$$

The model requires six input parameters; the doppler linewidth, the homogenous linewidth, the spacing between the ^{22}Ne and ^{20}Ne line-centres, the hole frequency related to the ^{20}Ne line position, and β_a=I_1/I_{sat} and β_a=I_2/I_{sat}

The Doppler width of the ^{22}Ne and ^{20}Ne line contribution is calculated using equation 2.23 to give 1.43 GHz and 1.50 GHz at 400 K using an atomic mass of 19.992 u and 21.991 u respectively [33].

The homogenous linewidth is calculated for different pressures using [11]:

$$\gamma = 8.5 + 59.5P \tag{4.6}$$

where P is pressure in torr. The atomic line centre of ^{20}Ne is 875 MHz apart from the ^{22}Ne [13].

There is a small difference between the intensity of the clockwise (I_1) and counter clockwise (I_1) beams present in all ring lasers, but this effect is ignored since the difference in intensity has only a small affect on the final result. This leads to the ratio I_1/I_{sat} of the clockwise beam (β_a) and ratio I_2/I_{sat} of the anti-clockwise beam (β_b)to be the same. In the rest of the chapter β_a and β_b are refereed to as β.

The last parameter is the laser operating frequency, which is determined to be at the peak of the non-saturated gain curve. Equation 4.5 is evaluated numerically to produce all of the relative gain curves shown in this chapter. The integral is normalised to give unity at maximum gain, so different gain curves can be compared. The constants associated with the Lorenzian and Gaussian curves are therefore eliminated.

4.1.2 Isotope Dependence of the Gain Curve

The shape of the gain curve varies with different neon isotope ratios. Naturally occurring neon is comprised of three isotopes: 90.48% ^{22}Ne, 0.27% ^{21}Ne and 9.25% ^{22}Ne [2]. In modeling of the He-Ne gain curves we may neglect the small contribution from ^{21}Ne. The atomic line centre of ^{20}Ne is 875 MHz apart from ^{22}Ne [13] and therefore the overall gain curve has two components shifted by this value, but dominated by the ^{22}Ne component. For a 50:50 isotopic mixture of ^{22}Ne and ^{20}Ne, the gain curve is essentially centred in between the two line profiles with a slight shift due to the difference in isotopic mass (fig 4.1).

In addition to changing the shape of the gain curve, the isotopes also affect the mode competition. If only one isotope is present, the clockwise and counter-clockwise beams will share the same set of atoms and this will cause one of the beams to extinguish [13]. In other words the hole burned by one beam eliminates the gain for the other. Fortunately both beams can be supported with a high degree of hole overlap [12]. In fact PR-1 can be operated with natural neon. Mode competition can also be further reduced by running the laser at 50% ^{22}Ne and 50 %^{20}Ne. For the rest of the text a 50% ^{22}Ne and 50% ^{20}Ne gas mixture will be referred to as 50:50 neon. This changes the gain curve such that it is more symmetric, although not completely so since there is a difference in the atomic

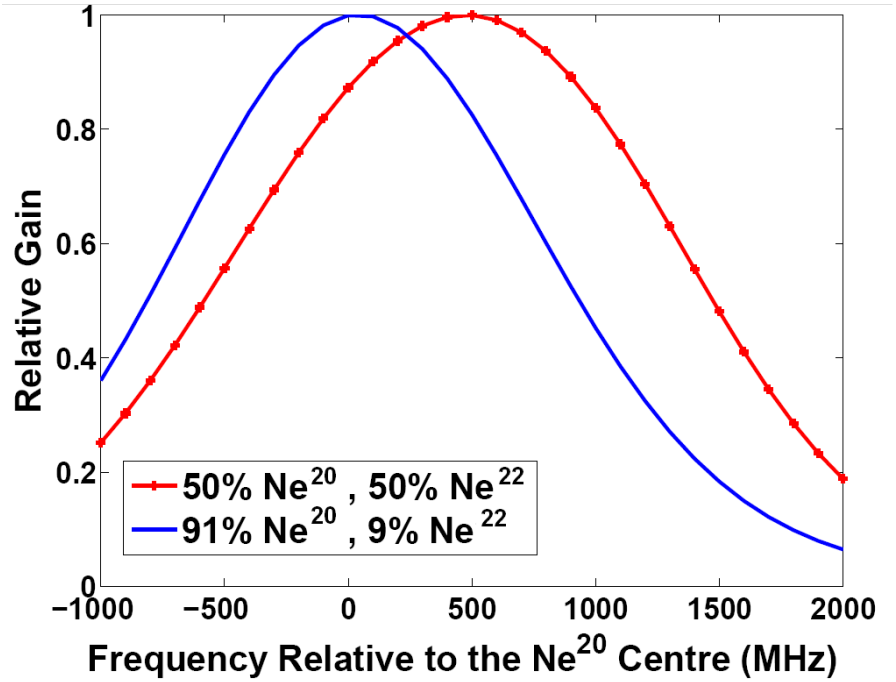

Figure 4.1: The gain curves for gas mixtures consisting of natural and 50:50 neon.

masses (fig 4.1). This decreases the hole overlap compared to natural neon and hence decreases the mode competition. This in turn allows the both beams to oscillate with greater stability than before [13].

4.2 Detection of Modes using Fabry-Perot Resonator

The Fabry-Perot Resonator (FP) with 25 cm confocal mirror was used to detect the modes present in PR-1. The free spectral range (FSR) for PR-1 is 46.8 MHz, hence in a single scan it is possible to scan through to six ($\frac{FP_{FSR}}{PR{-}1_{FSR}}$) cavity modes. Each of the longitudinal modes has corresponding transverse modes associated with it. The transverse modes for PR-1 have a frequency offset of 33.5 MHz for the out of plane direction and 23.0 MHz for the in plane direction [41]. When the order of the transverse mode increases the gain available for them decreases rapidly due to the increase in diffraction losses in the cavity. Figure 4.2 shows two longitudinal modes and two transverse modes associated with it.

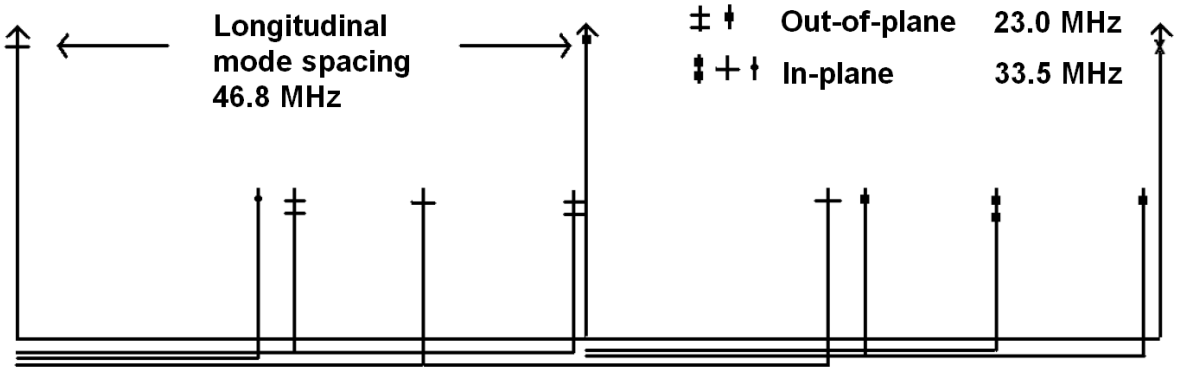

Figure 4.2: The diagram shows three longitudinal modes (large point up arrows). Two transverse modes in plane and two out of plane associated with the first two longitudinal modes are also shown. Notice that the mode pattern is degenerate.

4.3 Multi-Mode Threshold

The operation of ring lasers on a single longitudinal cavity mode is standard in interferometry. This is because multimode operation leads to random fluctuations in the amplitude of the Sagnac waveform. Since the modes in clockwise and anticlockwise beam are out of phase. Single mode operation is achieved by the gain starvation method, whereby the input power is reduced such that only a single mode is above the threshold [20]. The multimode threshold occurs when the gain curve is saturated (just before the hole burning process begins). Ideally the laser should be run away from either the lasing and multimode threshold. Near the lasing threshold, any increase in loss (e.g from gas degradation) would cause the laser to stop. A typical method used is to increase the pressure of the He-Ne gas. This causes an increase in the homogeneous linewidth (fig 2.2) causing the hole burned to be wider. Figure 4.3 shows the saturation of the hole increasing with pressure and β value for 50:50 neon. The increase in β value means that the intra cavity intensity needs to be higher to achieve the same level of saturation. The hole is burned at 475 MHz (1.5 torr) and shifts to 484 MHz (7.5 torr) from the ^{20}Ne line centre. The behavior of the gain curve is different for natural neon. The gain curve shows high asymmetry due to the large difference in the ratio of the isotope. As the pressure increases the point where the maximum gain occurs is pulled towards the ^{22}Ne linecentre. The legend in fig 4.5 shows that the frequency shift gets larger with pressure. Also, the β values for natural neon are consistently larger than 50:50 neon, so the multimode threshold should be larger for natural neon. The increase in β value means that the intensity of the signal needs to be higher to achieve the same level of saturation. In other words, the multimode threshold

increases with pressure. I_{sat} is also known to be strongly pressure dependent from earlier work done by P.W. Smith [49]. This combined effect of having higher I_{sat} and β values for higher pressure means the expected multimode threshold is highly pressure dependent.

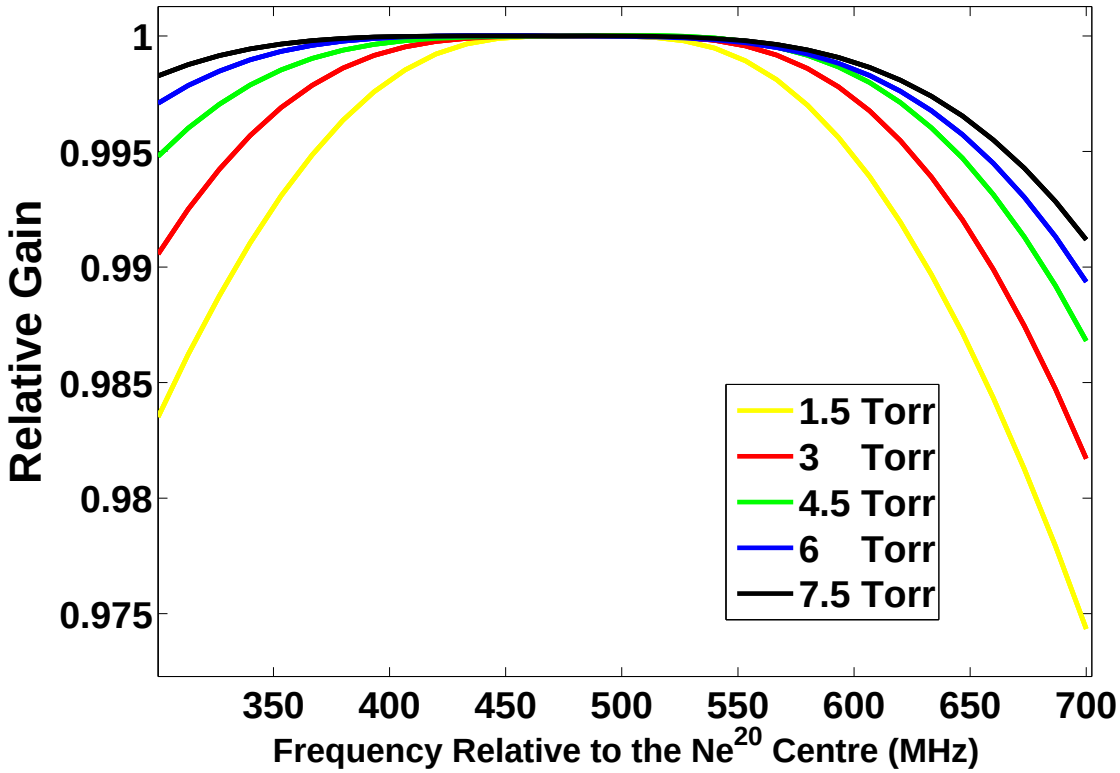

Figure 4.3: The relative gain curves for 50:50 neon at different pressure at the multimode threshold.

4.4 The Isotope Dependence of β

The atoms in the gain medium have a statistical distribution of velocities described by a Gaussian function. In a non-rotating ring laser, if the laser optical frequency is above the line centre freq, the clockwise beam has a tendency to saturate the atoms which are travelling in the same direction as the beam, while the counter clockwise beam will saturate the atoms traveling in the opposite direction [32]. This creates holes which are symmetric on both side of the gain curve [15] (fig 4.6 and 4.7). For natural neon there are three holes (A,B,C) near the operating frequency while for 50:50 neon there is only two holes (F,G-see figure 4.1). Having a greater number of holes near the operating frequency causes the β value for the multimode threshold to be consistently higher for natural neon

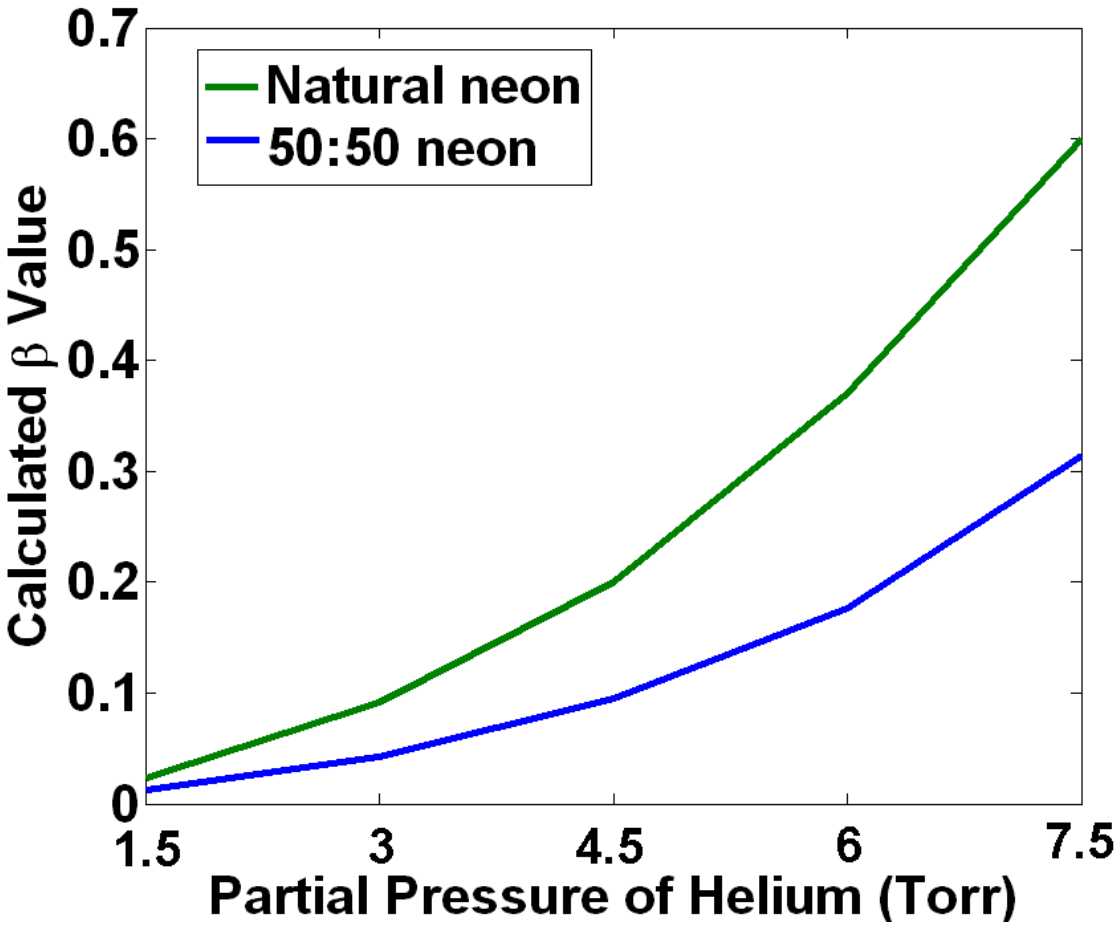

Figure 4.4: The calculated β at the multimode threshold for natural neon and 50:50 neon as a function of helium pressure.

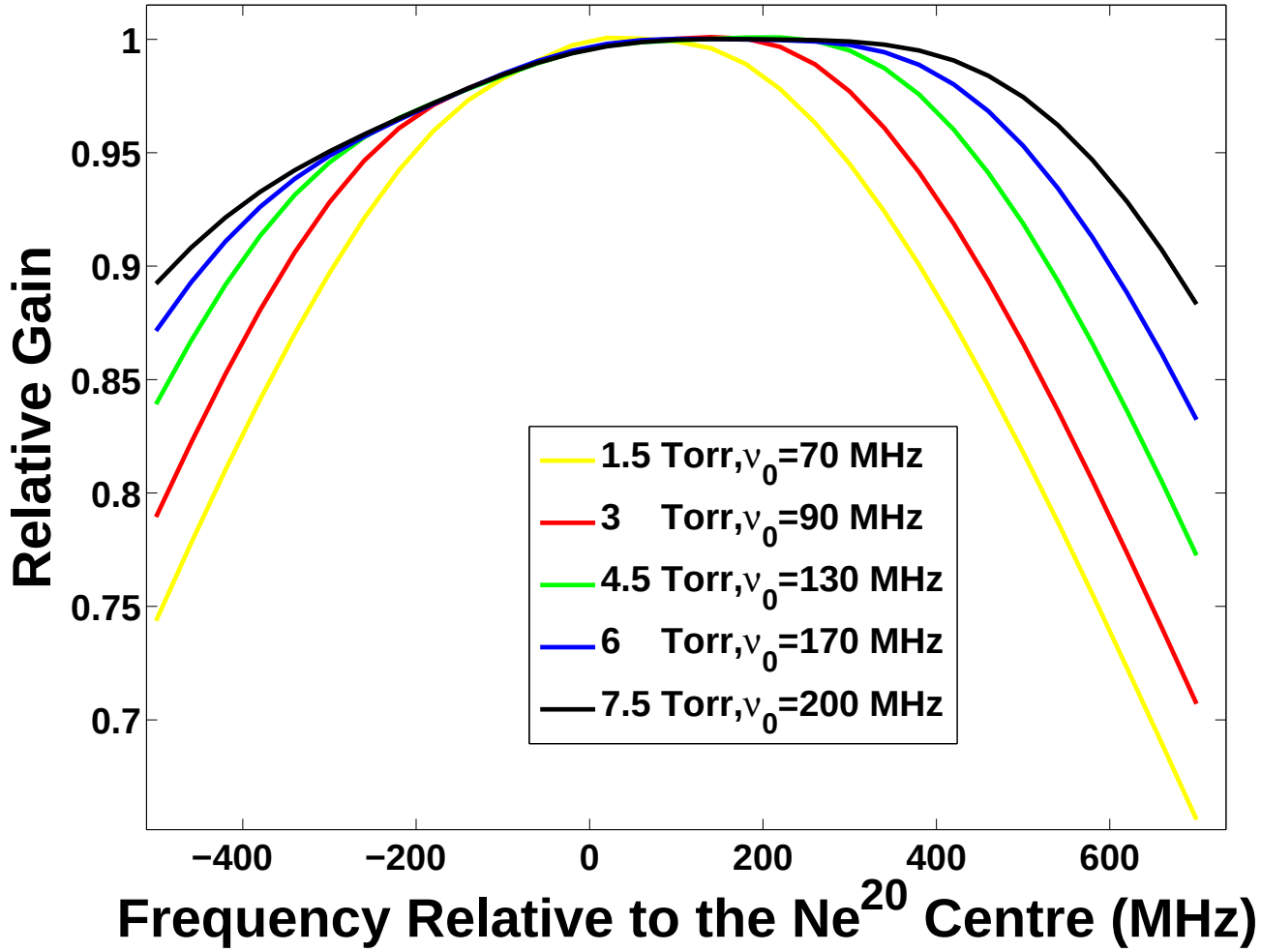

Figure 4.5: The relative gain for natural neon at different pressures at the multimode threshold. The frequency of the hole (ν_0) moves away from the ^{20}Ne centre with increasing in pressure.

than 50:50 neon. Also as mentioned earlier, the mode competition will be greater for natural neon than 50:50 neon at the same pressure.

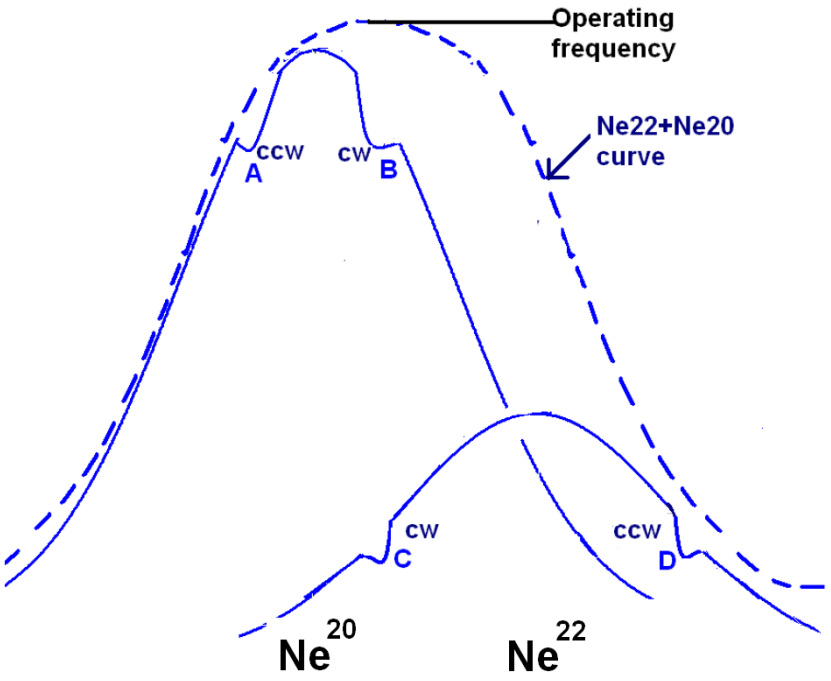

Figure 4.6: The sketch of gain curves for each isotope of neon present in natural neon. The dotted line is the combined line curve show in figure 4.1. Notice that holes B and C are close to operating frequency, followed by hole A then hole D.

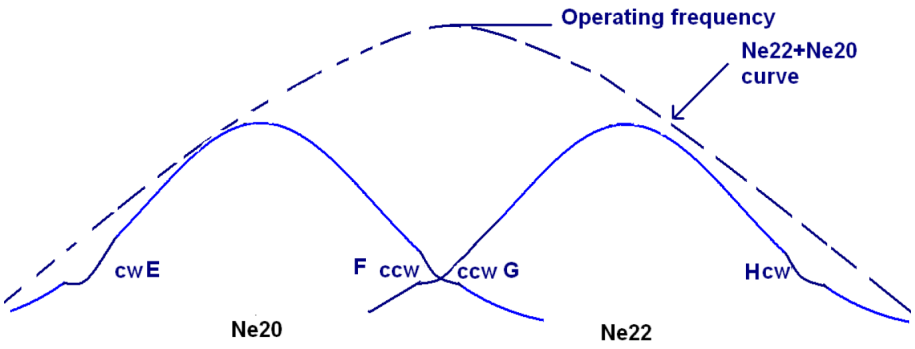

Figure 4.7: Sketch of the gain curves for each isotope of neon present in 50:50 neon. The dotted line is the combined line curve shown in figure 4.1.

4.5 Measuring Multimode Threshold and Laser Stability

Initially the vacuum is established in the cavity. This procedure begins by having all of the valves, other than the one attached to PR-1 are closed. Then all the stainless steel pipes are pumped out with the scroll pump. When the pressure drops to about 0.004 torr indicating that the molecular flow condition [25] is established, then the turbo molecular pump was turned on, while still maintaining a closed PR-1 valve (fig 4.8). Once all the pipes are under vacuum, the PR-1 valve is slowly opened. This procedure ensures that there are no impurities from the vacuum system getting into PR-1. This also produces a pressure gradient between PR-1 and the vacuum system preventing any material entering the cavity, which could cause degradation of the super mirrors. Once the pressure reaches zero[1] as indicated by diaphragm capacitance manometer (Edwards, Barocel) then the He-Ne gas was added. The gain tube in PR-1 has a 4 mm diameter. For this diameter the optimum Ne pressure is worked out by C.P Wyss to be 0.15 torr [56]. The partial pressure of neon has a small effect on the optimum pressure for laser operation [56]. For all the experiments the neon partial pressure was kept at 0.15 torr and the partial pressure of helium was varied. A 50:50 ratio of neon was achieved by mixing two parts of 70 $\%^{22}$Ne, 30 $\%^{20}$Ne and one part of natural neon. Once the gases were filled, the PR-1 valve was closed and the rest of the vacuum system was pumped out as a precautionary measure. This process is repeated for different partial pressures of helium. Once the gas was filled it was left for 15 minutes to mix, then RF power could be applied.

4.5.1 Mode Assignments at Higher Power

When the gas pressure is less than 1.5 torr, the lasing threshold and multimode threshold are very close together, which makes it a difficult task to measure the multimode threshold. Increasing the pressure causes the difference between the multimode and lasing threshold to increase, consequently making the measurement process simpler. Initially the laser was run under single mode operation (fig 4.9). When the laser is run about 1 nW above the multimode threshold the spectrum looks like that of fig 4.10. Table 4.1 shows all the modes that appeared after the multimode threshold. The spectrum was taken for neon 50:50 at 8.69 torr. Higher pressure was chosen since the mode behaviour was easier to observe, i.e. at lower pressures such as 2 torr the mode become chaotic with small changes

[1] the range of the manometer is 10^{-4} torr but the turbo pump can create a pressure of 10^{-6} torr

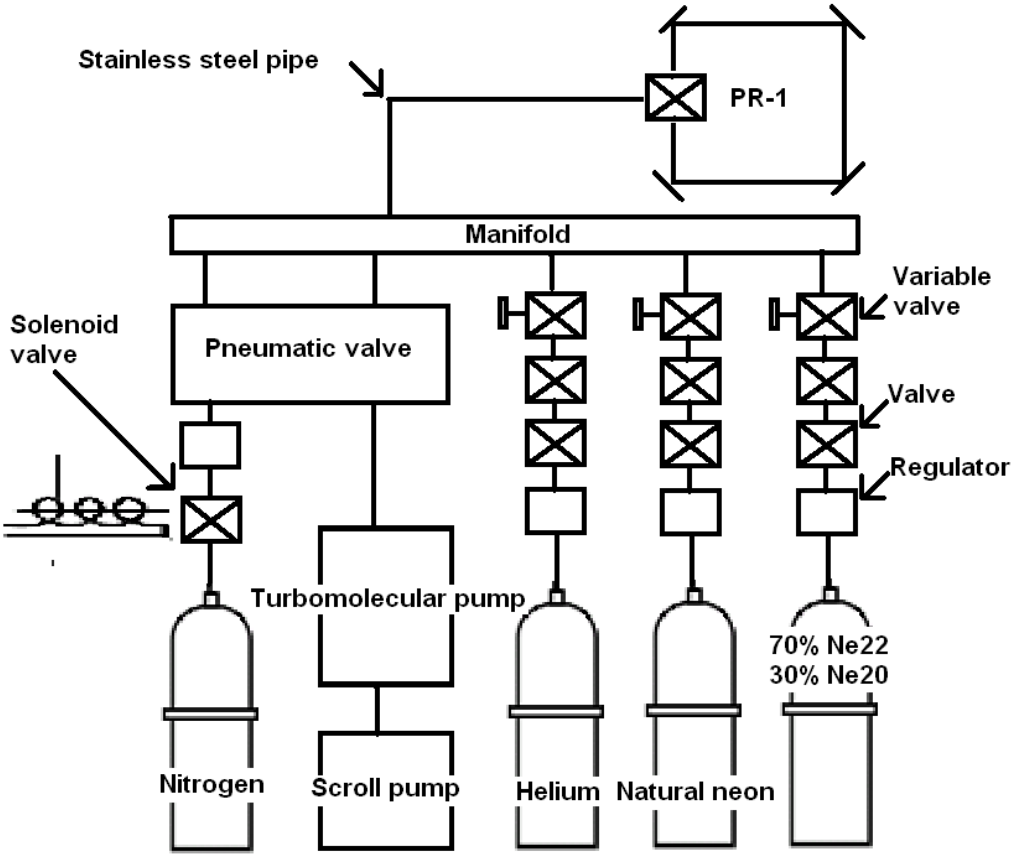

Figure 4.8: Schematic diagram of the vacuum setup.

in power above the multimode. This is possibly due to increased saturation at the higher pressure seen in fig 4.5. Burning a larger hole suppresses a larger number of modes, so there is less competition between the modes. When the power is increased to 0.5 nW [2] above the multimode threshold, the first mode to appear was mode TEM[3](1,0,-2) and TEM (1,0,1). Continual increase to 1 nW caused modes TEM (0,1,-3) and TEM (1,0,2) to appear. The last mode to appear was TEM (1,0,-1), which occurred when the power was at 1.5 nW.

[2]As measured from the transmitted beam through the supermirror

[3]TEM (x,y,z), where x is the order of the in-plane mode, y is the order of the out-of-plane mode and z is longitudinal mode index.

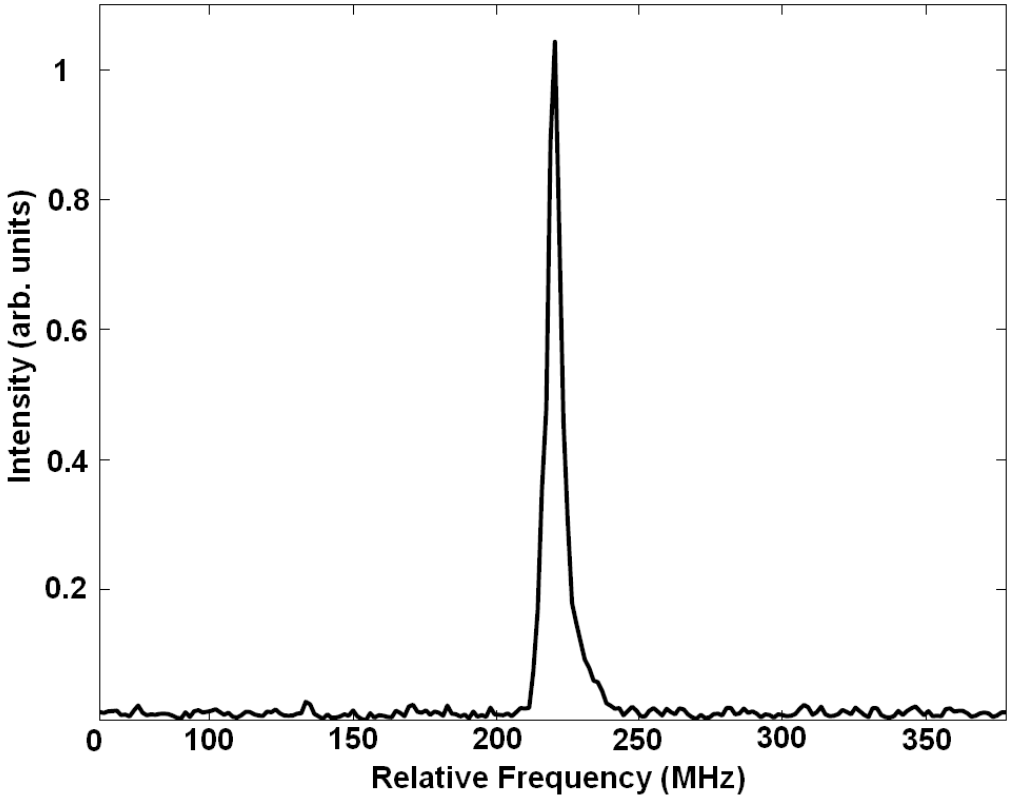

Figure 4.9: The laser spectrum under single mode operation.

4.6 Experimental Result for Change in Multimode Threshold

The laser output power was recorded when the TEM (1,0,-2) and TEM (1,0,1) modes became visible (fig 4.10) on the FP scan, indicating the multimode threshold had been reached. The meter reading can then be converted to intra-cavity intensity using the measured mirror transmission and calculated beam diameter of 2.6 mm. Figure 4.11 shows the experimental results for multimode threshold for various partial pressure of He. The multimode threshold for 50:50 neon is consistently lower than for natural neon. This was expected from the gain curve calculations, which shows β values are almost half the value for neon 50:50 (fig 4.4). The natural neon data points are more scattered than the 50:50 neon data especially at lower pressure. This reflects the fact that multimode threshold is harder to find due to the asymmetry of the natural neon gain curve. The frequency of the hole burnt also continually changes with pressure for natural neon (fig 4.5), so the hole is burnt at different places in the gain curve. This may account for the difference. The multimode threshold does rapidly increase in figure 4.11 as expected from

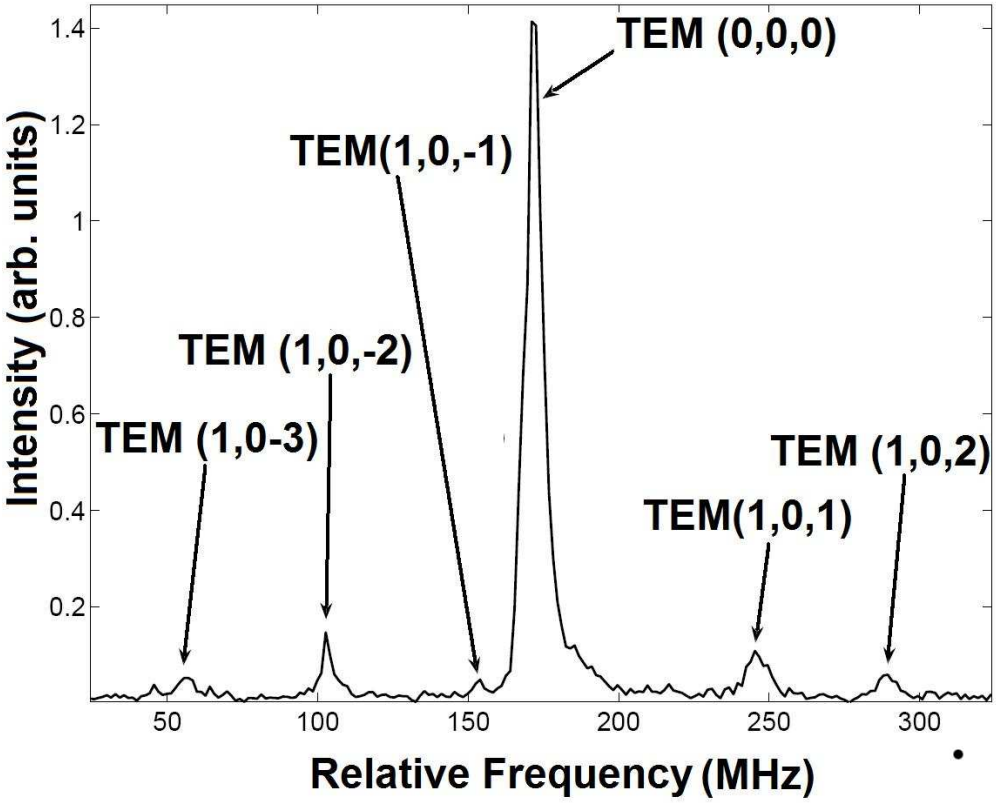

Figure 4.10: Laser spectrum for an output power 1.5 nW above the multimode threshold.

the rapidly increasing β values indicated in figure 4.4.

4.7 Frequency Stability of the Sagnac Waveform Versus Pressure and Isotope Mixture of the Gain Medium

Figure 4.12 shows the normalised Allan variance plot with the laser running on a single mode with different gas pressure and isotopic mixtures. For natural neon, as the pressure increases the stability of the laser increases, as indicated by the downward shift in the Allan plots as the pressure increases (fig 4.5). This is due to the fact that it is possible to run the laser at higher power for operation at higher pressure. This increases the number of photons in the cavity, hence increases the stability of the laser. Mode competition also increases with pressure due to the increased hole overlap (fig 4.6), but the improved photon statistics dominate. The mode competition is much lower since the holes E and

Mode	Mode spacing (± 8 MHz) [4]	Origin
TEM (1,0,-3)	-117	-3(46.8)+22
TEM (1,0,-2)	-68	-2(46.8)+22
TEM (1,0,-1)	-27	-1(46.8)+22
TEM (0,0,0)	0	Longitudinal mode.
TEM (1,0,1)	+70	1(46.8)+22
TEM (1,0,2)	+117	2(46.8)+22

Table 4.1: The modes present when PR-1 just reaches 1 nW above the multimode threshold. Origin column represents multiple of FSR plus in-plane mode (22 MHz). The negative sign means mode is left of the TEM (0,0,0)

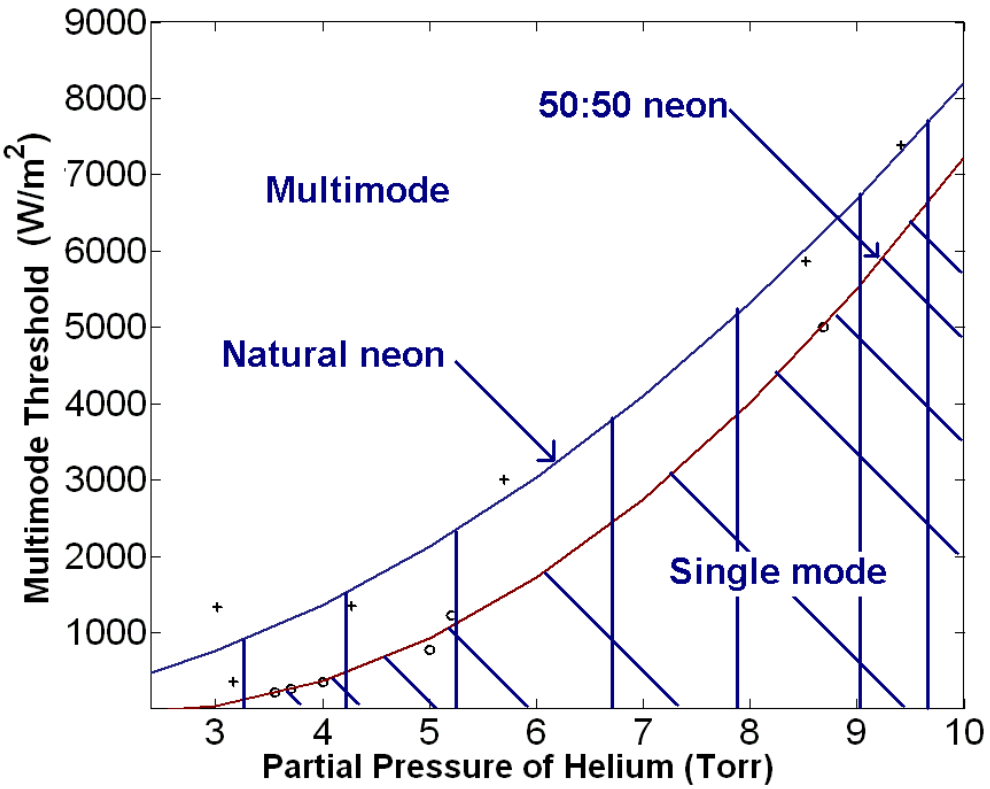

Figure 4.11: The intra cavity multimode threshold for natural neon and 50:50 neon. The shaded area under the curve represents single mode operation.

H are far apart for the operating frequency of 50:50 neon. Therefore, all the 50:50 neon plots have lower variance than natural neon. It was possible to run PR-1 at pressures up to 10 torr. It was not run higher than this pressure since the maximum measurable pressure was 10 torr with the current capacitance monometer setup.

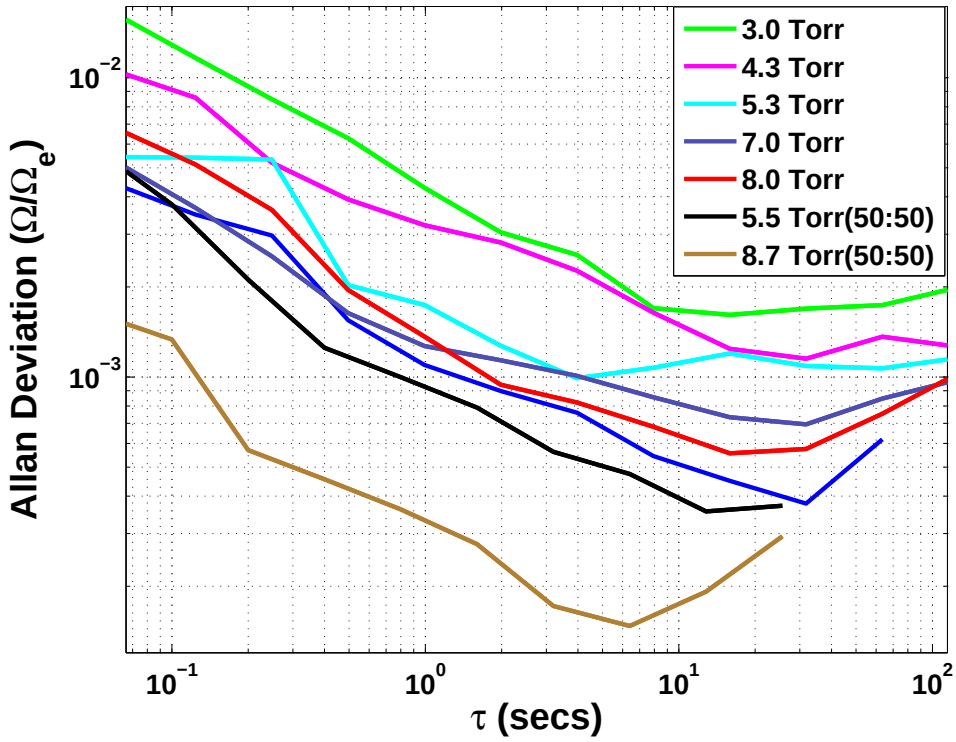

Figure 4.12: Allan variance plots for various pressures and isotopes. 50:50 stands for a gas mixture with 50% ^{22}Ne and 50% ^{20}Ne.

4.8 Stability of the Laser Cavity Modes

The amplitude stability of the cavity modes in PR-1 is affected by environmental factors (i.e. temperature fluctuations, building noise, nearby traffic, etc). These effects can be seen in the real time laser spectrum as small jitters and a slow frequency drift due to expansion and contraction of the laser cavity. Under single longitudinal mode operation the gain curve is as shown in figure 4.1 with only one cavity mode supported. As the cavity dimensions change, another mode may replace the first, whilst still maintaining single mode operation. This effect is known as mode hopping, and is evidenced in figure 3.6. It is known that mode hops occur more frequently in PR-1 than in other ring lasers operated by the Canterbury group. This is so because PR-1 is heterolithic in construction and mounted to a high rise building whereas the other devices are situated in the Cashmere cavern which is extremely stable by comparison.

When a hole is burnt, it adds complexity to the gain curve by creating a dip, which allows for higher gains at the wings of the curve as shown in fig 4.13. This can cause more than one mode to be able to be supported by the gain curve, and as the cavity dimensions

change, the different modes can have different gain at any given time. Monitoring the multi-mode spectrum with the spectrum analyser as a function of time illustrates this point (figure 4.14) with different modes popping in and out as they scan through the gain curve. Under these conditions, the Sagnac waveform has a randomly modulating amplitude due to the multiple modes which indicate that the signal is not in phase.

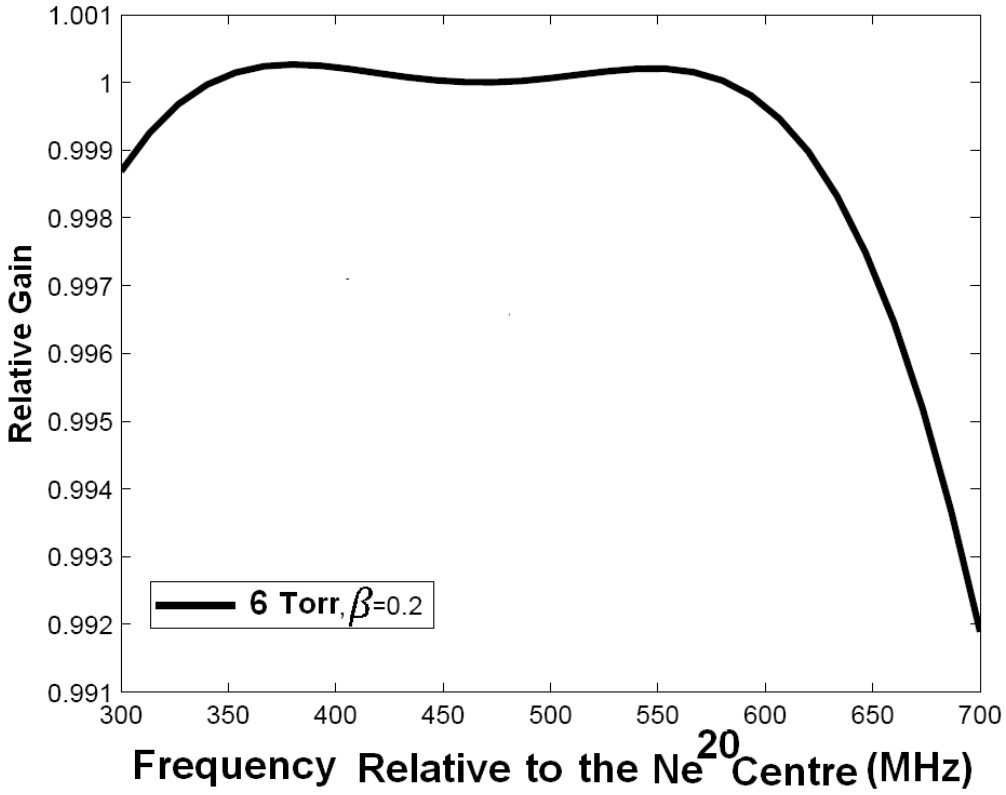

Figure 4.13: Saturation of the gain curve above the multimode threshold.

4.9 Stable Amplitude Multi-Mode Patterns

4.9.1 Low Pressure Operation

Under certain conditions, it is possible to run PR-1 on multiple longitudinal cavity modes whilst still maintaining a stable amplitude Sagnac waveform. This is important because it may then be possible to run the laser at higher powers and concomitantly improved photon statistics. This situation is equivalent to requiring the laser to be mode-locked (or potentially phase locked - with the longitudinal cavity modes having a non-zero but fixed phase relationship), albeit without the production of a pulse train at a frequency given by

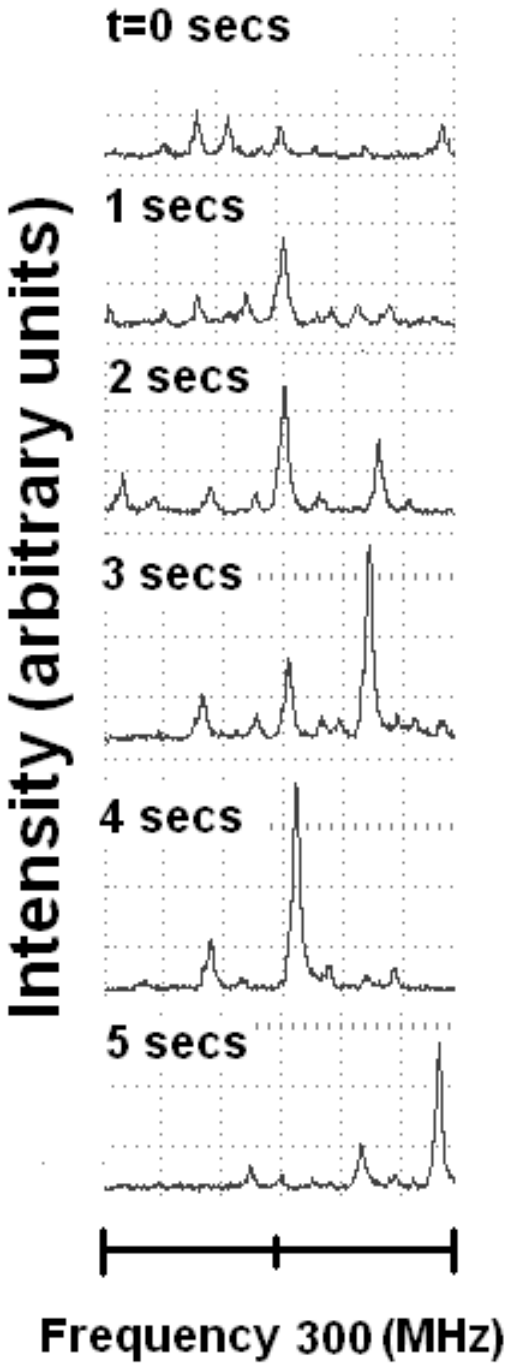

Figure 4.14: The mode behaviour above the multimode theshold. Some of the modes get stronger while others disappear as the dimensions of the cavity changes.

the reciprocal of a cavity round trip time. This is known as FM mode locking [10, 38, 48]. We have attempted to make some preliminary observations of this phenomenon and study the influence of variations in the helium-neon pressure as well as the isotopic mixture upon the stability of the Sagnac waveform.

As stated earlier, lowering the helium pressure to (lets say) $\sim$ 3 torr allows for the multimode threshold to occur at a lower intra-cavity beam power. It seems logical to begin at this point since the dynamic range above the multi-mode threshold is largest. As expected, when the laser powers are increased above the multi-mode threshold we see the mode amplitudes fluctuate randomly. In fact at the very lowest pressures (or when using natural neon) the laser is least stable and this adds to the difficulty of identifying operating parameters which yield a stable amplitude mode pattern. It was possible to identify such a case with a partial pressure of 3.11 torr of helium and 0.15 torr of natural neon. Notably the stable pattern (figure 4.15) occurred at an output power 13 times greater than the multi-mode threshold. Exactly what induces the locking phenomena is currently unknown. In passive (AM) mode locked lasers, such as short pulsed Ti:Sapphire lasers, locking is induced by a noise spike in the cavity leading to Kerr lensing. Nothing comparable can occur in this case however the cavity dimensions are fluctuating. Figure 4.16 shows the Sagnac frequency as a function of time, for stable multi-mode operation. After some time the laser appears to come out of 'lock' and the Sagnac frequency modulates randomly over $\sim$ 10 Hz.

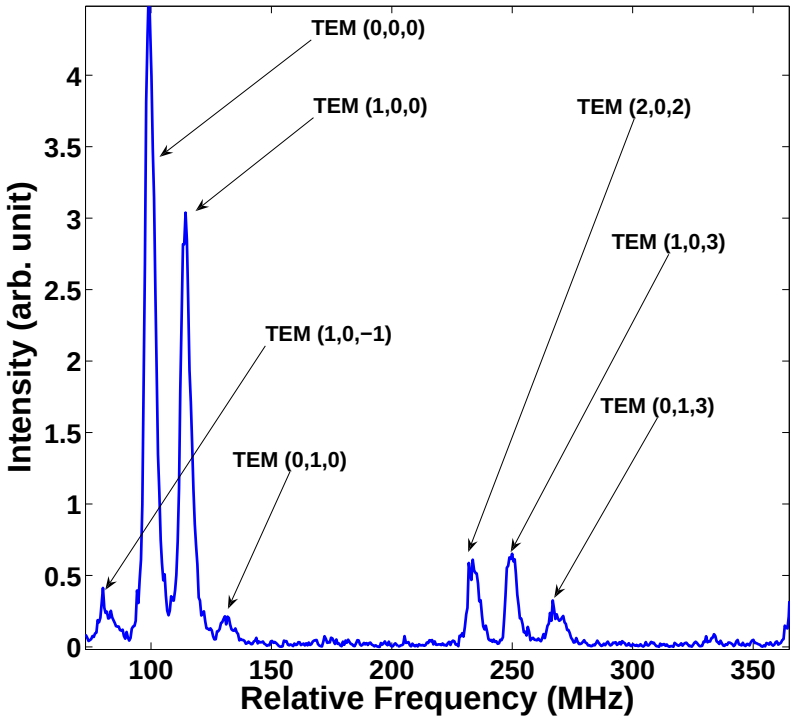

Figure 4.15: The laser spectrum of the stable pattern occurred at 3.11 torr of He and 0.15 torr of natural neon. Higher order modes are supported since the laser is running 13 times higher than the the multimode threshold (1.46 nW).

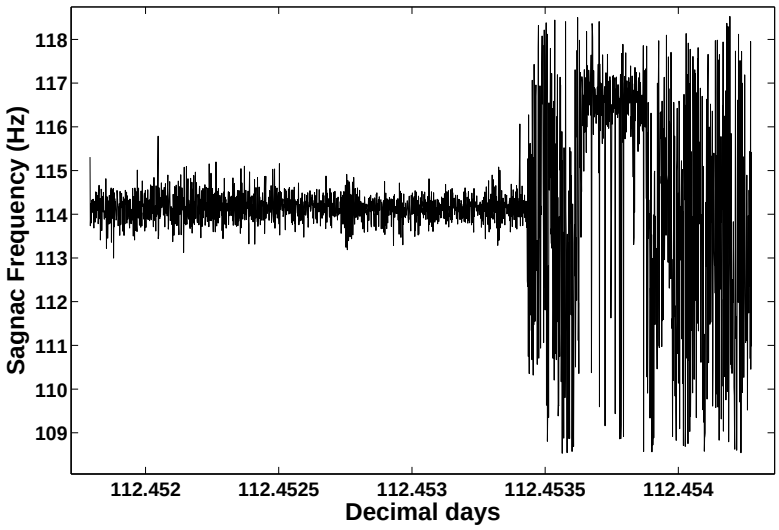

Figure 4.16: The Sagnac frequency as a function of time for a stable amplitude. The stable pattern corresponds to the Sagnac frequency is shown in figure 4.15.

4.10 High Pressure Operation

This 'mode-locked' behaviour is most readily observed if the gain medium is operated at high pressures and with a 50:50 isotope mixture. This may indicate a favoured distribution for the gain curve. The 50:50 neon mix is ideal, possibly for the same reason it is preferred in single mode operation, because mode competition is lower (section 4.1.2). Higher pressure is also preferred because of the large homogenous linewidth causing the hole burned to be less steep than at lower pressure. This allows for other modes to survive as the gain difference is not as high between the dominant mode as between the side modes. Figure 4.17 shows the laser spectrum as read from the oscilloscope at different powers above the multimode threshold at 8.69 torr helium, 0.15 torr of natural neon. Both the Sagnac waveform and the laser spectrum are displayed at each power. For each plot the y-axis of the Sagnac waveform is identical. From the plots it appears that the number of cavity modes simultaneously running does not determine the amplitude of the Sagnac waveform. This may suggest that when the counter propagating beams are recombined the interference is not fully constructive due to the differing phase factors between each mode. In turn, this may suggest that we observe phase locking as opposed to what is rigorously defined as mode locking. We further note that the period over which the pattern remained stable in each case is around 1 second. However figure 4.18 shows an amplitude stable multi-mode laser spectrum (i.e. that yields a stable Sagnac waveform) obtained at 88.9 nW above the multi-mode threshold. This pattern is remarkably robust and remains stable at all times investigated here. We also note that the Sagnac contrast (the ratio of the Sagnac waveform amplitude to the DC voltage from the combined cw and ccw beams) varies from 0.2 to 1.4 for various multimode patterns.

Figure 4.19 shows an additional pattern demonstrating similar characteristics (in other words, long time multi-mode stability) but obtained using a gas mixture with 0.15 torr of natural neon and 9.42 torr of helium. No obvious correlation exists between the two patterns.

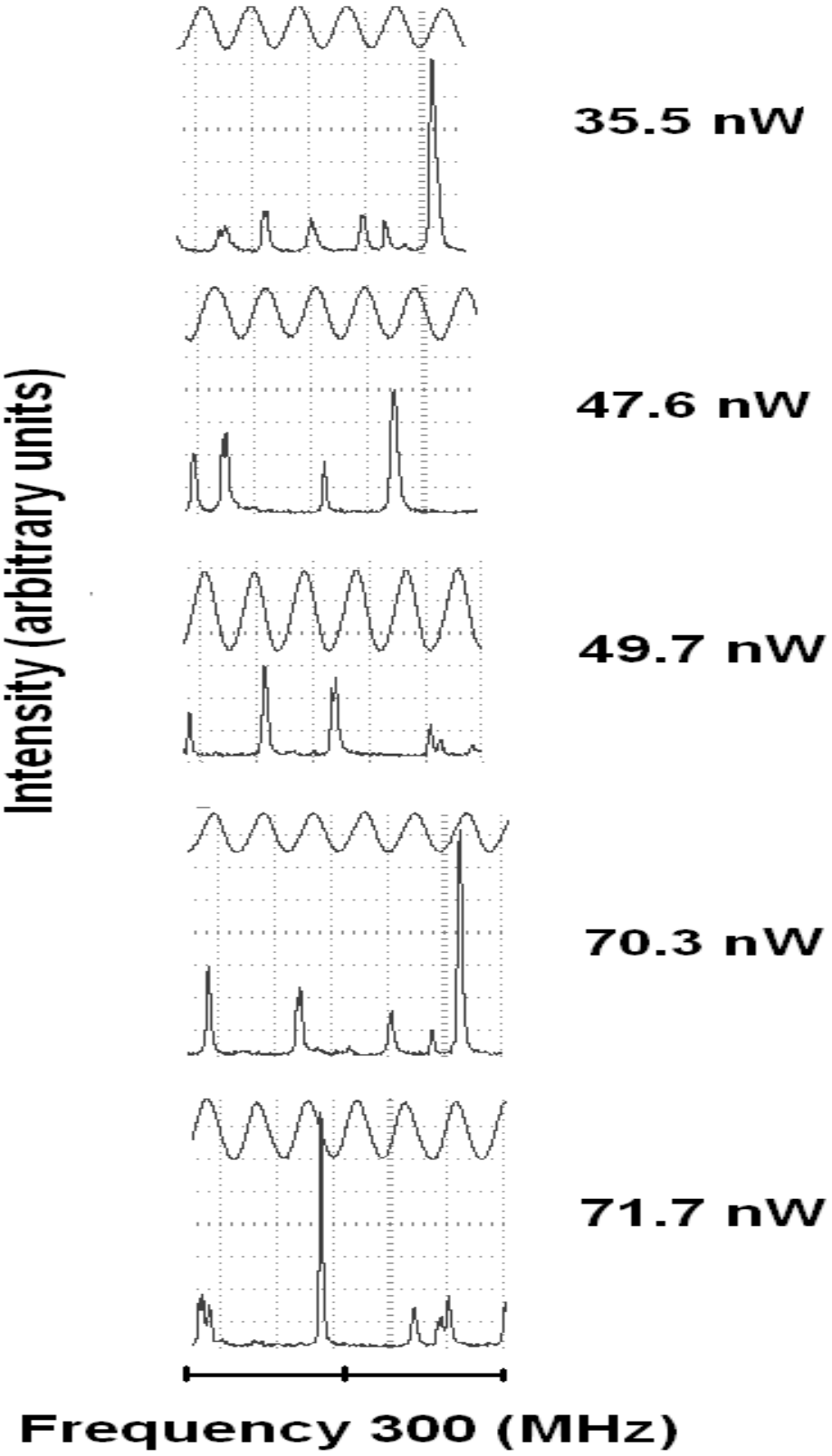

Figure 4.17: PR-1 laser spectra taken at different power above the multi-mode threshold (indicated on the right). The sinusoidal signal at the top of each spectrum is the Sagnac Waveform.

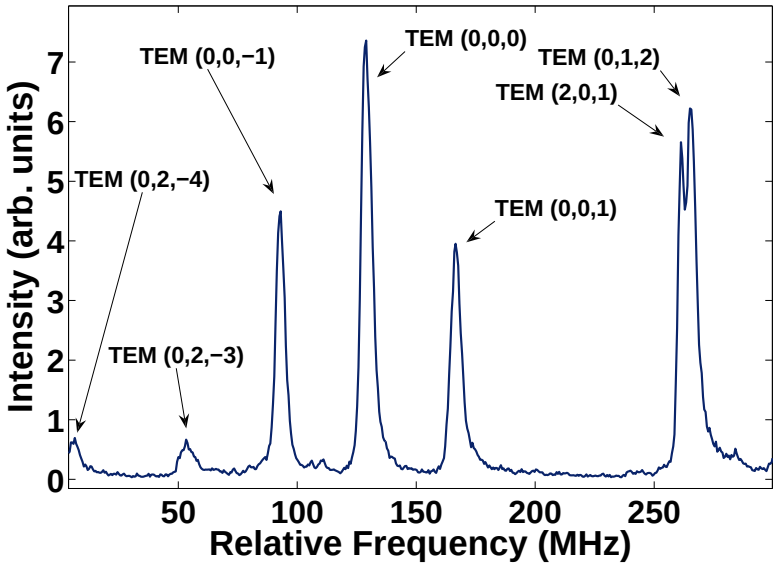

Figure 4.18: The stable mode pattern at 9.42 torr of helium and 0.15 torr of natural neon.

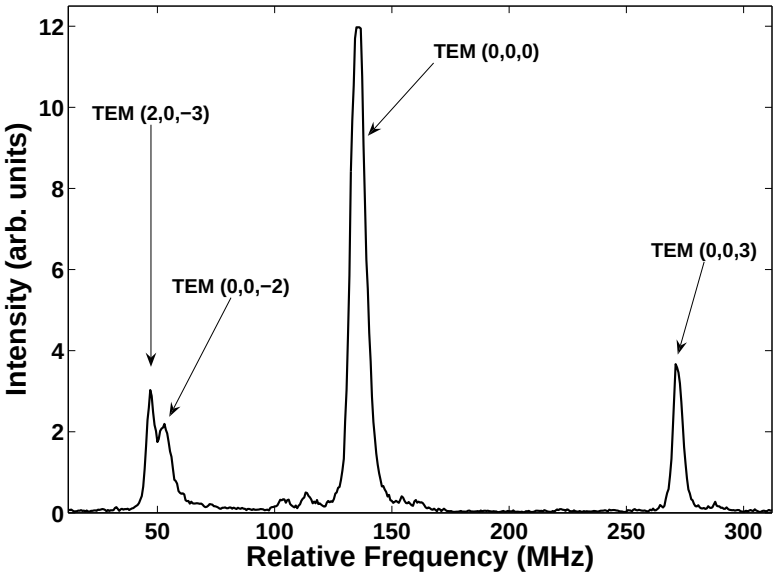

Figure 4.19: The stable mode multimode pattern at 8.68 torr of helium and 0.15 torr of 50:50 neon.

4.11 Comparison of the Allan Variance Plots

Figure 4.20 shows the Allan variance for four different regimes of operation for the PR-1 laser. Whilst the single mode plot is marginally the most stable regime of operation, it is clear that the multi-mode results are comparable. It is also worth pointing out that the multimode regime will not experience mode hops and therefore will yield stable long-time data not possible with single mode operation. Single mode operation is limited to time-periods of roughly 8 minutes between mode-hops.

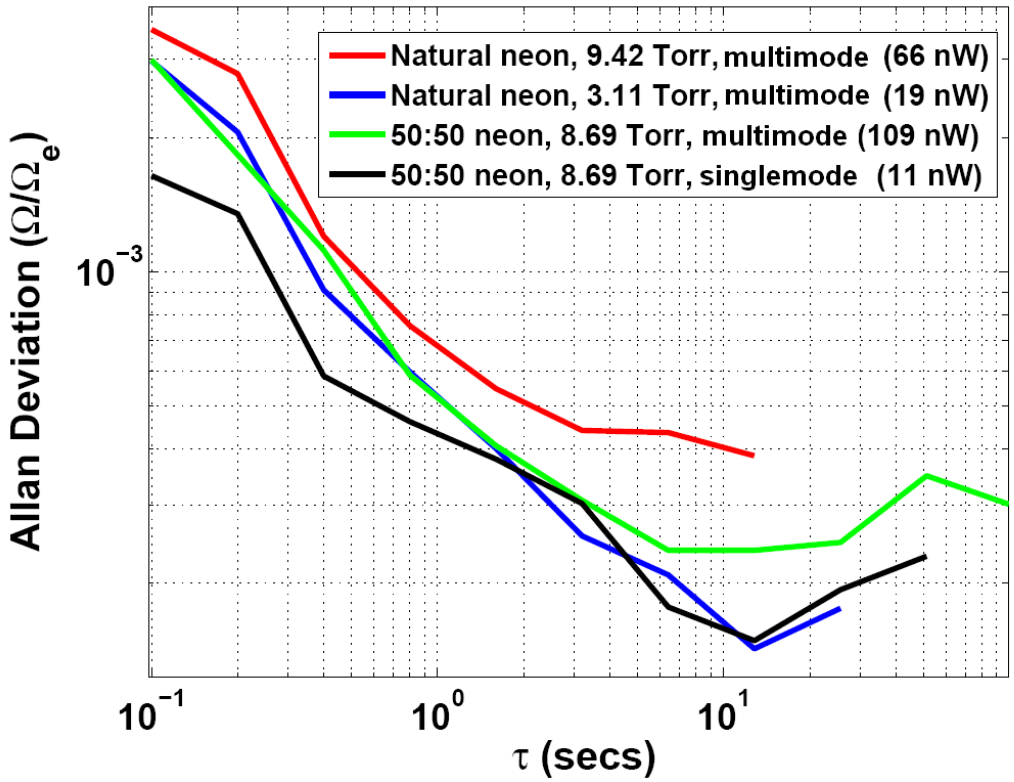

Figure 4.20: The allan variance plot comparing the single mode operation with various multimode regimes

Chapter 5

Observations of the Dynamics of a High-Rise Building

The PR-1 ring laser is mounted vertically on the structural wall of a high rise building (the Rutherford building on the central campus of the University of Canterbury). In this chapter we present some preliminary measurements of the dynamics of this building using the PR-1 ring laser gyroscope.

5.1 Natural Oscillations of the Rutherford Building

A complete analysis of the behaviour of the Rutherford building is too complex and therefore a few assumptions are necessary to simplify the problem. We assume that the building is isotropic, compressionally stiff along the column and very flexible in inter-story sheer. With these assumptions, the building deformation can either be dominated by bending or shear. Bending mainly occurs in buildings which are tall and have a small base surface area, while shear dominates in short building with a large base surface area (fig 5.1). The length of the Rutherford building is more than twice the height of the building and its width is about one fifth of its height. It therefore, has a large base surface area, so it is reasonable to assume that the shearing effect dominates.

Figure 5.2 shows the shearing effect of the floors of the Rutherford building. The floors are assumed to be incompressible and shearing occurs between them. The wall PR-1 is mounted on experiences shear which causes tilting of the ring. Tilt of the ring continually varies with the natural oscillation of the building. In other words it changes the local

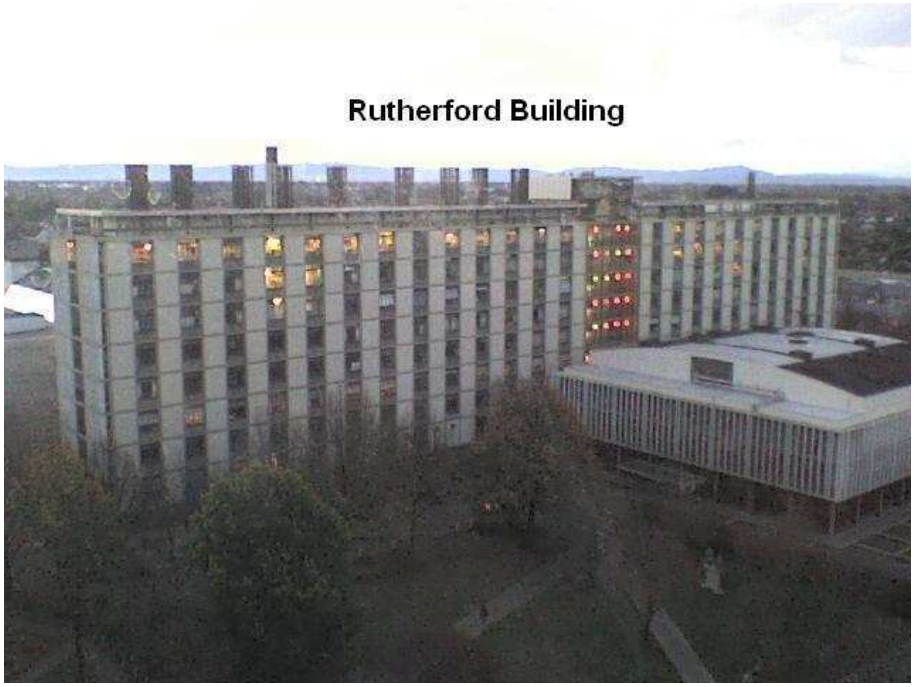

Figure 5.1: Rutherford building

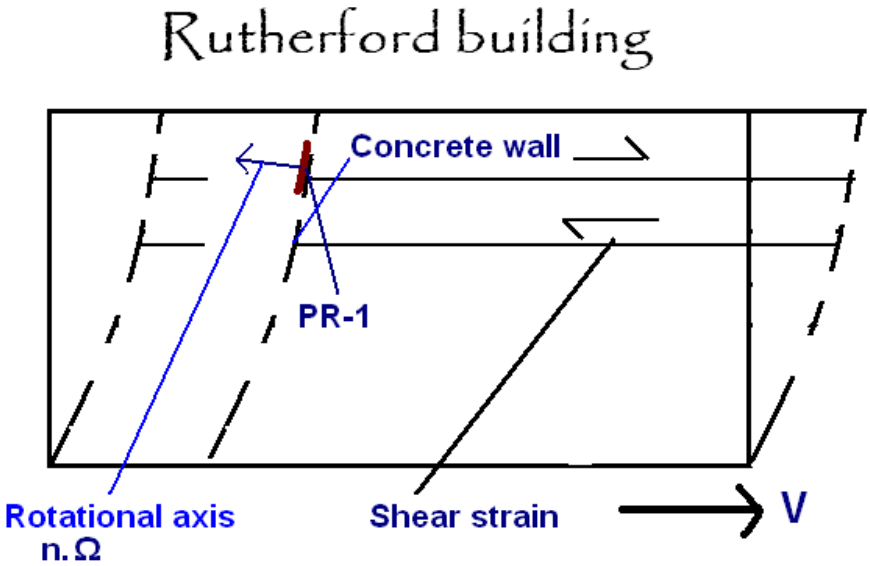

Figure 5.2: Shearing effect on the Rutherford building

normal ($\widehat{n}$) in equation 5.1

$$f_{sagnac} = \frac{4\widehat{A}}{\lambda P}\Omega\widehat{n} \tag{5.1}$$

where f_{sagnac} is Sagnac frequency, A is the area enclosed by the ring, λ is the wavelength of the laser, Ω the instantaneous angular velocity and $\widehat{n}$ is the local normal vector. The natural frequency of the building modulates the Sagnac frequency which can be seen as sidebands on figure 5.3. The sidebands are 2.4 Hz apart, corresponding to the first fundamental resonance mode, which are obtained from an SRS audio spectrum analyser. Figure 5.4 shows the same measurement done several years earlier with a building sensor. The value obtained from the sensor is 2.7 Hz. The small difference in frequency is expected as it is common for the building to drift in natural frequency due to diurnal temperature drift, wind, rain and also from microseisms [16]. Figure 5.5 shows the theoretically calculated mode shape for the shearing effect on the Rutherford building. Mode 1 shows the shape of the movement of the floors under natural oscillation in the wind for example.

The angular amplitude of the rotation induced by the tilt can be calculated using sideband analysis of the Fourier spectra. Stedman [52] (later modified by McLeod [36]) has calculated the modulation indices of the sideband S to be $\approx 2 \times 10^{\frac{-\alpha}{20}}$ where α is the difference in amplitude of the side band from the carrier earthline (caused by the rotation of the earth) in decibels. The modulation index in the equation below is used to calculate the angular amplitude:

$$\theta = \frac{S\lambda}{2P} \tag{5.2}$$

where θ is the angular amplitude, S the modulation index, λ the wavelength of the laser and P the perimeter. Using this expression, the angular amplitude is calculated to be 7.8 nrad for the natural oscillation of the building. It should be noted that this value is not the absolute angular amplitude (i.e. PR-1 is not rotated along the plane of the ring). The value is calculated so that it will give a quantitative way to compare the effects of earthquakes.

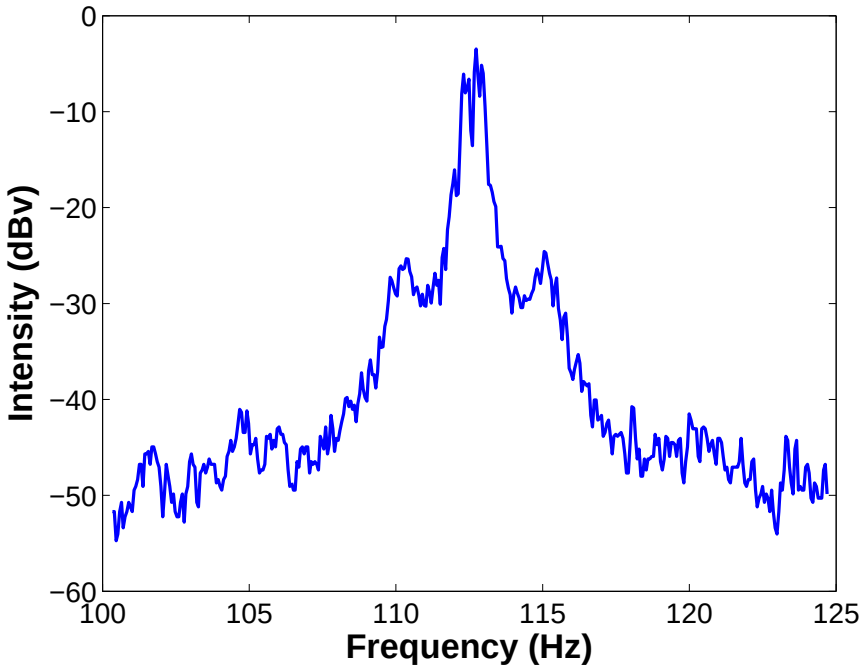

Figure 5.3: Fast Fourier spectrum of the Sagnac signal on a moderately windy day.

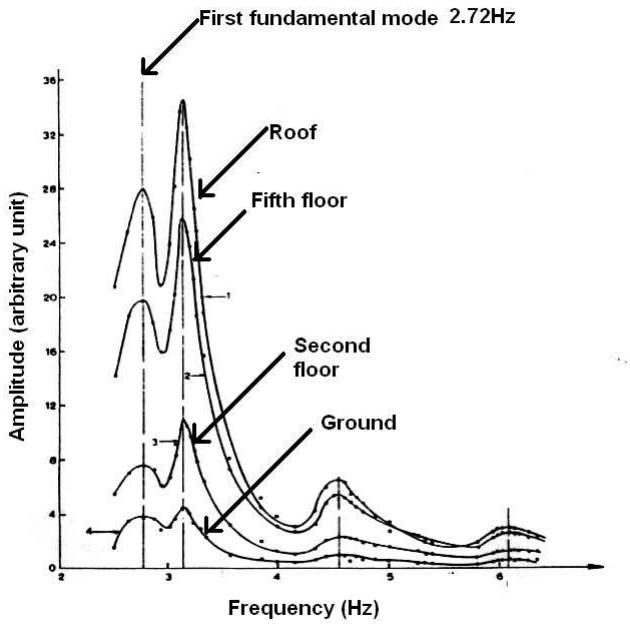

Figure 5.4: Normal modes of the Rutherford building as determined by triaxial sensors [41].

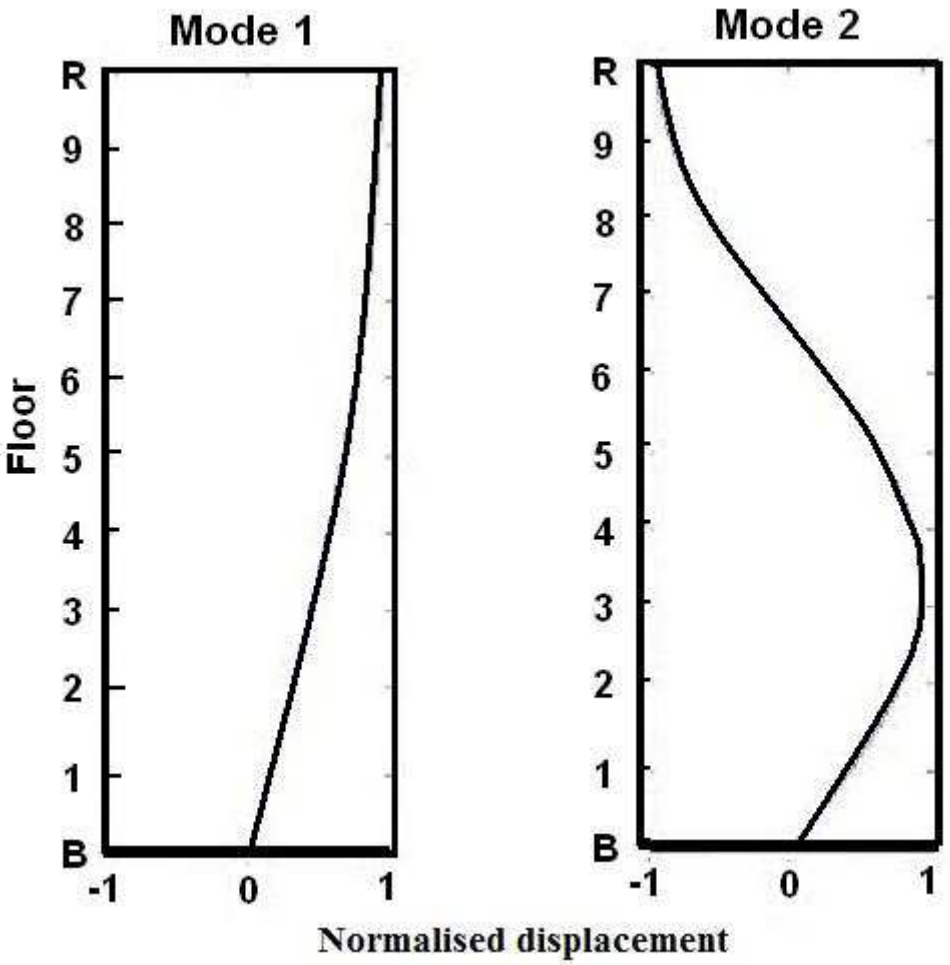

Figure 5.5: The fundamental mode oscillation of a typical building, which has similar dimensions as the Rutherford building [16].

5.2 Detection of Earthquakes

Large ring laser gyroscopes have been shown to be capable of detecting the horizontal and vertical components of teleseismic waves [39]. The coupling between the seismic waves and a ring laser has been studied in the past. However, all of the previous studies have utilised ring lasers that are attached to bedrock, and hence provide an insight into the behaviour of the earths crust. Usually a large ring laser, such as G-0, can pick up information from earthquakes. PR-1 is mounted in a building which tends to filter the response. This provides unique information on the building response. The four main types of seismic wave [3, 18, 35] which can affect the building response are summarised in table 5.1.

Wave type	**Properties**
Primary waves (P)	Compressional elastic body waves. The wave refracts through the intermediate crust. Travel faster than all other seismic waves. Induces longitudinal motion.
Shear waves (S)	Elastic shear body waves. Also called secondary waves. Can be horizontally (SH) or vertically (SV) polarised. Causes oscillation perpendicular to the direction of travel. Do not travel through fluids (i.e. molten rock, water, air.)
Love waves (L)	Horizontally polarised surface waves. Strongest amplitude is at the surface of the earth. Are dispersive and induce ripples in the ground in the horizontal plane.
Rayleigh (R)	Surface waves. Dispersive, causes displacement in the direction of propagation and in the transverse plane.

Table 5.1: Summary of the properties of different types of seismic waves.

When a seismic wave reaches the base of the building, oscillation occurs at one of the fundamental modes of the structure (fig 5.5). Since PR-1 is on the 7th floor, the effects are magnified. This can also be seen in figure 5.4 where the amplitude of the first

fundamental mode of oscillation increases as the floor level increases. This magnification is caused by the increase in displacement as the buildings height increases (fig 5.5). The time series for an earthquake recorded on the 1^{st} of February 2008 can be seen in figure 5.6. The first wave to arrive is the P-wave as it is the fastest seismic wave, as indicated by the initial increase in amplitude. PR-1 detected secondary waves 345 seconds after the primary wave. The secondary waves are S-waves. The Love (L) and Rayleigh (R) waves are the slowest and were not detected. This is possibly due to the fact the building is unable to respond to waves with such long wavelengths. The local geology and the dispersive characteristics of the surrounding medium may also have played a part.

The speed of P-waves in Banks Peninsula is 3330 ms^{-1} whilst for S-waves it is 1930 ms^{-1}. The exact propagation speed and the geology of the surface that the Rutherford building is based upon is not known, thus the Banks Peninsula values were used. It is possible to estimate the location (D) of the earthquake from the building response using the following equation:

$$D = \frac{\Delta t}{\Delta \varrho} \tag{5.3}$$

where $\Delta\varrho$ is the difference in slowness[1] of the S and P waves and Δt is the difference in arrival time [31]. This gives the location of the earthquake to be 1580 km from the building. A fast Fourier spectrum was taken during the earthquake and is shown in fig 5.7. This gives the frequency of the building during the earthquake to be 7.8 Hz and the angular rotation to be 41 nrad. This is significantly larger than that obtained previously. This indicates that the tilting effect is greater during the earthquake. For a typical building, the ratio for the frequency of mode 1 (seen left of figure 5.5) to mode 2 (seen right of figure 5.5) is obtained from instrumented structures[2] to be between 3 and 3.5 [16]. The ratio obtained during the earthquake is 3.2 (7.8 Hz/2.7 Hz), hence the Rutherford building was oscillating at the second fundamental mode during the earthquake.

[1]Geophysical term meaning reciprocal of wavespeed

[2] Buildings which have measured mode structures during an earthquake.

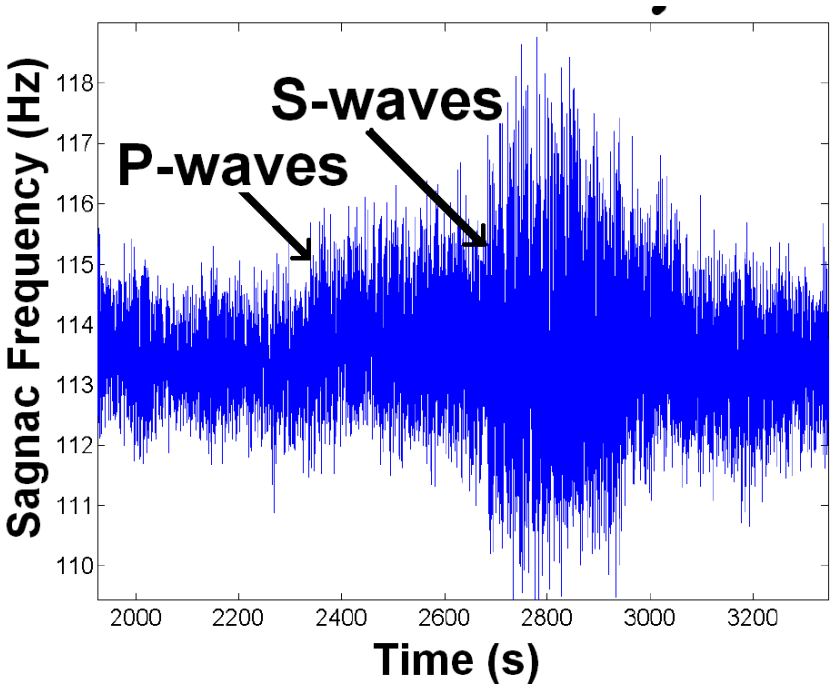

Figure 5.6: PR-1 time series during an earthquake recorded on 1^{st} of February 2008.

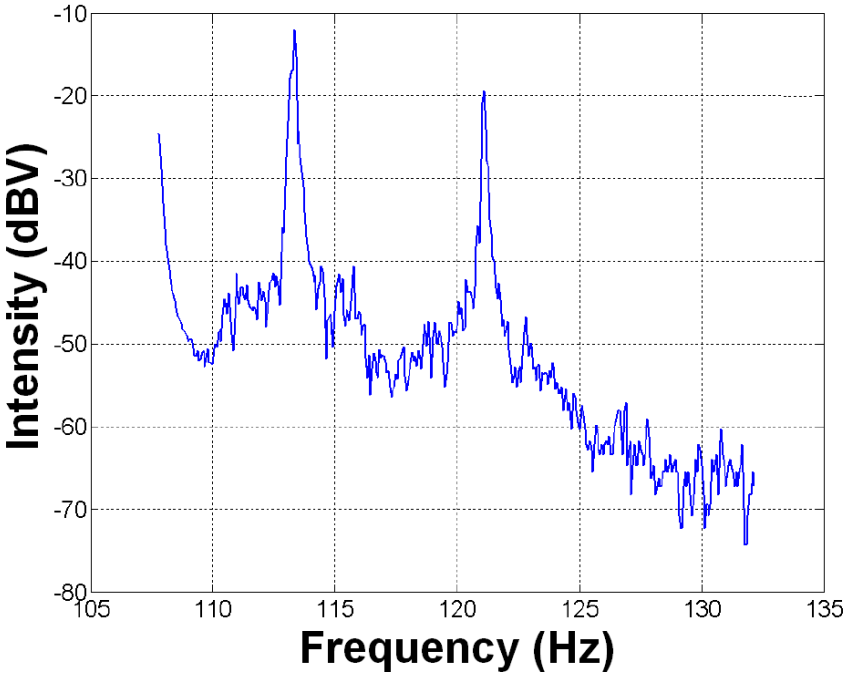

Figure 5.7: Fast Fourier spectrum measured using an SRS spectrum analyser during an earthquake.

Chapter 6

Testing Supermirrors via the Ringdown and Allan Variance Methods

Supermirrors with extremely high reflectivity play a large part in the performance of ring lasers by reducing laser backscattered light which leads to coupling of the clockwise and counterclockwise intra-cavity beams [13]. Even when the ring laser is not frequency degenerate (unlocked) they reduce frequency pulling compared to a conventional laser mirror. Though the large ring lasers don't have the problem of lock-in due to their shear size, they do experience random walk in frequency, the magnitude of which is proportional to the total scattered loss of the mirrors [47]. In this chapter the performance of a range of supermirrors will be analysed using ringdown measurements and the Allan variance obtained from their operation in the G-0 ring laser.

6.1 Mirror Construction

The supermirrors are dielectric mirrors composed of alternating layers of materials with high and low refractive indexes. The films are $\lambda/4$ thick and are stacked on a low expansion material such as Zerodur. The material used in the ring laser mirrors has alternating layers of TiO_2 causing a high refractive index and SiO_2 causing a low refractive index [55]. The reflectivity of these mirrors is 99.99997% and is limited by imperfections in the surface shape, roughness, loss of amplitude of the electric field upon reflection and anisotropy in birefringence [55]. The theoretical limit of the scattering losses calculated by Bilger

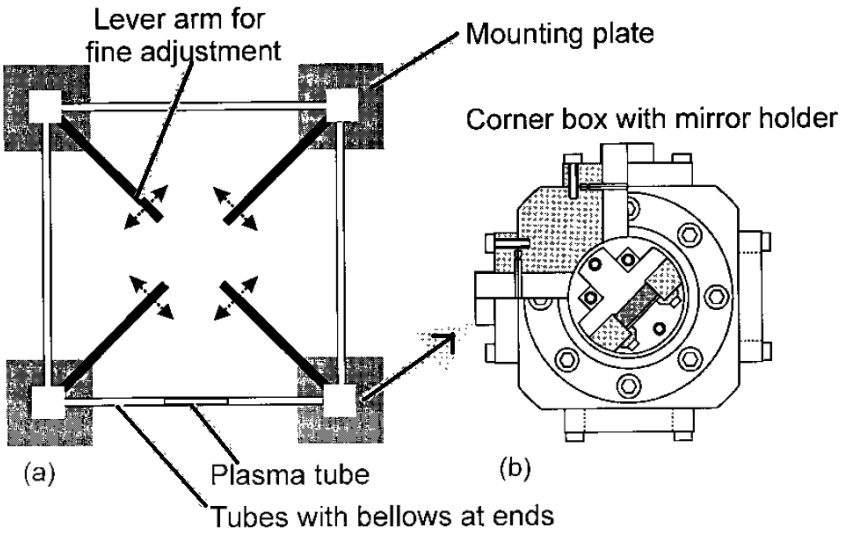

Figure 6.1: Overall schematic of (a) G-0 layout and (b) corner box detail [42]

was 1 ppb [14] for these materials has yet to be reached. All the mirrors are supplied by Research Electro-Optics, Inc(REO). Fully automated ion beam sputtering thin film (IBS) deposition is used in the mirror construction [4]. Unfortunately, the exact manufacturing process and the precise material details are not known due to commercial and military sensitivities.

6.2 Experimental Setup

The super mirrors were originally made for the Gross Ring Laser (G), a 4 m $\times$ 4 m ring laser made from Zerodur[1] and located at the Geodetic Observatory Wettzell in Bavaria, Germany [5]. Unfortunately the supermirrors are not easily interchangeable in G due to its design. The G-0 ring laser at Cashmere has similar dimensions to the the G-ring at 3.5 m $\times$ 3.5 m [42]. It is mounted vertically on a concrete wall in the Cashmere cavern. Mounting plates are attached to each side of G-0 to reduce beam movements caused by environmental change (fig 6.1(a)). Four corner boxes (fig 6.1(b)) are mounted on the side plates and are connected by stainless steel tubing. The G-0 construction enables easy access to the super mirrors and its location provides superb environmental stability. For this reason G-0 is chosen for this experiment. Four sets of mirror configurations were used in the experiment. Two of the sets contained ultra low expansion (ULE) titanium silicate

[1]Extremely low expansion glass ceramic

Mirror set	**Type of Supermirrors**
SM1	Four $\sim$ 1 year old supermirrors with radius of curvature of 4 m. The transmission of each mirror is 0.2 ppm. Zerodur substrate.
SM2	Four $\sim$ 1 year old supermirrors with radius of curvature of 4 m. Two of the mirrors have a transmission of 0.2 ppm. The other two mirrors have an extra coating on the surface which increases their transmission to 2 ppm. Zerodur substrate.
SM3	Four $\sim$ 10 year old supermirrors with radius of curvature of 21 m. The transmission expected to be 6 ppm. ULE substrate.
SM4	Four $\sim$ 10 year old supermirrors with radius of curvature of 4 m. The transmission is expected to be 6 ppm. ULE substrate.

Table 6.1: The supermirror sets used in the experiments.

glass as a substrate for the IBS coating. These were around 10 years old. A newer mirror set ($\sim$ 12 months old) uses a Zerodur substrate [6]. The mirror sets are summarised in table 6.1.

To perform mirror changes, a gas pumping system similar to that used in PR-1 (fig 4.8) is employed, using a diaphragm pump. A liquid nitrogen dewar was connected to the pumping system and was heated to provide nitrogen gas, which was added to atmospheric pressure to prevent air rushing into the cavity. This was done to prevent pitting and contamination of the surface of the mirrors. Once the cavity was at atmospheric pressure the eight bolts of the corner boxes were removed (fig 6.1(b)) and then the supermirrors were removed and placed in a sealed container. The new mirror set could then be placed. Two green 543.5 nm ($3s_2 \rightarrow 2p_{10}$) He-Ne lasers are injected in opposite directions around the cavity. The supermirrors transmit 50% of the green light. The beams were guided through the cavity until the clockwise and counter-clock wise beams overlapped. Then the gain tube was adjusted to ensure it did not obstruct the path of the beams. A power meter was used to measure the power of the clockwise beam. The laser was run at different power levels to ensure that the changes in the stability of the laser were due to the mirrors rather than different power levels. Natural neon was used for most of the experiment. For one set of mirrors a 50% ^{20}Ne, 50% ^{22}Ne ratio was also tried to ensure that the isotope mixture did not play a large role in the measured performance of the laser.

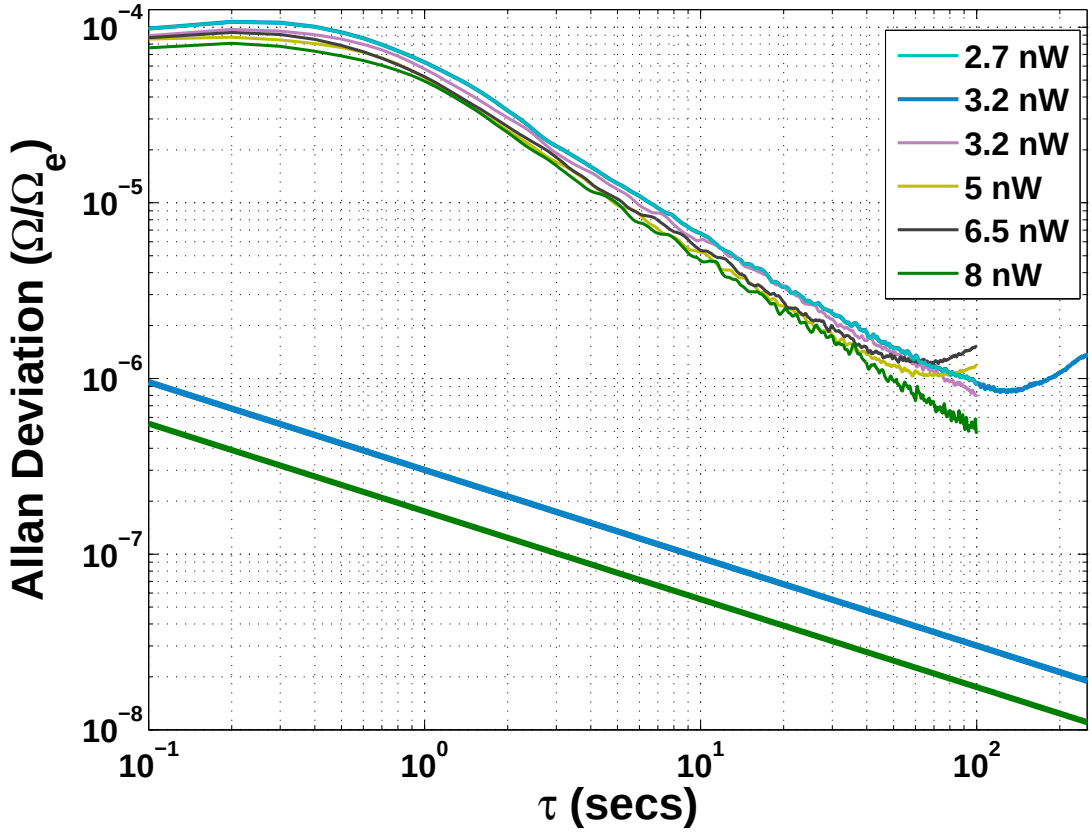

Figure 6.2: Allan variance plot for SM1 mirror set. The Allan variance is normalised with earth's rotation (Ω_e)

6.3 Results

All the Allan variance plots were normalised to the theoretical value of the Sagnac frequency for G-0 of 287.25 Hz [30]. From the graphs (fig 6.2, 6.3, 6.4 and 6.5), the measured gradient for the four sets of mirrors has a constant value of -0.9 for very short measurement times of 1 to 10 seconds. The gradient corresponds to an α value of 1 and 2 (table 2.1), hence flicker phase modulation and white phase modulation are the dominant noise processes at these integration times. It is not surprising that this is the case since this type of noise is associated with electronics such as the transimpedence amplifiers used on the photomultiplier and the analog to digital converter in the labview card. Since the same amplifier and labview card is used for all the experiments, the gradient remains constant.

The slope of the Allan variance plot changes for all but the mirrors are set at SM1, showing that they are the best mirror for 10 to 100 second measurement times. For the

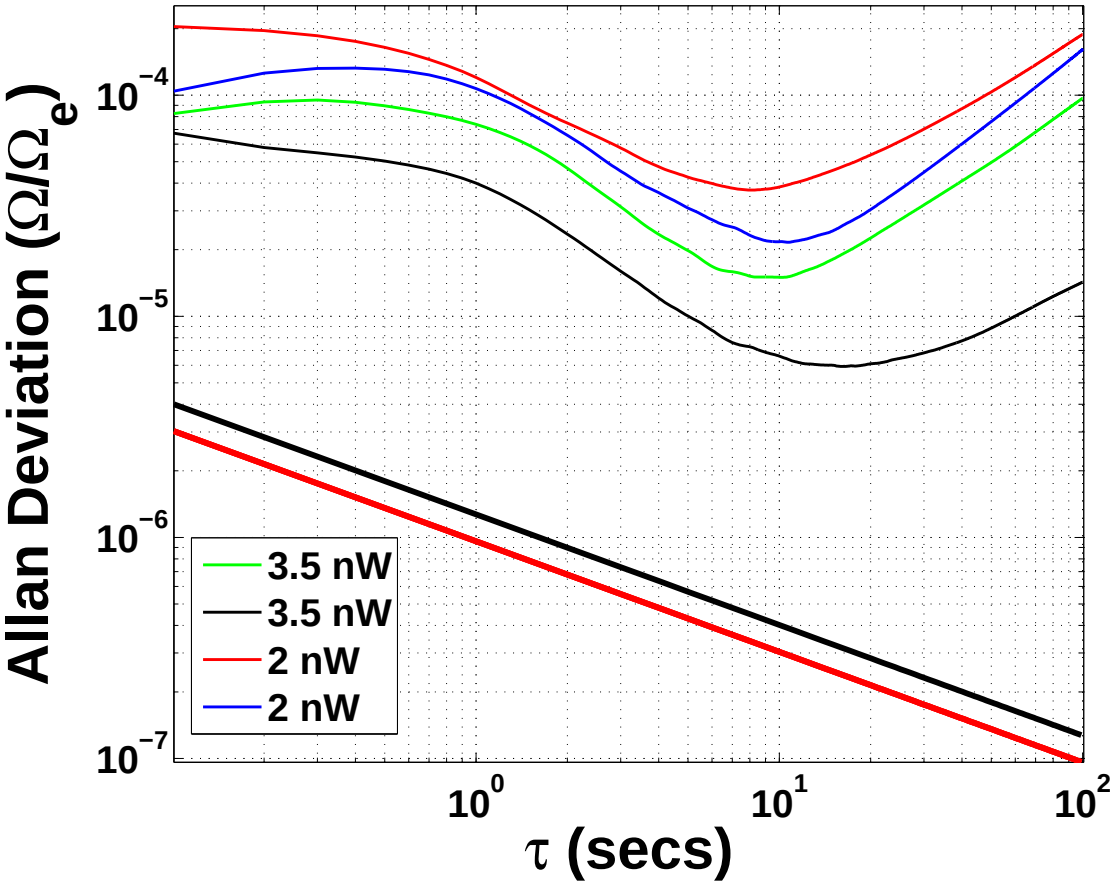

Figure 6.3: Allan variance plot for SM2 mirror set. The plots are scattered due varying stability.

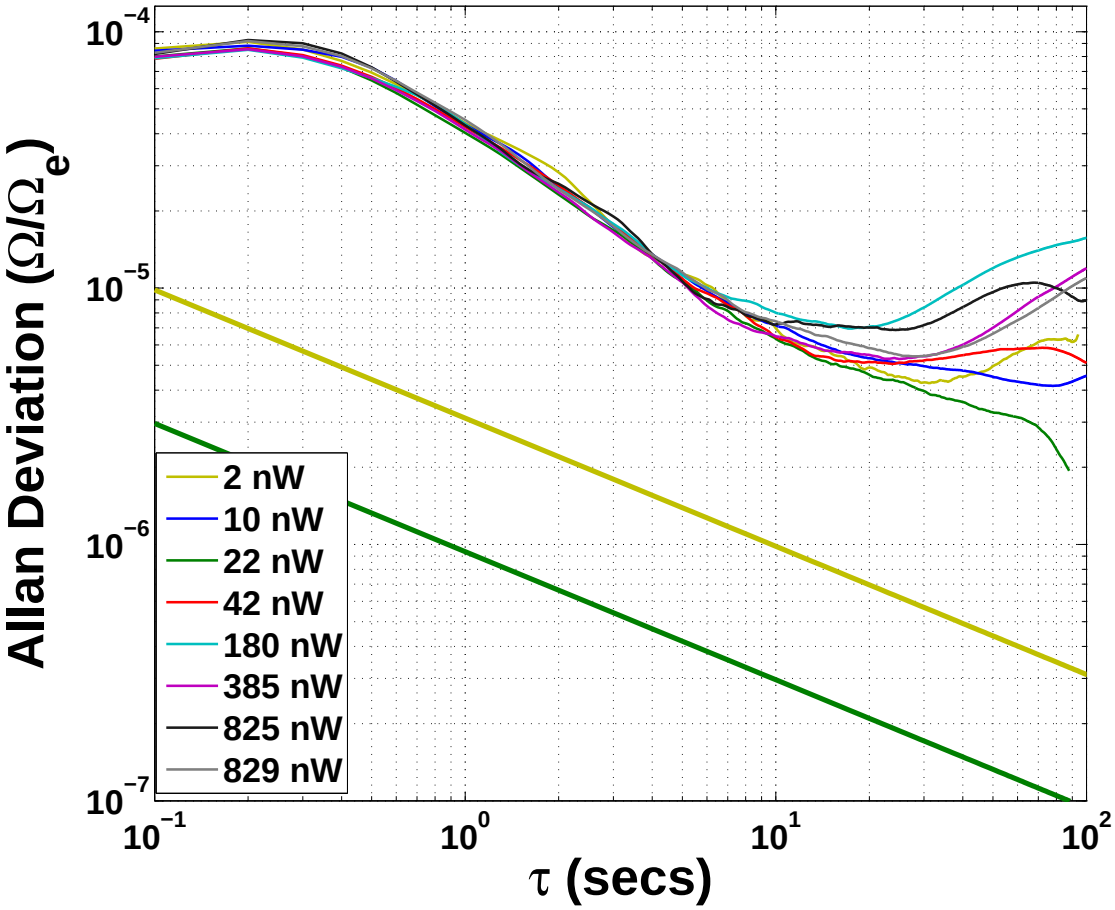

Figure 6.4: Allan variance plot for SM3 mirror sets. After integration time of 10 seconds, the Allan plot scatters due to beam steering effects.

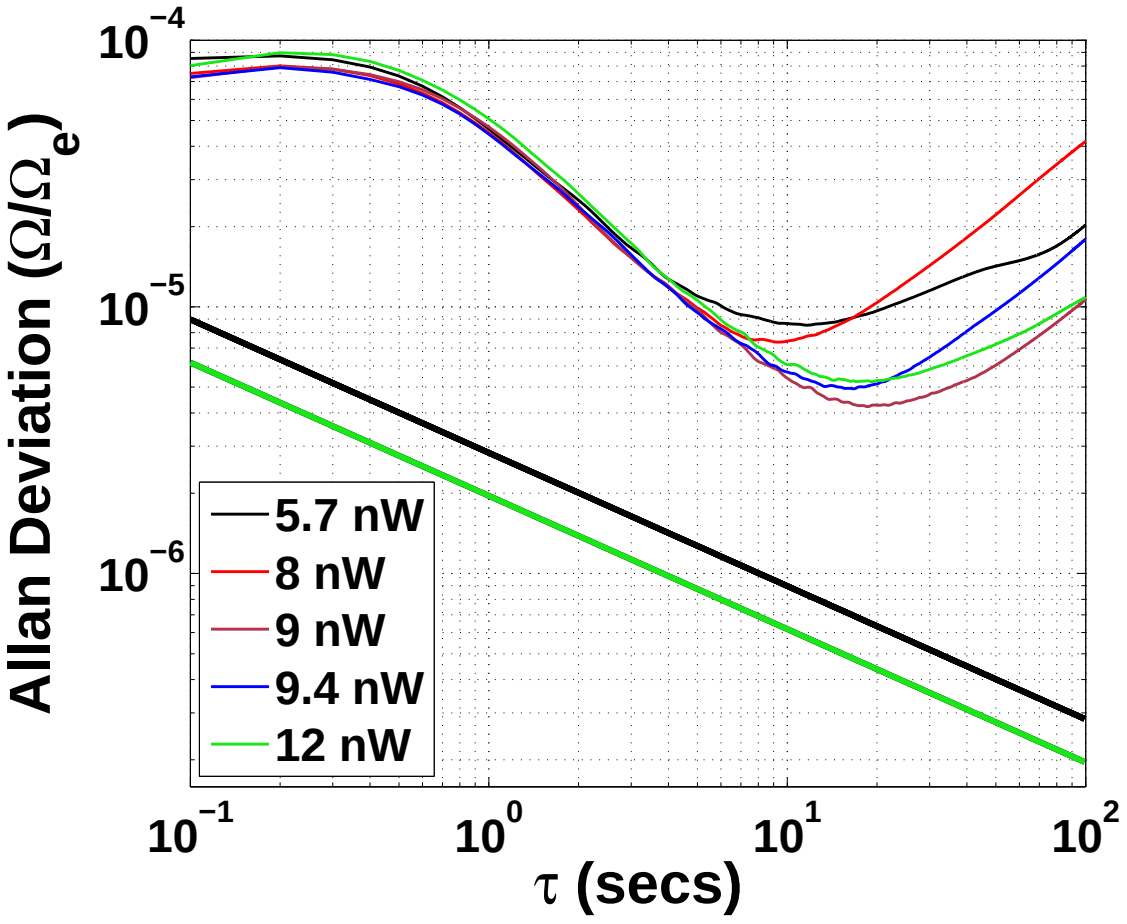

Figure 6.5: Allan variance plot for SM4 mirror sets.

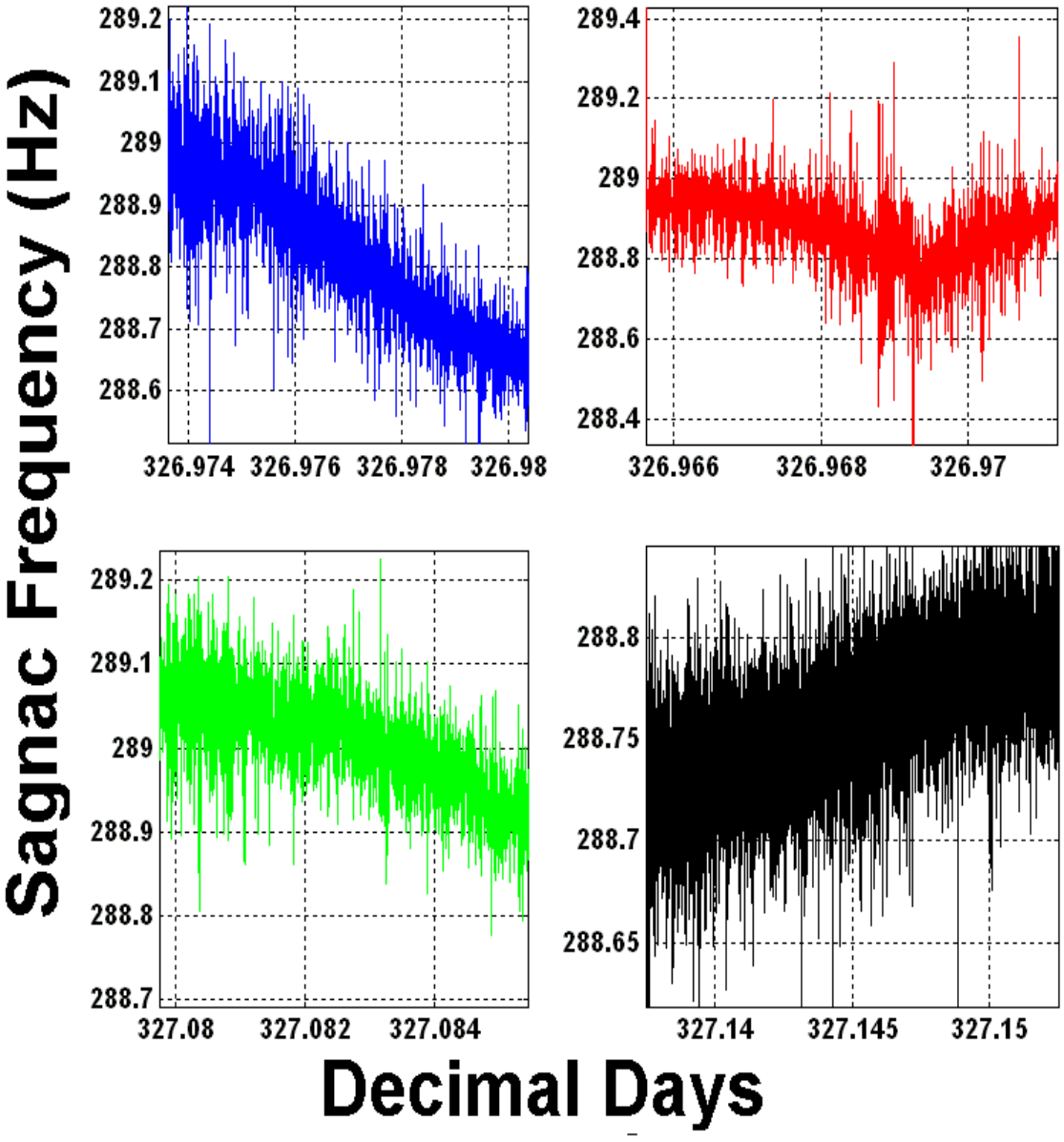

Figure 6.6: The Sagnac frequency for SM2 mirror set. The plot coloured black gives the best stability. All the other plots have varying drifts. The red plot yields the worst stability due to a glitch in the data.

SM4 mirror set the slope varies from 0.5 to 0.8 (fig 6.5), and for SM2 mirror it varies from 0.6 to 0.8 (fig 6.3). The values close to 0.5 are due to random walk noise caused by the random shift in Sagnac frequency and is usually related to the environmental factors, such as mechanical shock, vibration and temperature change. The gradient for the SM3 set varies widely from -0.2 to 0.8 (fig 6.4). These variations could be due to the fact that these mirrors have a different radius of curvature and are more suspectable to beam steering effects.

6.4 Beam Steering Analysis

The beam steering analysis was performed by Dr. Bob Hurst of the University of Canterbury, using a ray matrix approach. The mirrors of G-0 can be rotated and/or tilted by vibration, micro-seismics, temperature and pressure changes, thereby steering the beam on the surface of mirrors.

Different cavity parameters, such as mirror ROC, will have different sensitivity to these effects. The table below shows a hypothetical scenario where one of the mirrors(1)[2] is rotated clockwise about 10 μrad and when the mirror(1) is tilted outward by 10 μrad. The value of 10 μrad was chosen arbitrarily. For example, if the mirror was moved by 1 μrad all the values in the table 6.2 would be 10 times lower. The negative sign for the rotation value in table 6.2 corresponds to downward movement of the beam. The negative sign for tilt corresponds to downwards movement of the beam. All of the measurements are relative to the plane of the laser. The table shows that tilting the 21 m mirrors causes considerably large movements than the 4 m mirror configuration. Rotation affects the 4 m mirror configuration more than the 21 m. Environmental changes could favour tilt motion in G-0, and could explain the large variation in slopes on the 21 m mirrors seen in the Allan variance plots (fig 6.4).

6.5 Ring Down Measurements

The cavity (photon lifetime) ringdown measurements were performed in the same manner as previously. The figures 6.7, 6.8, 6.9 and 6.10 show the result from the ring down measurements. The ring down times are much larger for the SM1 and SM2 mirror sets since Zerodur can be polished much more smoothly than ULE [40] and the new mirrors are

[2]arbitrary mirror location, i.e. each mirror around the ring is labeled M(1)to M(4)

Mirror	**ROC 21 m Rotation**	**ROC 4 m Rotation**
1	-9	-69
2	42	19
3	-55	78
4	42	19
Mirror	**ROC 21 m Tilt**	**ROC 4 m Tilt**
1	25	-19
2	39	10
3	45	27
4	39	10

Table 6.2: The movement of the beam (μrad) induced by small perturbations in the mirror.

Mirror	**Ring Down Time (μs)**	**Standard Deviation (μs)**	**Quality Factor (Q)**
SM4	56.5	1.9	1.69×10^{11}
SM3	87.0	3.3	2.59×10^{11}
SM2	213	2.2	6.34×10^{11}
SM1	773	2.2	2.30×10^{12}

Table 6.3: The ring down time and standard deviation for various mirror sets

new and hence have better reflectivity. It is worth noting, however, that the SM2 mirror set has an extra coating to spoil the reflectivity and therefore increase the transmission. The SM3 mirrors have the longest ring down time for the older sets of mirrors and the highest standard deviation (table 6.3). It is not known why the SM2 mirror configuration produced such large shifts in the Allan plots (fig 6.3). From figure 6.6 it is clear that the shifts were due to drifts and jumps in the Sagnac frequency. Two of the mirrors in the SM2 mirror set has an extra coating, which decreases the finesse to increase transmission. Having higher transmission causes a better signal on the photomultiplier tubes, but from the Allan plots it is clear that finesse is the most important factor in terms of performance. There is no clear relationship between power and stability, as indicated by the scattered distribution of Allan variance plots (fig 6.2,6.3,6.4 and 6.5).

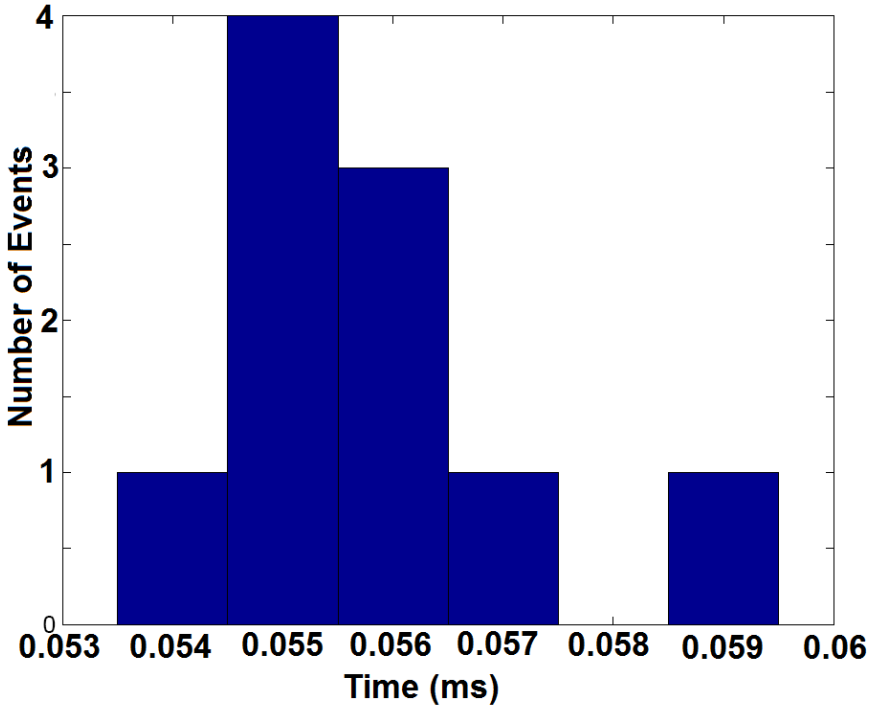

Figure 6.7: The distribution of measured ringdown times for mirror set SM4

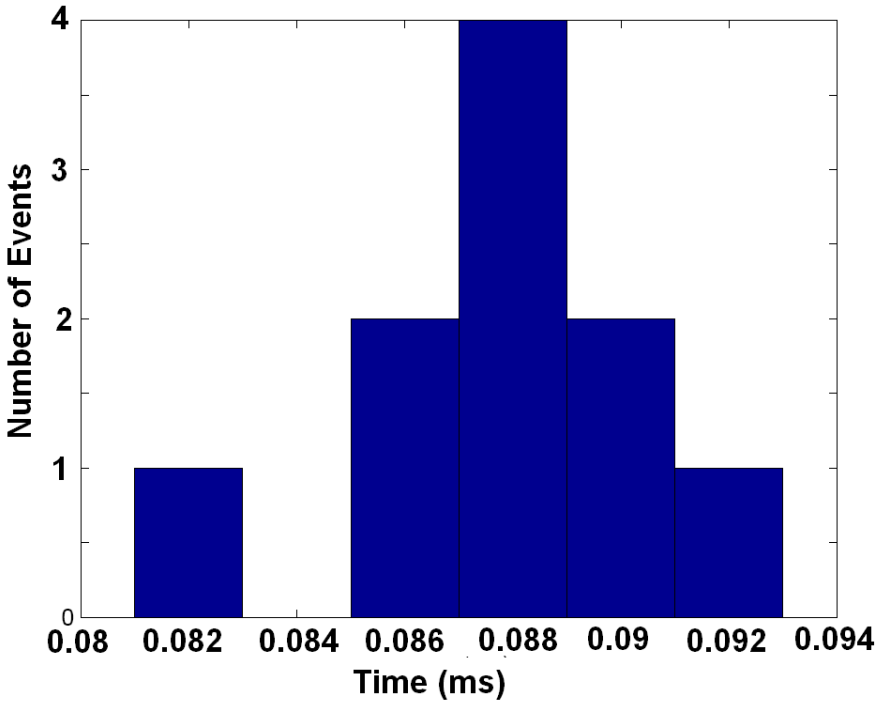

Figure 6.8: The distribution of measured ringdown times for mirror set SM3

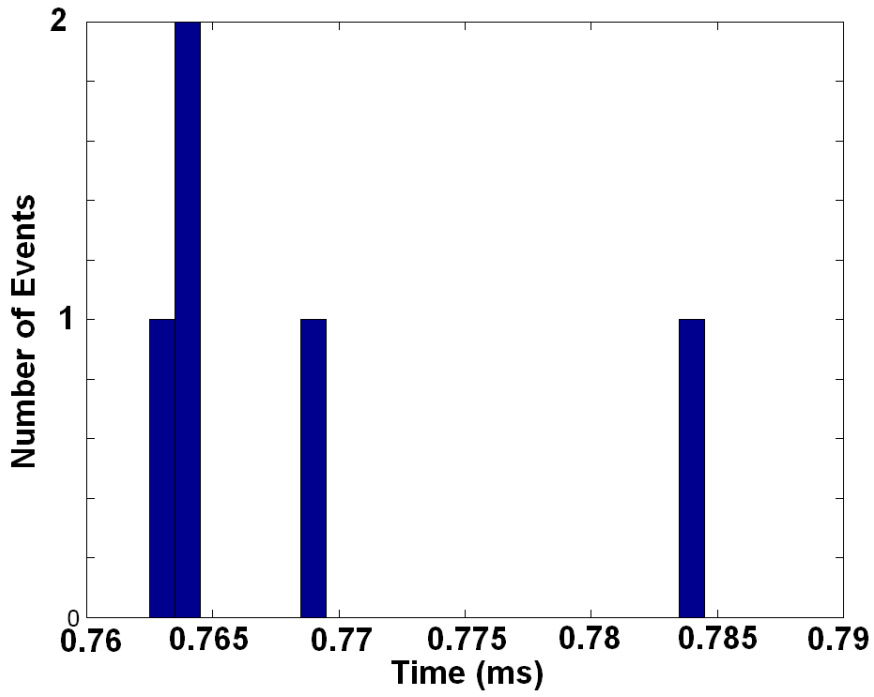

Figure 6.9: The distribution of measured ringdown times for mirror set SM1

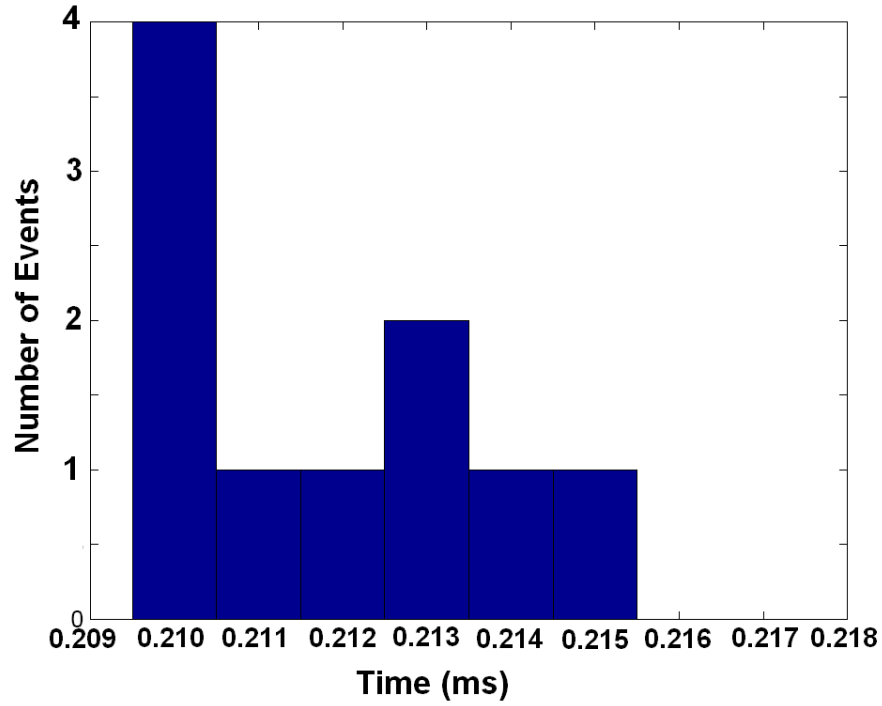

Figure 6.10: The distribution of measured ringdown times for mirror set SM2

6.6 Quantum Noise Limits

The noise caused by spontaneous emission, is the ultimate limit in detecting techniques for the laser linewidths. The irreducible quantum limit is given by the equation [45]:

$$\delta\Omega = \frac{cP}{4AQ}\sqrt{\frac{hf}{P_x t}} \tag{6.1}$$

where Q is the quality factor, c is the speed of light, A is the area enclosed by the beams. h is Plank's constant, P_x is power loss per mode and t is the time of integration. We also use the Q values in table 6.3, and assume an arbitrary total beam power loss per mode of 40 nW. As Q increases the Allan plot shifts downwards showing increased sensitivity to rotation (fig 6.11).

The power loss (P_x) in the cavity is mainly caused by the absorption by mirror substrate, scattering on the mirror surface and transmission through the mirror. The fractional losses for typical supermirrors is measured to be 4.8×10^{-5} for scattering, 1×10^{-6} for absorption and 3×10^{-7} for transmission [22]. From the measured output power and the fractional losses given above, it is possible to estimate the total power loss (P_x) for the various mirror sets.

Using the power loss (P_x) the quantum limit is calculated for the Allan plots shown in this chapter. Each of the plots contain two lines: one for the highest transmission output measured and other for the lowest. As the power loss increases the quantum limit decreases. The mirror sets SM3 and SM4 have quantum limits which are closer to the experimental data than SM1 and SM2 due to their lower finesse.

The Allan variance plots (fig 6.3,6.4 and 6.5) tend towards the quantum limit with an integration time of $\sim$10 seconds, then they diverge away for the higher integration times. In contrast, mirror set SM1 (fig 6.2) keeps heading towards the quantum limit until $\sim$100 seconds, showing that the SM1 mirror set is the best. From equation 6.1 it is clear that to improve the resolution of the instrument, the transmission and quality factor of the mirrors should be increased. However, the transmission and quality factor are related in such a way that having higher transmission will cause a decrease in quality factor, as shown by SM2 mirror set.

In figure 6.4 the quantum limit for transmission of 2 nW and 22 nW are calculated. All the other transmission values are very high for single mode operation. When this experiment was conducted FP was not available to identify multimode operation.

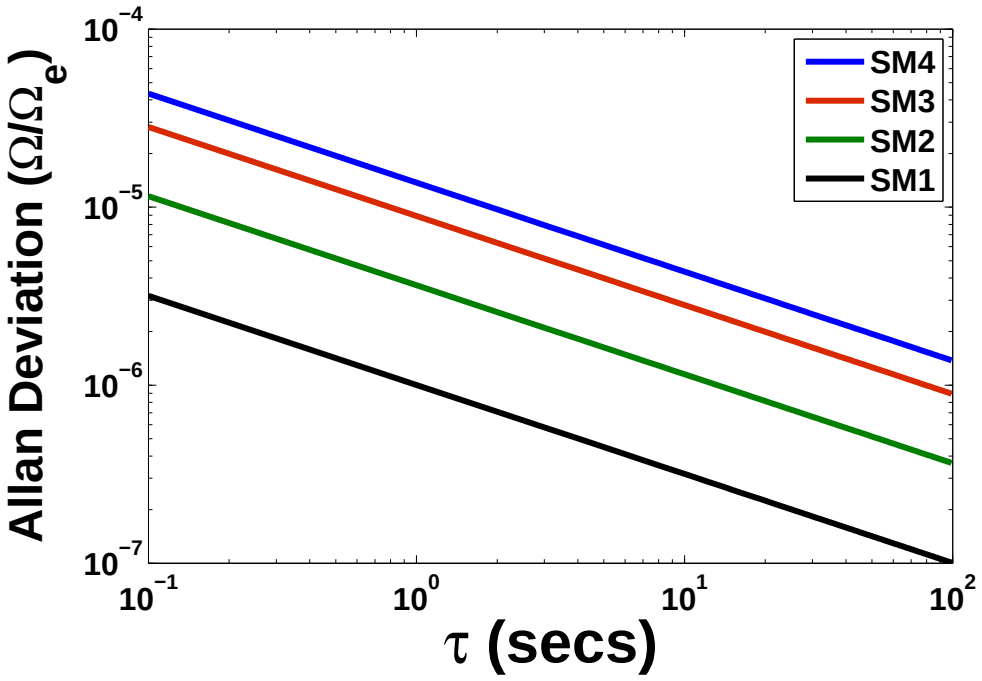

Figure 6.11: The quantum noise limits for various mirror sets

Chapter 7

Conclusion

7.1 Summary of Results

This thesis presents a systematic study of the PR-1 ring laser from the perspective of optimising its values as a sensor of seismically induced rotations. The laser was initially realigned after many years of lying idle. After cleaning the supermirrors, a cavity Q of 2.9×10^{11} was obtained. A peak sensitivity to rotation of around 10^{-3} of the earth's rotation rate was experimentally obtained, with a 10 second time constant. However, the gyroscope is ultimately limited by geometrical instabilities, which give rise to longitudinal mode hops and operation of the counter-propagating beams on different longitudinal modes.

A detailed study of the threshold for operation on more than a single longitudinal mode (the multi-mode threshold) was performed as a function of the helium pressure for both a 50:50 neon isotope mixture as well as for a natural neon mix. This was successfully modeled using the total atomic susceptibility to calculate a relative gain profiles for a Voight lineshape approximation to the gain curve. The derived saturation intensities increase with increasing pressure. The 50:50 neon mixture has a higher saturation intensity than natural neon. This feature can be successfully accounted for. A key feature of higher pressure operation is that the multi-mode threshold is high and thus the laser can be run at a higher output power (and therefore higher detectable light levels) whilst still maintaining single mode operation. The downside of this operation regime is that mode competition increases due to the increasing overlap of the spectral holes burnt into the gain curve. Notably for 50:50 neon the maximum frequency separation of holes is obtained and therefore the mode competition will be much lower than for natural neon.

This appears to be reflected in the Allan variance plots. The gain curve calculations also predicted that there is more gain available in the wings of the gain curve for higher power. This promotes multi-mode operation and was proven be the case.

It was possible to demonstrate stable amplitude multi-mode patterns (and concomitant Sagnac waveforms) at very high powers above the threshold. This is an indication of mode-locking although the laser does not exhibit pulsing this is known as FM mode locking. Running PR-1 in this regime may yield considerable advantages for long time operation since it can eliminate the mode-hops which plague the device during single mode operation. Differing mode patterns yield different Sagnac contrast.

PR-1 was able to monitor the fundamental resonance mode of the Rutherford building to 2.7 Hz. During an earthquake on the 1^{st} of February 2008, PR-1 was able to pick up S and P waves which gave the estimated distance from the earthquake to be 1580 km. During the earthquake the frequency of the building motion was 7.8 Hz and therefore the building was oscillating at its second fundamental frequency.

The stability of the supermirror sets is also investigated showing that the best mirror set is the one with the highest quality factor. This mirror set also tends towards the quantum limit for higher integration time than the other mirror set. This was followed by SM2 mirror set which has the second highest quality factor. However, the stability of these sets tends to vary, which may have to do with the extra coating on the mirror surface which increases transmission. The older mirror sets performed the worst due to their age and use of ULE as a substrate. The newer mirror sets used Zerodur which is superior to ULE. The 21 m is the best old set of mirror but it is more susceptible to environmental fluctuation as shown by the fluctuation in the the Allan plots after an integration time of $\sim$10 seconds.

The performance of a range of supermirrors has been investigated using the Allan variance and cavity photon lifetime methods. The mirrors employed for this study were the most comprehensive set available and range from very new mirrors coated using state-of-the-art technology, to mirrors that have seen a decade of service. Ultimately, and perhaps unsurprisingly, the mirror set with the highest finesse performs the best. One of the principal difficulties lies in knowing the precise losses at the surfaces of each mirror, that is, the transmission, scattering and absorption losses. The geometric stability of the cavity did not seem to play a strong role.

7.2 Acknowledgements

I would like to thank Dr. Jon-Paul for his supervision, tolerance and advice and Dr. Bob Hurst for his support and technical assistance. I am grateful to my grandmother and family for their support over the years. In particular I would like to thank Jen Dubois for proof reading this thesis and generally making me get moving.

Special thanks go to following staff and students:

Mr. Robert Thirkettle for technical help specially with alignment of the ring lasers

Mr. Richard Graham for programming and computer related help.

Prof. Ulli Schreiber for providing supermirrors and some experimental data.

Mr. Clive Rowe for his help with experimental work, especially for his servo system.

Mr. Graeme MacDonald and Mr. Ross Ritchie for electronic support.

Mr. Peter Hume for general discussion.

Bibliography

[1] R3896 PMT Technical Data Sheet, Hamamatsu Photonics, 2006.

[2] http://en.wikipedia.org/wiki/Neon.

[3] http://web.ics.purdue.edu/ braile/edumod/waves/WaveDemo.htm.

[4] http://www.reoinc.com/pdf/Laser Components.pdf.

[5] http://www.ringlaser.org.nz.

[6] http://www.pgo-online.com/intl/service/index.html.

[7] D.W. Allan. Time and frequency (time-domain) characterisation, estimation, and prediction of precision clocks and oscillators. *IEEE Journal of Quantum Electronics*, 6:647–650, 1987.

[8] D.W. Allan, N. Ashby, and C.C. Hodge. The science of timekeeping applications note 1289.

[9] D.W. Allan and J.A. Barnes. A Modified Allan Variance with Increased Oscillator Characterization Ability. Proceeding 35th annual frequency control symposium. 1981.

[10] E.O. Ammann, B.J. McMurtry, and M.K. Oshman. Detailed experiments on Helium-Neon FM lasers. *IEEE Journal of Quantum Electronics*, 6:263–272, 1965.

[11] T.D. Anh and W. Dietel. Homogeneous broadening in a 0.63 μm single mode He-Ne lasers. *Opto electronics*, 5:243–248, 1973.

[12] F. Aronowitz. Theory of a travelling-wave optical maser. *Physical Review*, 139:635–646, 1965.

[13] F. Aronowitz. *The Laser Gyro in Laser Applications.* Acedemic Press, 1971.

[14] H.R. Bilger, P.V. Wells, and G.E. Stedman. Origins of fundamental limits for reflection losses at multilayer dielectric mirrors. *Applied Optics*, 33:7390–7396, 1994.

[15] W.W. Chow, J.B. Hambenne, T.J. Hutching, V.E. Sanders, M. Sargent, and M.O. Scully. Multioscillator laser gyro. *IEEE Journal of Quantum Electronics*, 16:918–936, 1980.

[16] J. Clinton. *Engineering Seismology.* Unpublished lecture notes.

[17] L.S. Cutler and C.L. Searle. Some aspects of the theory and measurement of frequency fluctuations in frequency standards. *IEEE Journal of Quantum Electronics*, 54:136–154, 1966.

[18] D. Duff. *Holmes Principles of Physical Geology.* Chapman and Hall, 1994.

[19] R.W. Dunn. Multimode ring laser lock-in. *Applied Optics*, 28:2584–2587, 1989.

[20] R.W. Dunn. Design of a triangular active ring laser 13m on a side. *Optical Society of America*, 37:6405–6409, 1998.

[21] R.W. Dunn, D.E. Shabalin, R.J. Thirkettle, G.J. MacDonald, G.E. Stedman, and K.U. Schreiber. Design and initial operation of a 367-m 2 rectangular ring laser. *Applied Optics*, 41:1685–1688, 2002.

[22] R. Graham. *Investigation and control of the effects of backscatter in large ring lasers.* Undergraduate Project, 2004.

[23] R. Graham. *Experiment to Characterise the Distribution of Excited States in a Helium-Neon Plasma Discharge.* Undergraduate Project, 2005.

[24] R. Graham. *Ring Laser Gain Medium.* M.Sc. thesis, 2006.

[25] N. Harris. *Modern Vacuum Practice.* McGraw Hill Book Company, 1989.

[26] D.A. Howe, D.W. Allan, J.A. Properties of signal sources Barnes, and measurement method. Proceeding of 35th annual frequency contral symposium. 1981.

[27] R.B. Hurst, R.W. Dunn, K.U. Schreiber, R.J. Thirkettle, and G.K. MacDonald. Mode behaviour in ultralarge ring lasers. *Applied Optics*, 43:2337–2346, 2004.

[28] R.B. Hurst, J-P.R. Wells, and G.E. Stedman. An elementary proof of the geometrical dependence of the Sagnac effect. *Journal of Optics*, 9:838–841, 2007.

[29] S.F Jacobs and R. Zanoni. Laser ring gyro of arbitrary shape and rotation axis. *American Journal of Physics*, 50:659–660, 1982.

[30] B.T. King. *Ring Laser Dynamics*. PhD thesis, University of Canterbury, 1999.

[31] S.L. Kramer. *Geotechnical Earthquake Engineering*. Prentice Hall, 1996.

[32] Z. Li. *Optical Supercavity and Precision Ring Laser Measurement*. PhD thesis, University of Canterbury, 1993.

[33] D.R. Linde. *CRC Handbook of Chemistry and Physics*. CRC Press inc, 1990.

[34] W.M. Macek and D.T.M. Davies. Rotation sensing with travelling wave ring lasers. *Applied Physics Letters*, 2:67, 1963.

[35] S. Marshak. *Earth: Portrait of a planet*. W.W Norton and Company.Inc, 2005.

[36] D. McLeod. *Seismic effects in ring lasers and transverse mode selection in he ne lasers*. PhD thesis, University of Canterbury, 1999.

[37] A.A. Michelson, H.G. Gale, and F. Pearson. The effect of the earth's rotation on the velocity of light. *Journal of Astrophysics*, 61:137, 1925.

[38] S.E. Harris. Theory of FM Laser Oscillation. *IEEE Journal of Quantum Electronics*, 6:245–262, 1965.

[39] A. Pancha, T.H. Webb, G.E. Stedman, D.P. McLeod, and K.U. Schreiber. Ring laser detection of rotations from teleseismic waves. *Geophysical Research Letters*, 27:3553–3556, 2000.

[40] Personal communication with K.U. Schreiber. 2008.

[41] Personal communication with R.B. Hurst. 2008.

[42] C.H. Rowe, U.K. Schreiber, S.J. Cooper, B.T. King, M. Poulton, and G.E. Stedman. Design and operation of very large ring laser gyroscope. *Applied Optics*, 38:2516–2523, 1999.

[43] G. Sagnac. *Comptes Rendus*, 157:708–710, 1913.

[44] K.U. Schreiber, T. Klugel, A. Velikoseltsev, W. Schluter, G.E. Stedman, and J.-P.R. Wells. The large ring laser G for continuous earth rotation monitoring. *Journal of Geophysical Research*, 2008. in press.

[45] K.U. Schreiber, J-P.R. Wells, and G.E. Stedman. Noise processes in large ring lasers. *General Relativity and Gravitation*, 40:935–943, 2008.

[46] A.E. Siegman. *Lasers*. University Science Books, 1986.

[47] K.D. Skeldon, J. Mackintosh, M.V. Gradowski, S. Thieux, and R. Lee. Qualification of supermirrors for ring laser gyro based on surface roughness and scatter measurements. *Journal of Optics A*, 3:183–187, 2001.

[48] P.W. Smith. Mode locking of lasers. *IEEE Journal of Quantum Electronics*, 58:1342–1357, 1970.

[49] P.W. Smith. The effect of cross relaxiation on the behaviour of gas laser oscillators. *IEEE Journal of Quantum Electronics*, 8:704–710, 1972.

[50] P.W. Smith. Mode selection in lasers. *IEEE Journal of Quantum Electronics*, 60:422–440, 1972.

[51] G.E. Stedman. Ring-laser tests of fundamental physics and geophysics. *Reports on Progress in Physics*, 60:615–689, 1997.

[52] G.E. Stedman, Z. Li, and H.R. Bilger. Sideband analysis and seismic detection in a large ring laser. *Applied Optics*, 34:5375–5385, 1995.

[53] G.E. Stedman, Z. Li, C.H. Rowe, and A.D. McGregor. Harmonic analysis in a large ring laser with backscatter-induced pulling. *Physical Review A*, 51:4944–4957, 1995.

[54] D.B. Sullivan, D.W. Allan, D.A. Howe, and F.L. Walls. Characterization of clocks and oscillatiors. Technical report, National Institute of Standards and Technology, 1990.

[55] P.V. Wells. *Polarisation Dependence on Aplanarity in the Near Planar Ring Laser*. PhD thesis, University of Canterbury, 1996.

[56] C.P. Wyss, D.N. Wright, B.T. King, D.P. McLeod, S.J. Copper, and G.E. Stedman. Collision broadening and quantum noise in a very large ring laser gyroscope. *Optics Communications*, 174:181–189, 2000.